## General Disclaimer

## One or more of the Following Statements may affect this Document

- This document has been reproduced from the best copy furnished by the organizational source. It is being released in the interest of making available as much information as possible.

- This document may contain data, which exceeds the sheet parameters. It was furnished in this condition by the organizational source and is the best copy available.

- This document may contain tone-on-tone or color graphs, charts and/or pictures, which have been reproduced in black and white.

- This document is paginated as submitted by the original source.

- Portions of this document are not fully legible due to the historical nature of some of the material. However, it is the best reproduction available from the original submission.

SQT

NASA CR-134635



# TWO DIMENSIONAL THERMAL AND CHARGE MAPPING OF POWER THYRISTORS

Shih Pei Hu and Benjamin M. Rabinovici



NORTHEASTERN UNIVERSITY

prepared for

NATIONAL AERONAUTICS AND SPACE ADMINISTRATION

NASA LEWIS RESEARCH CENTER

Contract NAS12-2053

NASA CR-134635

# TWO DIMENSIONAL THERMAL AND CHARGE MAPPING OF POWER THYRISTORS

Shih Pei Hu and Benjamin M. Rabinovici

NORTHEASTERN UNIVERSITY

prepared for

NATIONAL AERONAUTICS AND SPACE ADMINISTRATION

NASA LEWIS RESEARCH CENTER

Contract NAS12-2053

| 1. Report No. CR 134635 | 2. Government Accession No. | 3. Recipient's Catalog No. |
|---|---|---|
| 4. Title and Subtitle<br>TWO DIMENSIONAL ANALYSIS AND MEASUREMENT OF CURRENT DENSITY AND TEMPERATURE DISTRIBUTION OF POWER THYRISTORS. | | 5. Report Date<br>6. Performing Organization Code |
| 7. Author(s)<br>SHIH PEI HU AND BENJAMIN M. RABINOVICI | | 8. Performing Organization Report No.<br>None |
| 9. Performing Organization Name and Address<br>NORTHEASTERN UNIVERSITY<br>BOSTON, MASSACHUSETTS 02115 | | 10. Work Unit No.<br>11. Contract or Grant No.<br>NAS 12-2053 |
| 12. Sponsoring Agency Name and Address<br>NATIONAL AERONAUTICS AND SPACE ADMINISTRATION<br>WASHINGTON, DC 20546 | | 13. Type of Report and Period Covered<br>CONTRACTOR REPORT<br>14. Sponsoring Agency Code |

15. Supplementary Notes
PROJECT MANAGERS - JULIAN F. BEEN AND IRA T. MYERS
SPACECRAFT TECHNOLOGY DIVISION
NASA LEWIS RESEARCH CENTER
CLEVELAND, OHIO 44135

16. Abstract

The two dimensional static and dynamic current density distributions within the junction of semiconductor power switching devices and in particular the thyristor were obtained. A method for mapping the thermal profile of the device junctions with fine resolution using an infra-red beam and measuring the attenuation through the device as a function of temperature were developed. The results obtained are useful in the design and quality control of high power semiconductor switching devices.

| 17. Key Words (Suggested by Author(s)) | 18. Distribution Statement |
|---|---|
| THYRISTORS, TWO DIMENSIONAL, SEMICONDUCTOR SWITCHES, INFRA-RED ATTENUATION, HIGH POWER, TIME DEPENDENT | UNCLASSIFIED, UNLIMITED |

| 19. Security Classif. (of this report) | 20. Security Classif. (of this page) | 21. No. of Pages | 22. Price* |
|---|---|---|---|
| UNCLASSIFIED | UNCLASSIFIED | 143 | |

* For sale by the National Technical Information Service, Springfield, Virginia 22151

NASA-C-168 (Rev. 6-71)

## SUMMARY

To understand fully the operation mechanism of a power semiconductor device and in particular thyristor, it is important to know the minority carrier, electric field, potential and current density distributions within the device as a function of the spatial variables. This report presents the formulation and closed form solution of the two-dimensional dependency of the minority carrier distribution within a thyristor for both the time independent and time dependent cases. Boundary conditions used to obtain the solution were chosen so as to conform to realistic devices being manufactured and to the physical properties of their surfaces. The general solutions were derived starting from the basic diffusion equations, and family of curves of the solutions for the static and dynamic cases of typical thyristors were obtained with the aid of a digital computer. These solutions were verified experimentally by the thermal mapping technique which was developed in the course of this work. This technique utilizes a 1.5μ infrared beam to map the temperature in the device after the device is turned on for a certain length of time (static case) or switched on and off for a large number of times (dynamic case). The differential temperature in each point of the junction is measured by the attenuation of the infrared beam through the device whose temperature dependence was experimentally well determined. Calculations were obtained by applying the analytical solutions to typical device geometries and making use of a CDC/3300 computer. The results and operating condition were plotted and compared to the results obtained with the experimental mapping method. The agreement between the analytical and experimental results were satisfactory.

# CHAPTER I

## INTRODUCTION

A p-n-p-n device was invented by W. Shockley[1] in the early 50's. The detaided device principles and the first working p-n-p-n devices were reported by J.L. Moll et al[2] in 1956. Later these works developed into two categories: a) the p-n-p-n diode[3], or Shockley diode, is a classical switch which can change between a high-impedance "off" state and a low-impedance "on" state; b) the three-terminal p-n-p-n device[3], or semiconductor-controlled rectifier (SCR), which has a gate terminal to control the switching. These devices are now developed to latch and control power systems because of their stable and low power dissipation in "on" and "off" states. They are also used as dc choppers, inverters, frequency converters, etc.[4].

An extensive presentation of the basic theories and applications of this device is available[3]. The switching criterion was established and modified by others.[3,4,5,6,7] J.J. Ebers[5] established an approximate switching theory via a two-transistor model. From Figure 1 we find:

$$I_{B1} = (1 - \alpha_1)\, I_A - I_{CO1} \tag{1}$$

$$I_{C2} = \alpha_2 \cdot I_K + I_{CO2} \tag{2}$$

$$I_{B1} = I_{C2} \tag{3}$$

$$I_k = I_A + I_G \tag{4}$$

we obtain:

$$I_A = \frac{\alpha_2 I_G + I_{CO1} + I_{CO2}}{1 - \alpha_1 - \alpha_2} \tag{5}$$

The gate current $I_G$ can trigger the switching, since when $I_G$ is increased, $I_A$ increases, and the I vs. V characteristic is changed (Figure 2).[8] When $I_G$ flows into the $P_2$ region, it will cause a non-uniform current density distribution which may over-heat the device and cause abnormal operation. This problem has been studied,[9,10,11,12] and many innovations of this device have been suggested.[10,13,14] An understanding of how the non-uniform current density is formed and changed during a series of switchings requires an understanding of the two-dimensional switching mechanism.[15] It is the objective of this work to analyse the switching mechanism in two-dimensions and to illustrate numerically the process for typical operations.

Experimentally, the lateral spreading of active-area (or turned-on area) was first tried by N. Mapham.[9] W.H. Dodson et al,[16] and H.J. Ruhl[17] measured the spreading by measuring the currents of the probing islands (Figure 3).

Multijunction semiconductor devices have rapidly become the main switching element for high efficiency compact power processing systems. Among these the thyristor is the most widely used because of its desirable means of control and latching characteristics and its superior ability to handle inductive loads. These devices must operate with the lowest possible dissipation in order to achieve high overall power processing efficiency under severe temperature conditions. Power switching devices and especially the thyristor are limited in their performance characteristics by the temperatures reached at the junctions. Nearly all significant operational parameters of a thyristor are affected in a major way by the temperature and thermal resistance of the junction. Also the life expectancy of the semiconductor power device is increased as the operating thermal stress is

reduced. When the device is switched on the current density distribution within the junction varies greatly from point to point causing uneven temperature distributions. This could lead to local over-heating and become a source of hot spots and failure. It is thus essential that the thermal profile of the junction area of any power switching semiconductor device be known. It is not sufficient to measure the average junction temperature in order to rate the device, but it is required that the temperature at any point of the junction be measured. Such a novel method was developed on this project and is fully described in the Experimental Verification section of this report. In the work described in this report an optical system was set up to test the temperature of a semiconductor device by measuring the infrared transmission which is temperature dependent.[18,19] The technique will be extended to focus and scan an infrared beam on the device and thus derive the thermal profile within the device. The transmission variations of the beam through the device produce thermal profiles which reveal the spreading of the active-area.

In the following sections, the static analysis is discussed, where the two dimensional time-independent minority carrier concentration will be solved for device configurations that have practical boundary conditions. The dynamic analysis is treated, where the time-dependent minority carrier concentration during the process of switching was derived for some type of device with very practical boundary conditions. Numerical examples calculated by digital computer are also given. The experimental work performed on this program is presented in some detail, including the description of the

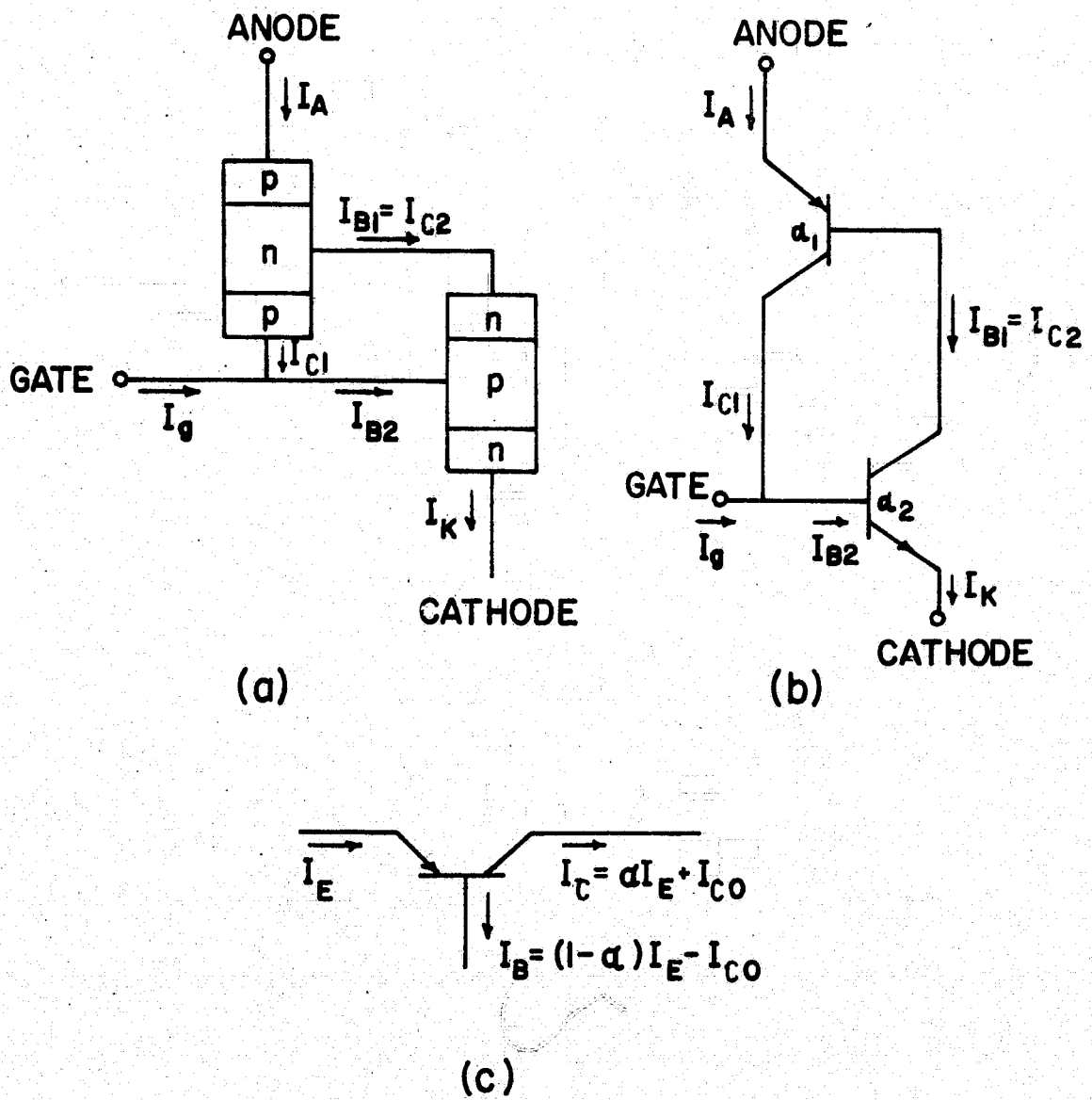


Figure 1

(a) Two transistor approximation of a three terminal p-n-p-n device
(b) Same as (a) using transistor notations
(c) Current relationships in a p-n-p transistor

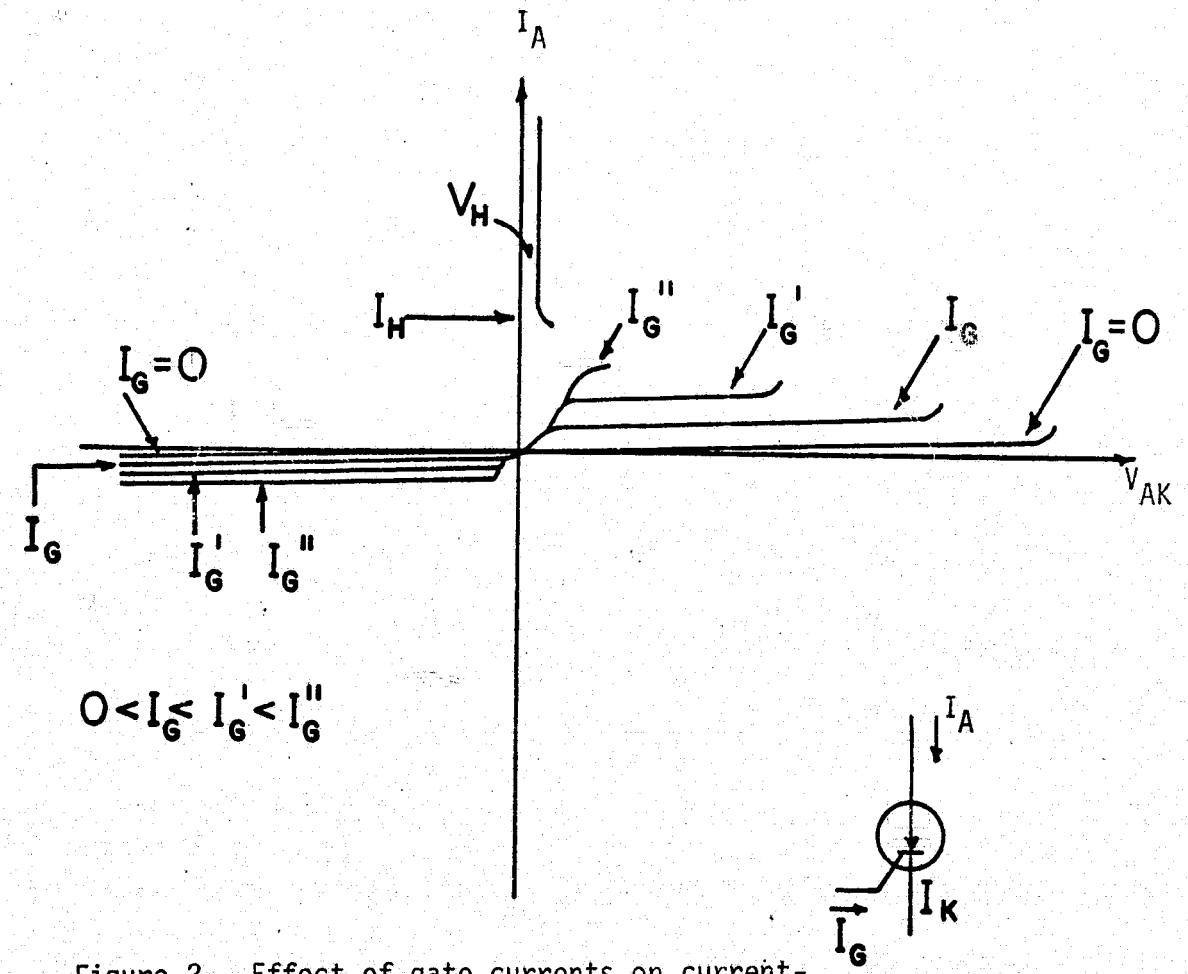


Figure 2. Effect of gate currents on current-voltage characteristics of an SCR.

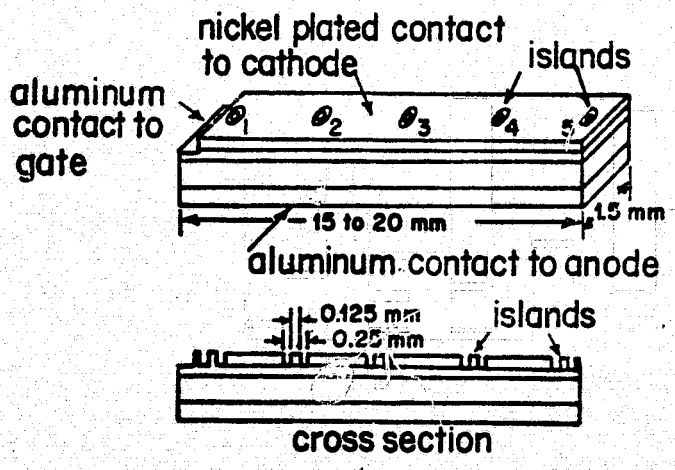


Figure 3. Device configuration. The islands permitted the observation of the on - state."

laboratory set up, the techniques used in making experimental measurements and in the analysis of the results. Also presented is a discussion of the results, their correllation, the conclusions and some recommendations for future work.

# CHAPTER II

## STATIC ANALYSIS

In three-terminal semiconductor devices like transistors, thyristors etc., electric field, potential and current density are not simply functions of one spatial variable, since between emitter and collector, the third terminal always contributes lateral current disturbance. Therefore, it is necessary to use a two-dimensional analysis in order to investigate their operating mechanism in detail. For thyristors (Figure 4 and 5) the two-dimensional nature of the current flow is even more accentuated, since when the device is first "turned-on" by the application of a gate current, the load current density will start off slowly with a non-uniform distribution which will result in a partial turn-on of the device and could produce so called "hot-spots". This problem was particularly noticed in the case of high-speed, high-power thyristors.[20,21] Two-dimensional approaches were used with limited success to derive the h-parameters for bipolar transistors.[22,24]

However, in order to determine the two-dimensional distribution of current, potential and electric field of a typical three-terminal semiconductor device, one must have a detailed knowledge about minority carrier distribution within the specified device and how this relates to its geometry. In this section an approach is employed that takes this into consideration[15] and treats the general steady state two-dimensional solution for the minority carrier distributions of semiconductor multijunction devices and the thyristor in particular. The novelty of this approach is that the analysis is applied to practical device geometries that are typically in use.

Figures

Figure 4. A typical thyristor geometry. Areas shaded are ohmic contacts, the nonshaded surfaces are covered by oxide. Typical doping concentrations are:

$p_1 = 10^{19}$ cm$^{-3}$, $n_1 = 10^{14}$ cm$^{-3}$,

$p_2 = 10^{16}$ cm$^{-3}$, $n_2 = 10^{19}$ cm$^{-3}$

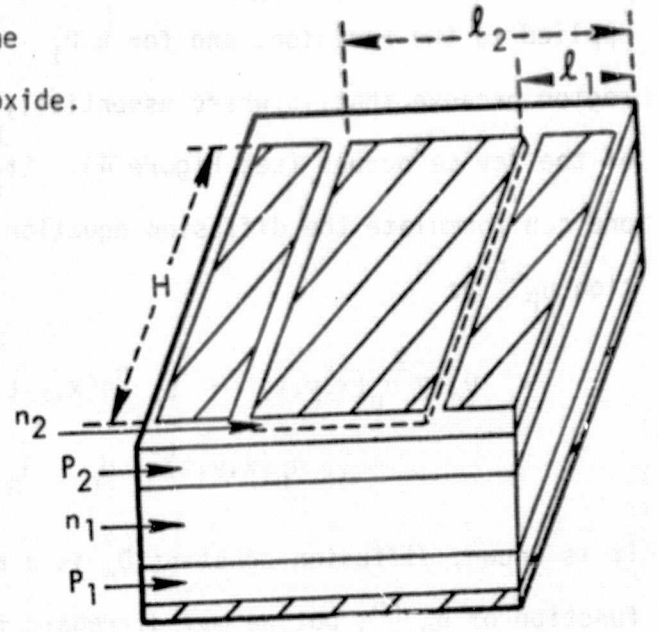


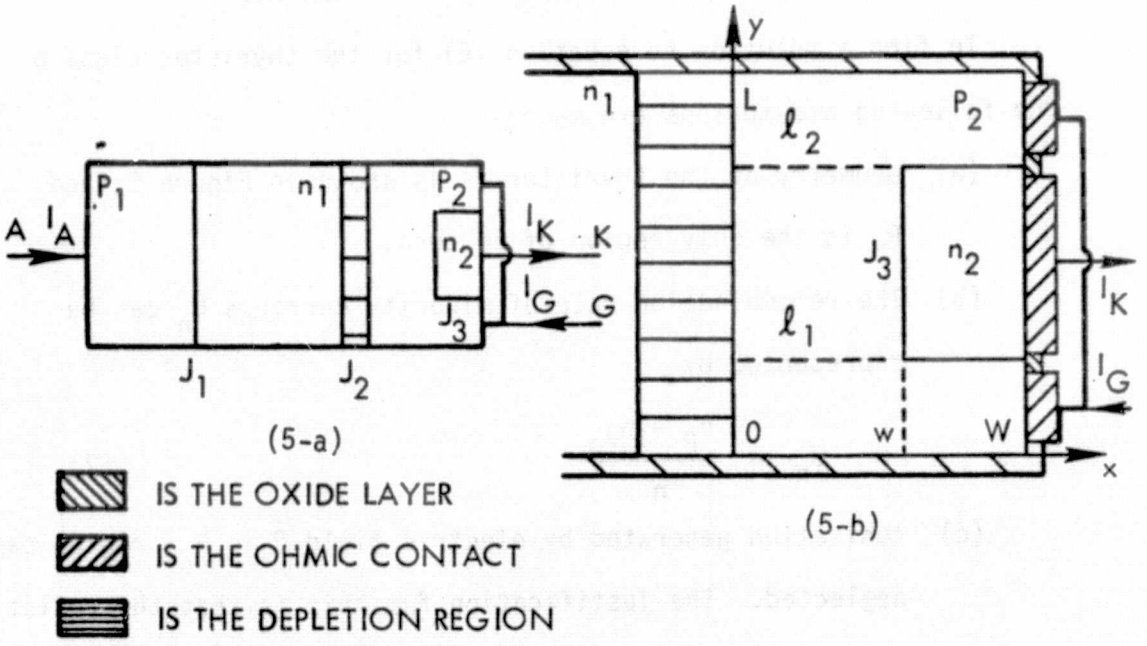


Figure (5-a) A thyristor in forward blocking bias.

Figure (5-b) Close up of $p_2$ - $n_2$ regions

Note, $L - \ell_2 = \ell_1$. A, anode; k, cathode; G, gate

Formulation of the Problem

For an $n_1 - P_2 - n_2$ transistor, a two-dimensional analysis should be applied to the P-region, and for a $P_1 - n_1 - P_2 - n_2$ thyristor, to the $P_2$ region because that is where essentially the non-uniform power dissipation of the device occurs (see Figure 4). Starting with the continuity equation one can formulate the diffusion equation for the minority carrier concentration $n_p$[25] as

$$D_n \vec{\nabla}^2 n_p(x,y,t) + \mu_n n_p(x,y,t) \vec{\nabla} \cdot \vec{E} + \mu_n \vec{E} \cdot [\vec{\nabla} n_p(x,y,t)] = \frac{\partial}{\partial t} n_p(x,y,t) + U_n - G_n \qquad (6)$$

It is known, diffusion constant $D_n$ is a non-linear, monotonically increasing function of $n_p$ [26], but we may disregard this non-linearity if $n_p$ is less than the number of states in the conduction band Nc.

To find a solution to equation (6) for the thyristor class of devices the following assumptions are made:

(a) Geometry of the thyristor is as shown in Figure 5, and $P_2$ is the only region of concern.

(b) The recombination rate of minority carriers $U_n$ can be represented by

$$U_n = \frac{n_p - n_{po}}{\tau_n} \qquad (7)$$

(c) Ionization generated by electric field $\vec{E}$ in $P_2$- region can be neglected. The justification for this is that the resistivity of $P_2$ is about 1.2 ohm - cm, for a current density of 1 amp/cm$^2$

the field $\vec{E}$ ($\lesssim \rho \vec{J}$) is only 1.2 volt/cm. and the ionization generation rate of electrons is $3.8\times10^{6}\ \exp(-1.75\times10^{6}/|E|\ )\ |J|/q^{27}$, or around the order of $10^{-10^{6}}$ $sec^{-1}\text{-}cm^{-3}$ which is very, very small. On the other hand, for $n_p \approx 10^{15}$ $cm^{-3}$ (which $\vec{J}$ is 1 $Amp/cm^2$) and $\tau_n = 10^{-6}$ sec, the recombination rate $U_n$ is around the order of $10^{21}$ $sec^{-1}\text{-}cm^{-3}$, which makes the ionization generation rate in equation (6) negligible.

(d) No other carrier generations (e.g. surface generation) exist, thus $G_n = 0$.

(e) The oxide on the surface is considered as a perfect insulator. Namely, no current may flow through the oxide.

(f) This analysis is limited to the low level injection case. Therefore, by charge neutrality, the Poisson's equation is now

$$\vec{\nabla} \cdot \vec{E} = \frac{\rho\ (x,y,t)}{\varepsilon} = 0. \qquad (8)$$

and therefore the $\vec{\nabla} \cdot \vec{E}$ term in equation (6) may be ignored.

(g) The electric field $\vec{E}$ in the $P_2$-region is so small that the third term on the left of equation (6) can be ignored. The justification for high-power devices like thyristors, is that the field $\vec{E}$ is mainly in the x-direction (longitudinal). Considering the assumptions so far, equation (6) in x-direction can be rewritten for the static case:

$$D_n \frac{\partial^2 n_p}{\partial x^2} + \mu_n E \frac{\partial n_p}{\partial x} = \frac{n_p - n_{p_o}}{\tau_n} \qquad (9)$$

The solution is

$$n_p(x) = n_{P_o} + C_1 e^{m_1 x} + C_2 e^{m_2 x}$$

where $$m_{1,2} = -\left[\frac{\mu_n E}{2D_n} \pm \sqrt{\left(\frac{\mu_n E^2}{2D_n}\right) + \frac{1}{D_n \tau_n}}\right] \qquad (10)$$

Thus the importance of E can be justified by comparing with

$$E_o = \sqrt{\frac{4\ D_n}{\mu_n^2 \tau_n}} \qquad (11)$$

For typical values of $\mu_n = 10^3$ cm$^2$/V-sec, $D_n = 25$ cm$^2$/ sec, $\tau_n = 10^{-6}$ sec, $E_o = 10$ V/cm while the field due to ohmic drop, as mentioned in assumption (c), is 1.2 V/cm. The field due to doping profile in the $P_2$-region is approximately $(D_p/\mu_p N_A)(\partial N_A/\partial X)$, and is about 5 V/cm for a typical acceptor gradient of $2 \times 10^{18}$ cm$^{-4}$. Therefore, as a first order solution, we may ignore the field completely in equation (6). As a result of the above assumptions, equation (6) can now be simplified for the steady state case as:

$$D_n \vec{\nabla}^2 n_p(x,y,t) = \frac{n_p(x,y,t) - n_{Po}}{\tau_n} \qquad (12)$$

Equation (12) will be solved for the steady state condition for two distinct cases. The first is the steady state case with gate left open. This corresponds to a forward blocking thyristor and forward conducting thyristor when triggered by gate pulse (current density in $P_2$-region must meet assumption (g) ). This condition would also apply to a transistor

with no base current. The second is the steady state case when the gate is in operation. This corresponds to the gate controlled thyristor (or typical transistor with base current). The transient case where the gate has just been applied will be treated separately in the following chapter.

Substituting

$$n_s(x,y) = n_p(x,y,o) \tag{13}$$

and defining

$$N_s(x,y) = n_s(x,y) - n_{p_o} \tag{14}$$

equation (12) may be rewritten as

$$L_n^2 \vec{\nabla}^2 N_s(x,y) = N_s(x,y) \tag{15}$$

where, of course

$$L_n^2 = D_n \tau_n \tag{16}$$

Boundary Condition and Solution

Since for the forward blocking thyristor, the depletion region sweeps out all the electrons on the boundary we have $n_p = o$ at $x = o$. (This is condition (A) listed below). Ohmic contracts force the boundary to maintain the carriers in equilibrium $n_{po}$ (condition (B) ). By assumption (e), current flow through the oxide boundary (i.e., the concentration gradient normal to the boundary) is zero (condition (C) and (D) ). Conservation of current should hold on the gates (condition (E) ) and junction $J_3$ (condition (F) ). When $(\ell_2 - \ell_1) \to \infty$, we may have (see Figure (5-b) ),

$$n_s(W,\frac{L}{2}) = n_{pw} = n_{po}\, e^{qV_{J3}/kT} \qquad (17)$$

because in this case, $P_2 - n_2$ can be considered as a forward biased diode without "gates" (condition (G) ).

With reference to Figure (5-b) and equations (13) and (14) one may list the boundary conditions as follows:

$$(A)\quad N_s(o,y) = n_{po} \qquad 0 < y < L \qquad (18)$$

$$(B)\quad N_s(\overline{W},y) = 0 \qquad 0 < y < \ell_1 \ell_2 < y < L \qquad (19)$$

$$(C)\quad \left.\frac{\partial N_s}{\partial y}\right|_{y=0} = 0 \qquad 0 < x < \overline{W} \qquad (20)$$

$$(D)\quad \left.\frac{\partial N_s}{\partial y}\right|_{y=L} = 0 \qquad 0 < x < \overline{W} \qquad (21)$$

$$(E)\quad I_{nG} = -\,2qD_n H \int_0^{\ell_1} \left.\frac{\partial N_s}{\partial x}\right|_{x=\overline{W}} dy \qquad (22)$$

$$(F)\quad I_{nP}(J_3) = qD_n H \left[ \int_{\ell_1}^{\ell_2} \left.\frac{\partial N_s}{\partial x}\right|_{x=W} dy + \int_{W}^{\overline{W}} \left.\frac{\partial N_s}{\partial y}\right|_{y=\ell_1} dx + \int_{W}^{\overline{W}} \left( - \left.\frac{\partial N_s}{\partial y}\right|_{y=\ell_2} \right) dx \right] \tag{23}$$

$$(G)\quad N_s\left(W, \frac{L}{2}\right) = n_{Pw} - n_{Po} \qquad (\ell_2 - \ell_1) \to \infty \tag{24}$$

NOTE:
$$I_{nP}(J_3) \approx \frac{qD_n H}{L_n} n_{Po} \left(e^{qV_{J3}/kT} - 1\right) (2\overline{W} - 2w + \ell_2 - \ell_1) \tag{25}$$

For forward conducting thyristor, junction $J_2$ is also forward biased (Figure 6). The minority carriers in proximity to the depletion region are no longer completely swept across $J_2$. In this case condition A, should be changed to:

$$(\acute{A})\quad N_s(0,y) = n_{Pf} - n_{Po} \qquad 0<y<L \tag{26}$$

where

$$n_{Pf} = a\, n_{Po}\, e^{qV_{J2}/kT} \tag{27}$$

Equation (17) should also be modified as

$$n_{Pw} = c\, n_{Po}\, e^{qV_{J3}/bkT} \tag{28}$$

a,b,c, are the interaction factors which account for the fact that each junction is affected by the other two[28]. Now, applying the separation of

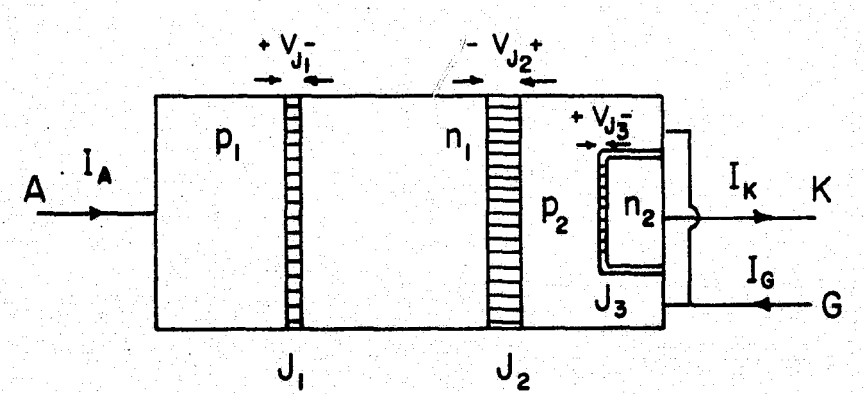


Figure 6. A thyristor in forward conducting state; dashed regions are depleted junctions.

variables method,[29] one sets

$$N_s(x,y) = X(x)Y(y) \tag{29}$$

and equation (15) is then written as

$$L_n^2 \left[ X\frac{\partial^2 Y}{\partial y^2} + Y\frac{\partial^2 X}{\partial x^2} \right] = XY \tag{30}$$

conditions (C) and (D) imply

$$Y(y) = \cos \frac{k\pi y}{L} \qquad k = 0, 1, 2, \text{------} \tag{31}$$

By substituting equation (31) into equation (30), one obtains

$$L_n^2 \left[ -X\left(\frac{\pi^2 k^2}{L^2} Y\right) + Y\frac{\partial^2 X}{\partial x^2} \right] = XY \tag{32}$$

The particular solution for X is then of the form

$$X(x) = \sinh \sqrt{\frac{1}{L_n^2} + \frac{K^2\pi^2}{L^2}}\, X \tag{33}$$

We may satisfy conditions (A), (B), and (E) by superposing a few terms in the form of equation (33) for X(x), so that $N_s(x,y)$ is $-n_{po}$ for x = 0, zero for x = W, and finite slope for x = W. A possible combination of terms giving a complete solution to equation (16) is as follows:

$$N_s(x,y) = \sum_{k=0}^{\infty} \cos \frac{k\pi y}{L} \left[ A_k \sinh \sqrt{\frac{1}{L_n^2} + \frac{k^2\pi^2}{L^2}}\, x \right.$$

$$+ B_k \sinh \sqrt{\frac{1}{L_n^2} + \frac{k^2\pi^2}{L^2}}\, (x - w) - C_k U_{-1}(x - w) \sinh \sqrt{\frac{1}{L_n^2} + \frac{k^2\pi^2}{L^2}}$$

$$\left. (x - w) \right] \qquad (34)$$

where $U_{-1}(x-w)$ is a step function at x=w. $A_k$, $B_k$, $C_k$ are unspecified coefficients for the conditons mentioned above.

As listed above, there are seven boundary conditions for this analysis, but only two (conditions (C) and (D) ) have been satisfied by the "$\cos \frac{k\pi y}{L}$" part of equation (34). In this equation, there are only three sets of unknown coefficients, not enough to satisfy the other five conditions. One may superpose five terms in the form of equation (33) to satisfy these conditions, but then a complete solution with five infinite series will be too tedious to calculate numerically for any set of (x,y). One may, however, simulate equation (34) to a certain function at a given x-plane, so that one brings in sufficient unknownsto satisfy these conditions. One may assume a function for $\frac{\partial N_s}{\partial x}$ at x = w plane (see Figure 7) as follows:

$$\left.\frac{\partial N_s}{\partial x}\right|_{x=w} = Q \equiv \begin{cases} n_o' + (n_w' - n_o') \sin \dfrac{4}{\pi} \dfrac{y}{2\ell} & 0 < y < \ell \\ n_w' & \ell < y < L - \ell \\ n_o' + (n_w' - n_o') \sin \dfrac{4}{\pi} \dfrac{(L-y)}{2\ell} & L - \ell < y < L \end{cases}$$

(35)

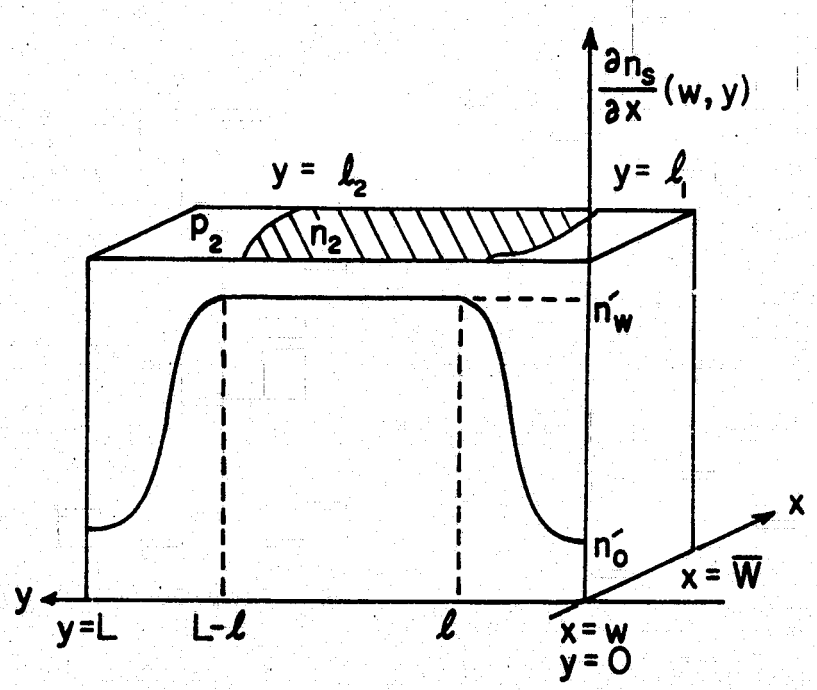


Figure 7. Qualitative characteristics of function Q given in equation (35).

$n_w'$, $n_o'$, $\ell$ are the new unknowns, in addition to $A_k$, $B_k$, $C_k$, now one has the exact number of unknowns for conditions (A), (B), (E), (F), (C), and equation (35).

The reason for assuming a function Q for $\frac{\partial N_s}{\partial x}\Big|_{x=w}$, instead of $N_s(w,y)$ is that it would bring faster convergence for the coefficients, and therefore reduce the number of terms to be retained in the infinite series. This is important to the numerical calculations to be performed. The choice of "$\sin^4\theta$" for function Q was aimed towards a simpler mathematical derivation for the coefficients as well as faster convergence for the infinite series. With the help of a digital computer, one may find how close "$\sin^4\theta$" is to an optimal choice.

The determination of coefficients $A_k$, $B_k$, $C_k$ and unknowns $n_w'$, $n_o'$, $\ell$ should be related to the particular cases of interest.

Case A $\quad I_{Gn} = 0.$

(A) Forward blocking thyristor.

By condition (A) and equation (34).

$$B_k = \begin{cases} \dfrac{n_{Po}}{\sinh(\frac{W}{L_n})} & \text{for } k = 0 \\ 0 & \text{for } k \neq 0 \end{cases} \qquad (36)$$

By equation (35),

$$A_k = \begin{cases} \left\{ \left[ n_w' \left( L - \frac{5}{4}\ell \right) + \frac{5}{4} n_o' \ell \right] \frac{L_n}{L} - B_o \right\} \Big/ \cosh \frac{W}{L_n} & \text{for } k = 0 \\ & \text{for } k = \text{odd} \\ \dfrac{4 (n_w' - n_o') \sin \frac{k\pi\ell}{L}}{n\pi \sqrt{\alpha} \cosh \sqrt{\alpha} W} \left\{ -1 + \dfrac{k\ell}{L(2 + \frac{k\ell}{L})} \left[ 1 + \dfrac{2}{1 + \frac{k\ell}{L}} \left( 1 + \right. \right. \right. & \\ \left. \left. \left. \dfrac{3}{\frac{2\,k\ell}{L}} \left[ 1 + \dfrac{1}{\frac{2\,k\ell}{L} - 4} + \dfrac{1}{\frac{2\,k\ell}{L} - 2} \right] \right) \right] \right\} & \text{for } k \text{ even} \end{cases} \tag{37}$$

where $\sqrt{\alpha} \sqrt{\dfrac{1}{L_n^2} + \dfrac{k^2\pi^2}{L^2}}$

From condition (E),

$$C_k = C_k + A_k \frac{\cosh \sqrt{\alpha}\, \overline{W}}{\cosh \sqrt{\alpha}\, (\overline{W} - w)} \tag{38}$$

The details of these calculations are presented in Appendix A.

By condition (F) ),

$$I_{np}(J_3) = qD_n H \left\{ \frac{L-2\ell}{L_n} (A_o \cosh \frac{w}{Ln} + B_o) - 2 \sum_{\substack{k \text{ even} \\ k \neq 0}}^{\infty} A_k \sin \frac{k\pi\ell}{L} \left\{ \frac{L\sqrt{\alpha}}{k\pi} \text{Cosh } \sqrt{\alpha}\, w + \frac{k\pi}{L\sqrt{\alpha}} \sinh (\sqrt{\alpha}\, w) \tanh \sqrt{\alpha} (\overline{W} - w) \right] \right\} \tag{39}$$

Note, since

$$I_{pn}(J_3) \simeq \frac{qDp}{L_p} p_{no} \left(e^{qV_{J3}/kT} - 1\right) H(2\bar{W} - 2w + \ell_2 - \ell) \tag{40}$$

and

$$I_k = I_{pn}(J_3) + I_{np}(J_3) \tag{41}$$

When, $n_{po} >> p_{no}$, then $I_{np}(J_3) >> I_{pn}(J_3)$, and $I_{np}(J_3) \simeq I_K$.

By condition (G) and equation (34),

$$n_{pw} - n_{po} \equiv N_s\left(w, \frac{L}{2}\right) = A_o \sinh \frac{W}{L_n} + \sum_{\substack{k \neq o \\ k \text{ even}}}^{\infty} (-1)^{k/2} A_k \sinh \sqrt{\alpha}\, w \tag{42}$$

It follows from condition (B) that the minority carriers at the gate - metal contacts (assumed to be ohmic) are at equilibrium. However, for a practical device the following two factors must be noted:

(a) The $P_2$ - base is usually highly doped, ($P_2 = 10^{16}$ cm$^{-3}$, typically), and the metal contacts can hardly be considered to be "ohmic" (true only for a $P^+$ - metal contact).

(b) The metal contact in this case is opened, and electrons can accumulate and build up a potential which tends to stop the sweep of electrons to the metal through the depletion region

of $P_2$ - metal junction. This means that $n_s(\overline{W},y)$ may become larger than equilibrium number $n_{po}$[†], or $N_s(\overline{W},y) \geq n_{po}$ for $0 < y < \ell_1$ , $\ell_2 < y < L$, where

$$N_s(\overline{W},0) = A_o \sinh \frac{\overline{W}}{L_n} \Big/ \cosh \frac{\overline{W} - w}{L_n} + \sum_{\substack{k \neq o \\ k \text{ even}}}^{\infty} A_k \sinh \sqrt{\alpha} w \Big/ \cosh \sqrt{\alpha}(\overline{W} - w) \qquad (43)$$

By equations (36 - 39, 42, 43), we may solve for the unknowns

$n_w'$, $n_o'$, $\ell$ , $A_k$, $B_k$ and $C_k$.

(B) Forward conducting thyristor

Equations (37) to (43), obtained in part (A) remain valid but $n_{pw}$ as per equation (28) is replaced by $n_{pw}'$. From condition (A'), equation (36) now becomes

$$B_k = \begin{cases} \dfrac{n_{po} - n_{pf}}{\sinh \dfrac{W}{L_n}} & \text{for } k = 0 \\ 0 & \text{for } k \neq 0 \end{cases} \qquad (44)$$

---

[†]The force that sweeps electrons from semiconductor to metal by the field in depletion region can be balanced by the repulsion between the electrons in the metal and semiconductor.
For $P_2$ of $10^{16}$ $cm^{-3}$, the maximum number of electrons on the metal (which is left open) is $2 \times 10^6$ $cm^{-3}$, then no electron can go farther than one third of the depletion length. c.f. The book by S.M. Sze (reference 25) Chapter 8 discusses the metal-semiconductor junction.

Case B $\quad I_{Gn} \neq 0$

For a forward blocking thyristor, this represents the condition between gate triggering and turn on, or the condition the device is in after it has switched over. Equations (36) and (37) for $B_k$ and $A_k$ in case A are still valid. By virtue of condition (B),

$$C_k = B_k + A_k \frac{\sinh \sqrt{\alpha}\, \overline{W}}{\sinh \sqrt{\alpha}\, (\overline{W} - w)} \tag{45}$$

From condition (E) and equation (45)

$$\frac{I_{Gn}}{q D_n} = 2 \frac{H \ell_1 A_o \sinh \frac{w}{L_n}}{L_n \sinh \frac{\overline{W} - w}{L_n}} + 2H \sum_{\substack{k \neq o \\ k \text{ even}}}^{\infty} \frac{\sqrt{\alpha}\, L \sin \frac{k\pi \ell_1}{L} A_k \sinh \sqrt{\alpha}\, w}{k\pi \sinh \sqrt{\alpha}\, (\overline{W} - w)} \tag{46}$$

and from condition (F) and equation (45)

$$I_{np}(J_3) = H q D_n \left\{ \frac{L - 2\ell_1}{L_n} (A_o \cosh \frac{w}{L_n} + B_o) + 2 \sum_{\substack{k \neq o \\ k \text{ even}}}^{\infty} A_k \sin \frac{k\pi \ell_1}{L} \left[ - \frac{L\sqrt{\alpha}}{k\pi} \cosh \sqrt{\alpha}\, w + \frac{k\pi \sinh \sqrt{\alpha}\, w}{L\sqrt{\alpha} \sinh \sqrt{\alpha}\, (\overline{W} - w)} (1 - \cosh \sqrt{\alpha}\, (W - w)) \right] \right\} \tag{47}$$

The above equations are derived in Appendix B. By equation (36), (37), (42), (45), (46), and (47), one may solve for the unknowns $n_w'$, $n_o'$, $\ell$, $A_k$, $B_k$, and $C_k$.

Numerical Calculations

Since the concentration of minority carriers in the forward blocking case could change from zero to $10^{12}$ within $10^{-3}$ cm, the numerical calculations may face a serious problem of accuracy. It was therefore necessary to take particular care in the course of writing the computer program to minimize the possibility of errors. The calculations were carried out on CDC-3300 Computer at Northeastern University Computation Center. The program was written in FORTRAN IV in double precision and the calculations were found to have an accuracy of at least twelve digits. The following examples are the numerical calculations corresponding to each case discussed above.

Example 1 For a typical thyristor, in forward blocking state the geometry was as follows:

$$H = 5 \times 10^{-2} \text{ cm}, \quad L = 5.1 \times 10^{-2} \text{ cm}, \quad w = 5 \times 10^{-3} \text{ cm},$$

$$\overline{W} = 1 \times 10^{-2} \text{ cm}, \quad \ell_1 = 3.5 \times 10^{-3} \text{ cm}.$$

The other parameters are, $L_n = 5 \times 10^{-3}$ cm, $D_n = 25$ cm$^2$/sec, and $\tau_n = 10^{-6}$ sec. Doping with $P_2 = 10^{16}$ cm$^{-3}$, $n_2 = 10^{19}$ cm$^{-3}$ and $n_{po} = 2.2 \times 10^{4}$ cm$^{-3}$. When $I_k = 4.4 \times 10^{-7}$ amp, $I_G = 0$, in forward blocking state one may solve equations (39), (42), and (43) simultaneously and obtain

$$\ell = 1.5118 \times 10^{-2} \text{ cm}.$$

$$n_w^2 = 6.5836652 \times 10^{13} \text{ cm}^{-4}$$

$$n_o^2 = 2.6683225 \times 10^{12} \text{ cm}^{-4}$$

Substituting these values in equations (36), (37), and (38) one obtains the coefficients $A_k$, $B_k$, $C_k$, explicitly. Thus from equations (14) and (34), one could plot the minority carrier distribution $n_s(x,y)$ as shown in Figure 8. The derivative with respect to x, $\frac{\partial n_s(x,y)}{\partial x}$ which is $\frac{J_{nx}(x,y)}{q_n D_n}$, is shown in Figure 9. From Figure 8, one can note that minority carriers distribute smoothly in $P_2$-region. Figure 9 shows how smooth the distribution of $J_{nx}$ is. However, one observes that in the region of $w<x<\bar{W}$ and $0<y<\ell_1$, $J_{nx}$ of $y = 0$ is larger than $J_{nx}$ of $y = \ell_1$. This is because $\vec{J}_n$ is mostly in the y-direction when electrons flow out of $n_2$ into $P_2$ region.

From this solution, $n_s(x,y)$, one calculates $\vec{J}_n$ as

$$\vec{J}_n = q\, D_n \left[\hat{x}\, \frac{\partial}{\partial x} + \hat{y}\, \frac{\partial}{\partial y}\right] n_s(x,y) \qquad (48)$$

One may estimate the electric field in x-direction as

$$\vec{E}_x = \vec{I}_{px} / \left[q\mu_p\, P_2\, x(\text{cross section area})\right] \qquad (49)$$

where

$$\vec{I}_{Px} = \vec{I} - \vec{I}_{nx} \qquad (50)$$

and

$$\vec{I}_{nx} = H \int_0^L \vec{J}_{nx}\, dy \qquad (51)$$

Example 2 Same thyristor, but in forward conducting state without gate current. $I_k = 0.125$ amp. $I_G = 0$, $V_2 = 0.95$ volt (polarity as defined in Figure 6), $V_3 = 1.13$ volts, $a = 0.82$, $b = 1.5$, $c = 0.877$. By equations (39), (42), and (43), the parameters are calculated to be:

Figure 8

The three-dimensional minority carrier distribution in $p_2$-region, $n_p(x,y)$, in forward blocking open gate case. To read the curves exactly, find the x- and y- axes first, then read on the vertical axes on each division of x-axis for the variables plotted. (Read the variables from y=o to $y=\frac{L}{2}$ ). The curves in y=L/2 to y=L are symertric to the curves shown here.

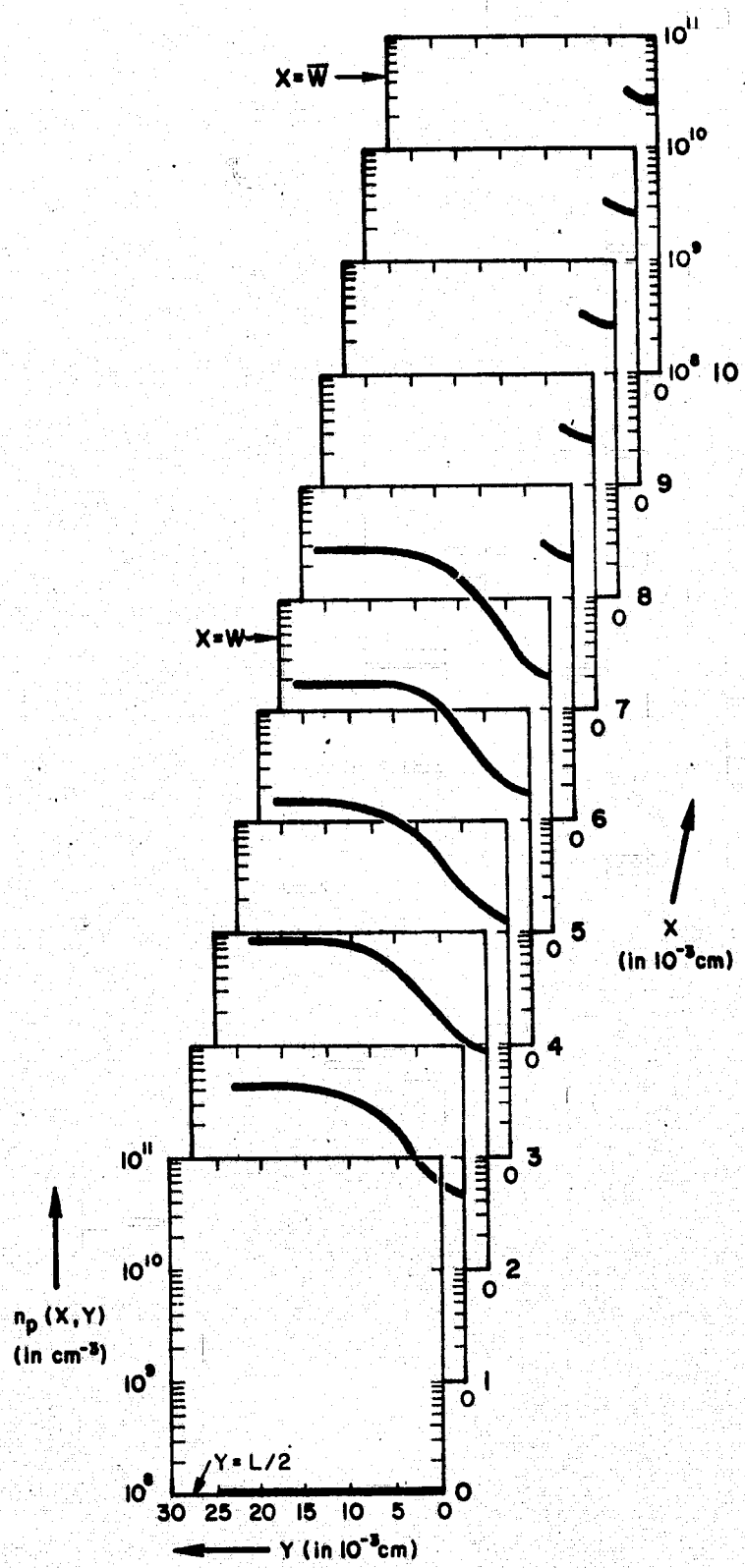

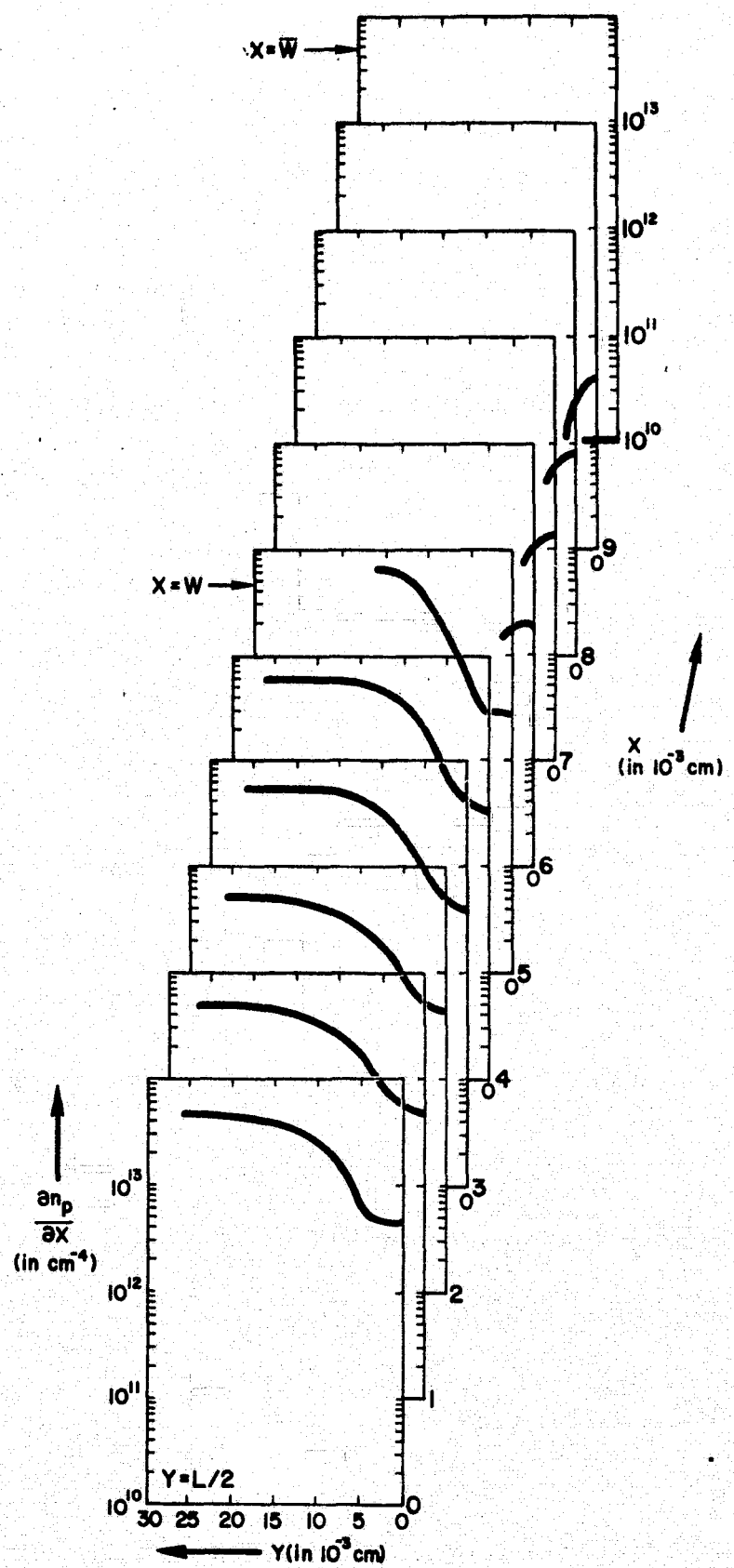


Figure 9
$\partial n_p(x,y)/\partial x$, the slope in x-direction of $n_p(x,y)$ in $p_2$-region in forward blocking open gate.

$$\ell = 4.97 \times 10^{-3} \text{cm}$$

$$n_w' = 1.35215768 \times 10^{19} \text{ cm}^{-4}$$

$$n_o' = 2.01741901 \times 10^{17} \text{ cm}^{-4}$$

Again with these values, one obtains the coefficients An, Bn, Cn explicitly. The plot of $n_s(x,y)$ is shown in Figure 10. The distribution varies smoothly, $\frac{\partial n_s(x,y)}{\partial x}$ and $\frac{\partial n_s(x,y)}{\partial y}$ are plotted in Figure 11. From equation (48), one may find the distribution of $J_n$ in $P_2$-region. In the region of $0<y<\ell_1$, $w<x<\bar{w}$, $\vec{J}_n$ is flowing toward the gate when close to $n_2$-region, but turned around and flows toward junction $J_2$ when close to the oxide (i.e., $y = 0$). This is due to the high current density at the $P_2$ - $n_2$ junction, especially at $\ell_1<y<\ell_2$, for this forward conducting case.

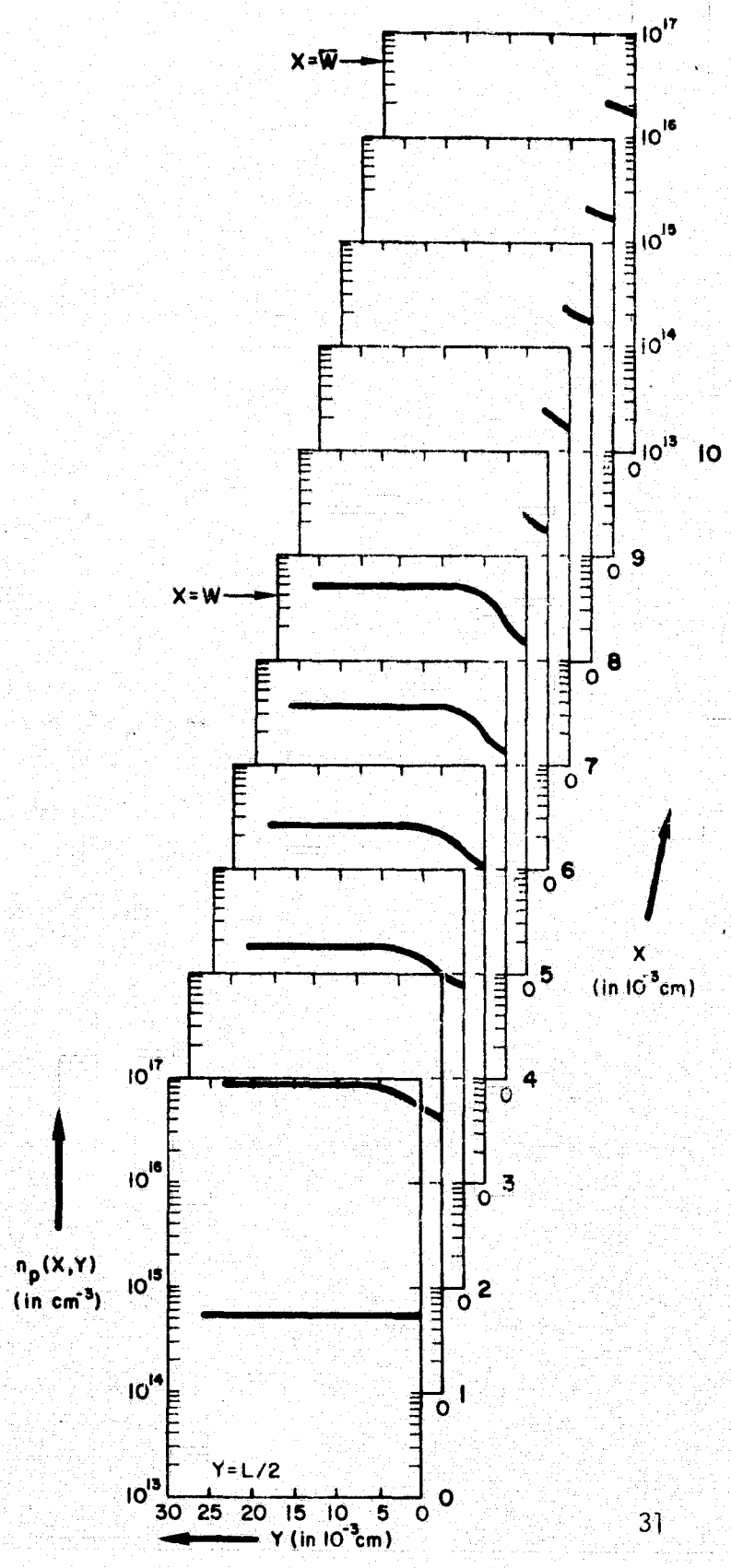


Figure 10

The minority carrier distribution in $p_2$-region $n_p(x,y)$ in forward conduction open gate case.

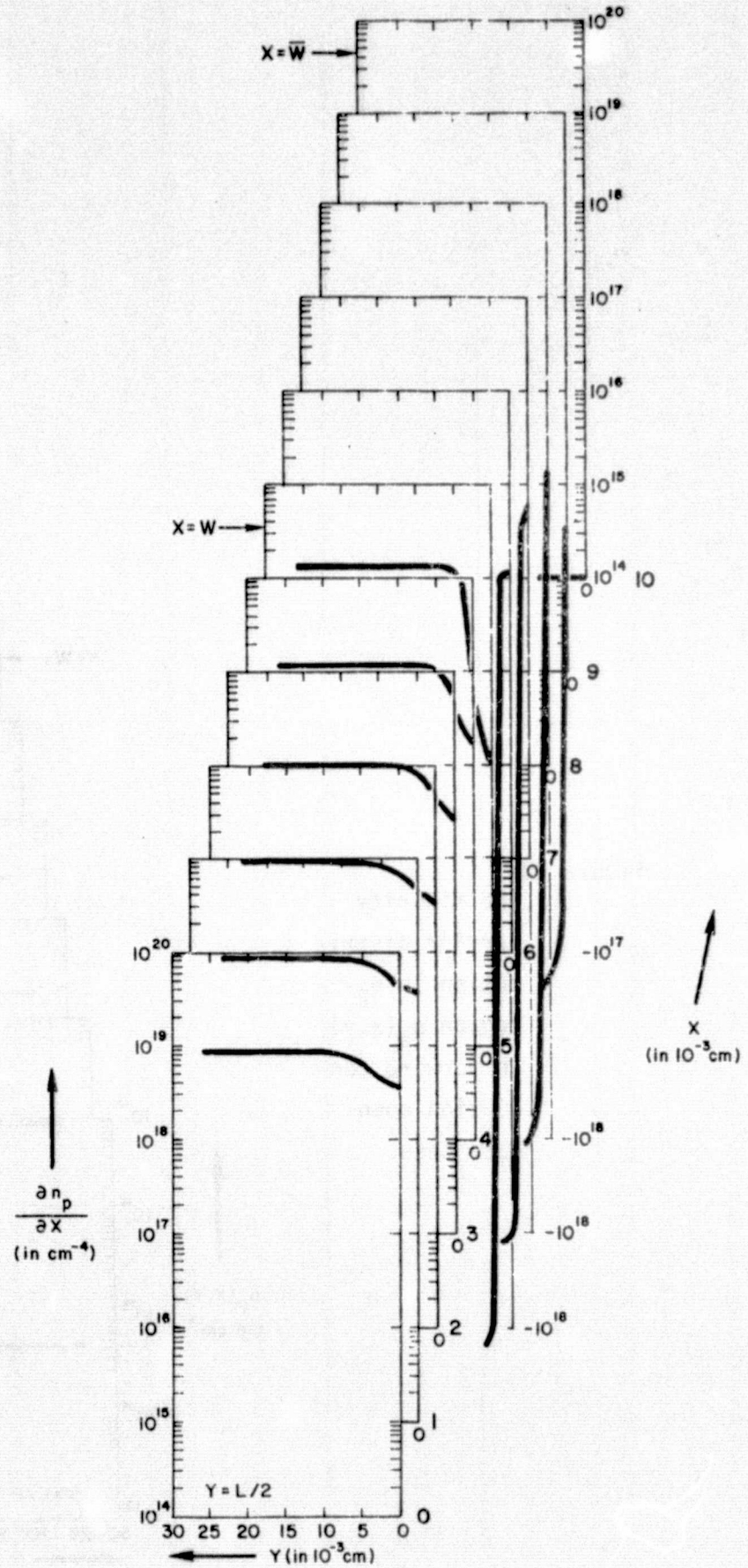


Figure 11a

In forward conducting open gate case, $\partial n_p(x,y)/\partial x$, the slope of $n_p(x,y)$ in x-direction in $p_2$-region (a). $\partial n_p(x,y)/\partial y$, the slope of $n_p(x,y)$ in y-direction (b). These two figures give the x and y components of $J_n/qD_n$.

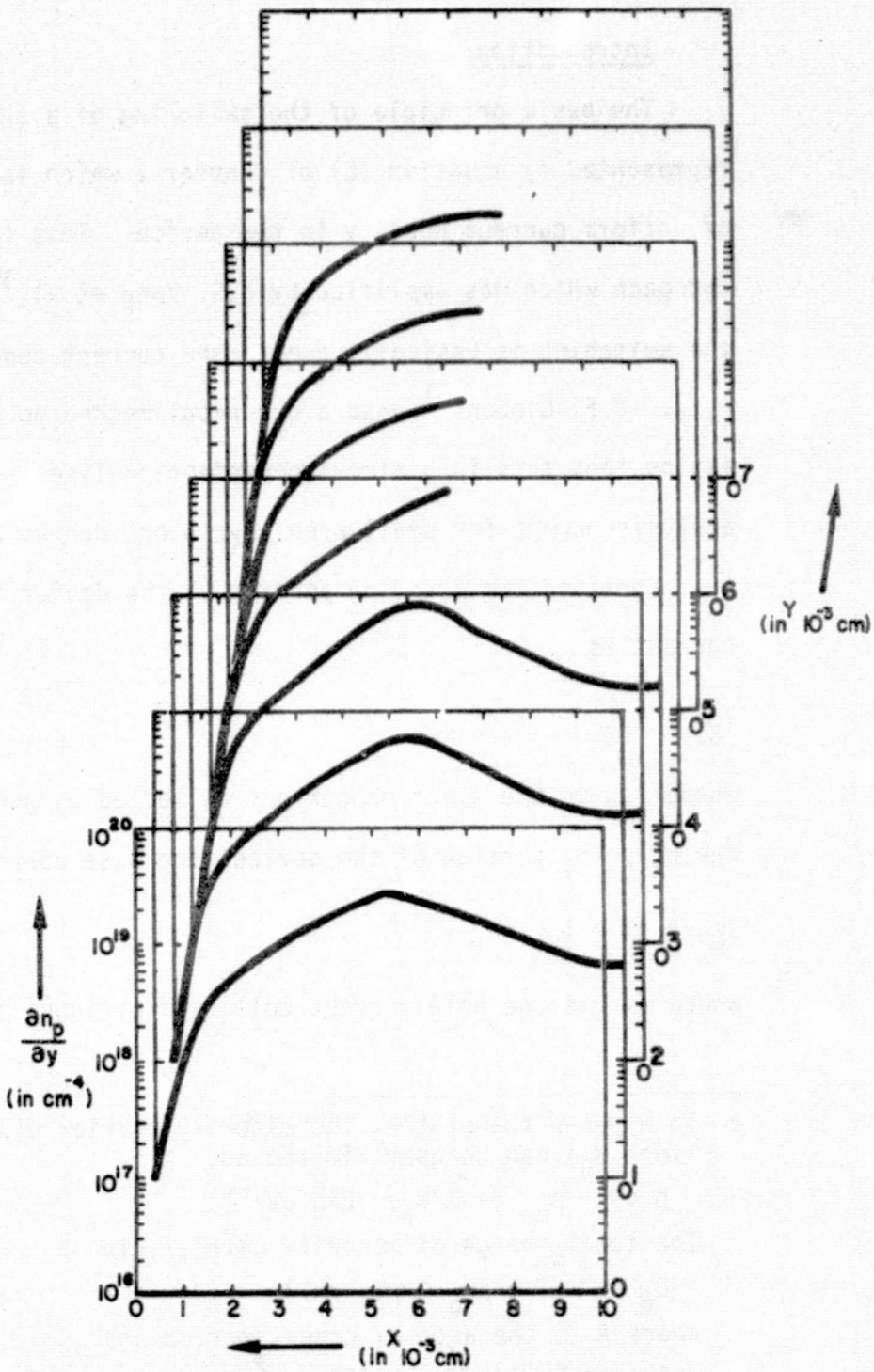
$10^{20}$
$10^{19}$
$10^{18}$
$10^{17}$
$10^{16}$
$\frac{\partial n_p}{\partial y}$
(in $cm^{-4}$)
0 1 2 3 4 5 6 7 8 9 10
X
(in $10^{-3}$ cm)
0 1 2 3 4 5 6 7
Y
(in $10^{-3}$ cm)

Figure 11b

# CHAPTER III

# DYNAMIC ANALYSIS

## Introduction

The basic principle of the switching of a thyristor can be well represented by equation (5) of Chapter I which is based on the assumption of uniform current density in the device. This is a one dimensional approach which was amplified by E.S. Yang et al,[30] and who pointed out that the switching is basically due to the current dependence of current gains $_1$, $_2$. J.F. Gibbons[31] used a graphical method to analyse the I-V characteristics, but this is a time-independent analyses. The one-dimensional analysis valid for small area thyristors can be briefly states as follows:

Consider the $p_1$-$n_1$-$p_2$ portion of the device in Figure 12, the base current is

$$I_{B1} = I_{C2} \tag{52}$$

where $I_{C2}$ is the electron current collected by junction $J_2$. Consider the $n_2$-$p_2$-$n_1$ portion of the device, the base current is

$$I_{B2} = I_G + I_{C1} \tag{53}$$

where $I_{C1}$ is the hole current collected by junction $J_2$. But,†

---

† In a p-n-p transistor, the minority carrier distribution in base (of width $W_B$) can be approximated as,

$$p(x) = p_{no}\ (1-X/W_B)\ \ Exp(qV/kT)$$

The total charge of minority carriers is

$$Q_B = \frac{A\ W_B}{2}\ q\ p_{no}\ Exp(qV/kT)$$

where A is the area of cross section and

$$I = -AqD_p\ (dp/dx) = (2D_p/W_B^2)Q_B$$

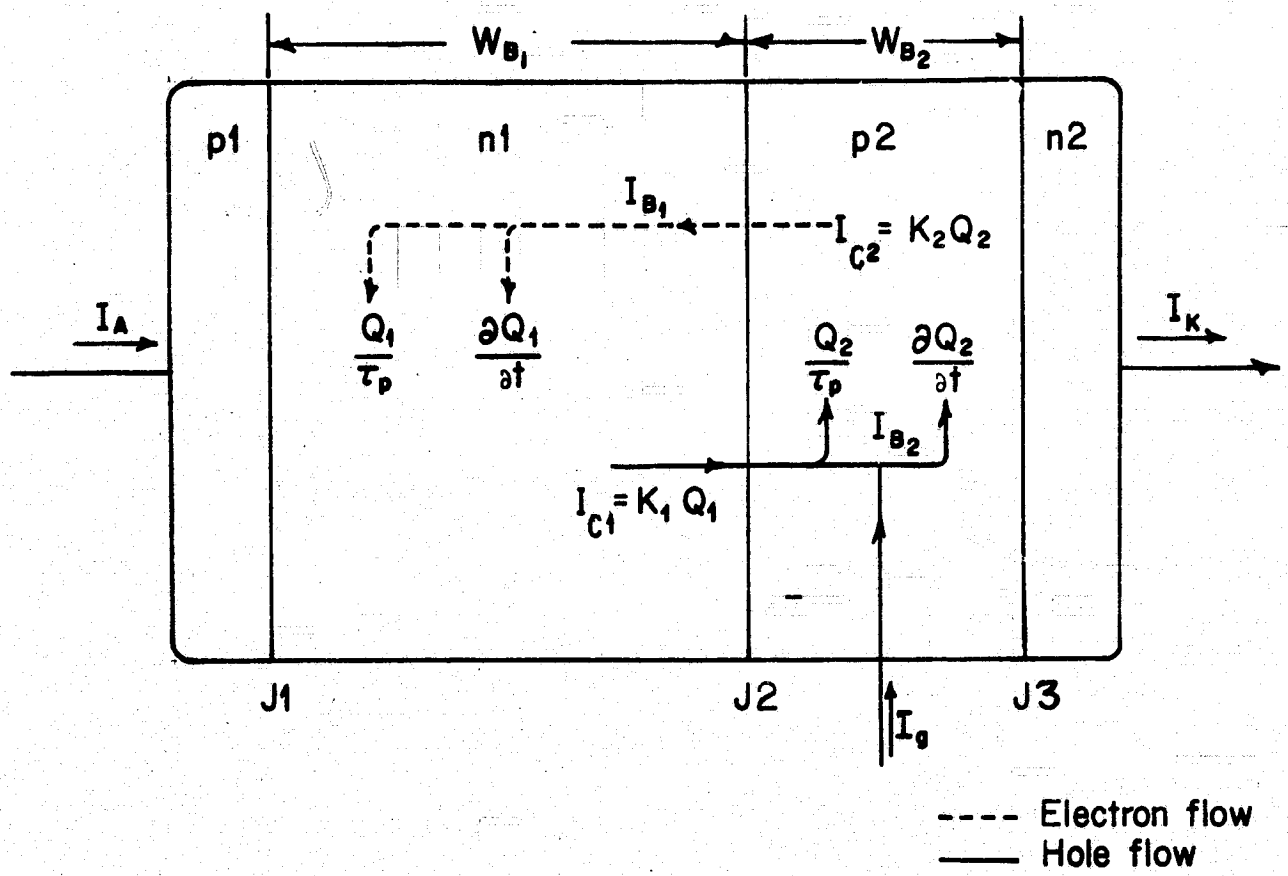


Figure 12. Model for turn-on analysis.

$$I_{C1} = K_1 Q_1 \tag{54}$$

$$I_{C2} = K_2 Q_2 \tag{55}$$

From the equation of continuity,

$$-\vec{\nabla}.\vec{J}_p = q\frac{\partial p}{\partial t} + q\,\frac{p-po}{\tau_p} \tag{56}$$

$$\text{vol. of } n_I \int (-\vec{\nabla}.\ \vec{J}_p)\ dv = \frac{\partial Q_1}{\partial t} + \frac{Q1}{\tau_p} \tag{57}$$

So,

$$I_{B1} = \frac{\partial Q_1}{\partial t} + \frac{Q_1}{\tau_p} \tag{58}$$

likewise,

$$I_{B2} = \frac{\partial Q_2}{\partial t} + \frac{Q_2}{\tau_n} \tag{59}$$

Substituting equations (54) and (59) into equation (53), one obtains

$$I_G + K_1 Q_1 = \frac{\partial Q_2}{\partial t} + \frac{Q_2}{\tau_n} \tag{60}$$

Substituting equations (55) and (58) into equation (52), one obtains

$$K_2 Q_2 = \frac{Q_1}{\tau_p} + \frac{\partial Q_1}{\partial t} \tag{61}$$

Use Laplace transform to solve $Q_1$, $Q_2$ simultaneously in s-domain, then take inverse Laplace transform back to time domain,

$$Q_1(t) = K_2 I_G \left[\frac{1}{ab} + \frac{\mathrm{Exp}(-at)}{a(a-b)} + \frac{\mathrm{Exp}(-bt)}{b(b-a)}\right] \quad (62)$$

and

$$Q_2(t) = \frac{I_G}{\tau_p}\left[\frac{1}{ab} + \frac{(1-a\tau_p)}{a(a-b)}\,\mathrm{Exp}(-at) + \frac{(1-b\tau_p)}{b(b-a)}\,\mathrm{Exp}(-bt)\right] \quad (63)$$

where

$$a,\ b = \frac{\tau_p + \tau_n}{2\tau_p\tau_n}\left[1 \pm \sqrt{1 + \frac{4K_1K_2\tau_p^2\tau_n^2 - 4\tau_p\tau_n}{(\tau_p + \tau_n)^2}}\right] \quad (64)$$

Since

$$I_A(t) = K_1 Q_1(t) + K_2 Q_2(t) \quad (65)$$

one may find the $I_A$ response as a function of $I_G$.

This approach was used by G.D. Bergman[12] to calculate rise time and delay time of switching and by R.L. Davies,[32] et al.

Instead of integrating the equation of continuity to establish the relationship between current (I) and charge (Q) as shown in equation (65), it is more rigorous to solve the minority carrier distribution from the diffusion equation, then calculate the electric quantities like current density $\vec{J}$, field $\vec{E}$ and potential V. This approach assumes no lateral uniformity and applies equally well for the one- and two-dimensional analysis. This approach was used by A.A. Lebedev, A.I. Uvarov, and V.E. Chelnokov (one dimensional).[33,34,35,36] They solved the minority

carrier distributions in $n_1$ and $p_2$ regions when "turned-on" by assuming no electric field, low level injection and that the number of minority carrier is negligible in "off" state. They imposed the boundary conditions of the continuity of current at each junction and they obtained general solutions of minority carriers in the form of Laplace transform. They did not obtain the inverse Laplace transform and therefore did not obtain a general time dependent closed form solution and their time-dependent solutions were presented only for some very particular cases.[33]

In the novel approach used in this work one solves the diffusion equation in $n_1$ and $p_2$ regions separately for each region making use of the basic techniques like separation of variables, Fourier series and Laplace transform. These are general time-dependent two dimensional solutions applicable to practical thyristor device geometries. These solutions are then calculated numerically and plotted. With the computer programs given in Appendix C,D,E and F one may calculate the characteristics of other given thyristor types having different geometries and different doping characteristics.

## Formulation of the Problem

As discussed in earlier chapter, the distribution of the minority carrier concentrations is a fundamental and descriptive approach to obtain electric quantities like $\vec{J}$, $\vec{E}$, V. This is true for both static and dynamic cases. For a typical thyristor one would start from the continuity equation and formulate the diffusion equations for the minority carrier $p_n$ in $n_1$ region

$$D_p \vec{\nabla}'^2 p_n + \mu_p p_n \vec{\nabla}' \cdot \vec{E}_1 - \mu_p \vec{E}_1 \cdot (\vec{\nabla}' p_n) = \frac{p_n - p_{no}}{\tau_p} + \frac{\partial p_n}{\partial t} \qquad (66)$$

where

$$\vec{\nabla}' = -\hat{x} \frac{\partial}{\partial x} + \hat{y} \frac{\partial}{\partial y}$$

and for the minority carrier $n_p$ in $p_2$-region

$$D_n \vec{\nabla}^2 n_p + \mu_n n_p \vec{\nabla} \cdot \vec{E}_2 + \mu_n \vec{E}_2 \cdot (\vec{\nabla} n_p) = \frac{n_p - n_{po}}{\tau_n} + \frac{\partial n_p}{\partial t} \qquad (67)$$

where $\vec{\nabla} = \hat{x} \frac{\partial}{\partial x} + y \frac{\partial}{\partial y}$

$$\vec{E} = \hat{x} E_x + \hat{y} E_y$$

To find the solution to equations (66) and (67), one makes the following assumptions:

(a) Geometry of the thyristor is as shown in Figure 13, Notice, the device is symmetrical along the $y = L/2$ line.

(b) The recombination rate of minority carriers $U_p$ and $U_n$ are

$$U_p = p_n/\tau_p$$

$$U_n = n_p/\tau_n$$

The equilibrium minority carrier concentrations of $P_{no}$ and $n_{po}$ are negligible compared to $P_n$ and $n_p$ respectively for the dynamic case.

(c) Ionization generated by electric field $\vec{E}$ can be neglected. The justification is given under the section on Formulation of the Problem.

(d) No other carrier generations exist, thus

$G_p = 0$, $G_n = 0$

(e) The oxide on the surface is considered as a perfect insulator.

(f) This analysis is limited to the low level injection case. Therefore, the Poisson's equation is,

$\vec{\nabla} \cdot \vec{E} = \rho(x,y,t)/\varepsilon = 0$, by charge neutrality.

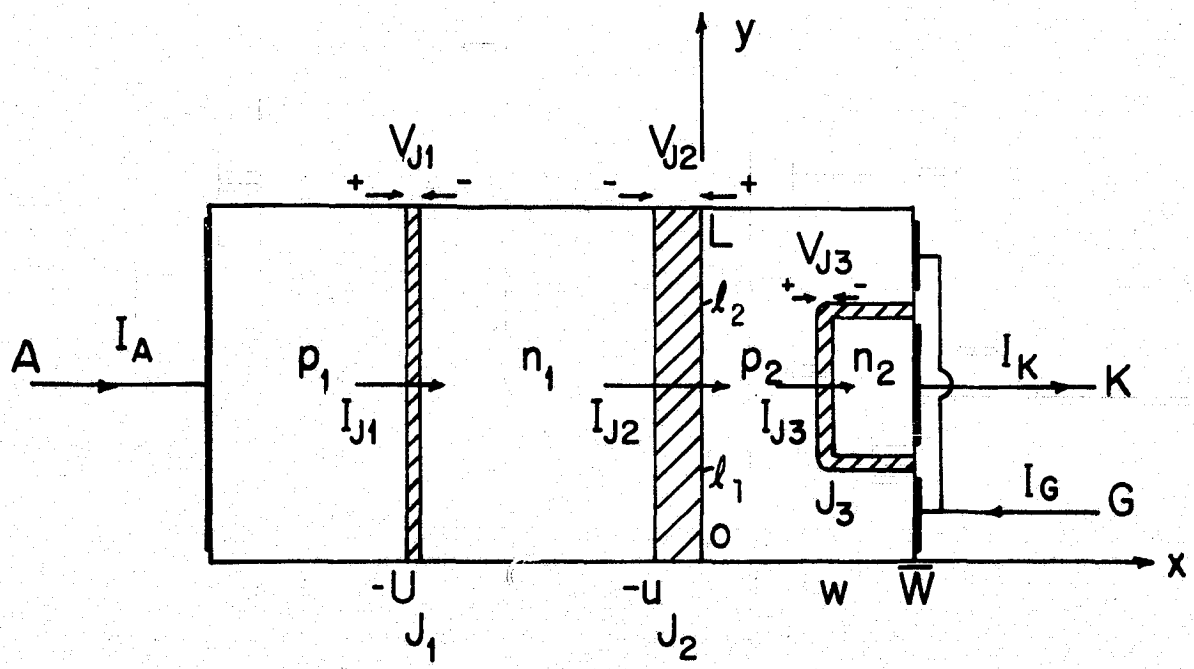


Figure 13 A Two-dimensional View of a Typical Thyristor. Slashed-line regions are depletion regions, potential polarities are defined as shown.

(g) Electric field $\vec{E}$ is not negligible in $n_1$-region, but is negligible in the $P_2$-region. The justification for this assumption is also given in the section on Formulation of the Problem. In the $n_1$-region, one may compare the electric field (due to doping profile and current conduction) to the critical field to justify this assumption. As given by equation (11), the critical field is:

$$E_o = \sqrt{\frac{4\ D_p}{\mu_p^2 \tau_p}}$$

For typical values of $\mu_p$ = 350 $cm^2$/V-sec, $D_p$ = 13 $cm^2$/sec, and $\tau_p = 10^{-6}$ sec, the critical field is $E_o$ = 20.6 V/cm. The field due to doping profile in the $n_1$-region is $(D_n/\mu_n N_D)\ (\partial N_D/\partial x)$, and is estimated to be 2 V/cm and is negligible compared to the critical field. When the device is conducting a current of 1 Amp/$cm^2$ (which is lower than typical forward conducting current) in the $n_1$-region of typical resistivity 40 Ω-cm, the field is 40 V/cm,much larger than the critical electric field. Therefore, the electric field in $n_1$-region becomes more and more important as the device is turned-on.

(h) The problem is two-dimensional in $P_2$-region, while in $n_1$-region it is one-dimensional. The distinction is based on

the geometry and whether there are more than two current sources or not.

The boundary conditions can be stated as follows:

$$(A)\quad n_p(x,y,t)\Big|_{\substack{x=o\\t=o}} = p_n(x,y,t)\Big|_{\substack{x=-\mu\\t=o}} = 0$$

$$(B)\quad \frac{\partial n_p}{\partial y}\Big|_{\substack{y=o\\y=L/2\\y=L}} = \frac{\partial p_n}{\partial y}\Big|_{\substack{y=o\\y=L/2\\y=L}} = 0$$

$$(C)\quad n_p(x,y,t)\Big|_{x=\overline{W}} = n_{po} \qquad \ell_2<y<L,\quad 0<y<\ell_1,$$

$$(D)\quad I_{J1} = I_{J2}$$

$$(E)\quad I_{J2} + I_G = I_{J3}$$

Condition (A) refers to the fact that the number of minority carriers is zero at the depletion boundary, condition (B) refers to the insulation of oxide and symmetry of the device, conditon (C) refers to the ohmic contact at the gate contacts, conditions (D) and (E) refer to the conservation of current. Each current can be symbolically represented as

$$I_{J1} = LHq\left[\mu_p\ E_{1x}\ p_n(x=-U) - D_p\ \frac{\partial p_n}{\partial x}\Big|_{x=-U}\right] + I_{R1}\ e^{\,qV_1/\eta kT} \tag{68}$$

$$I_{J2} = LHM(V_2)q \left[ -D_p \frac{\partial p_n}{\partial x} \Big|_{x=u} + \mu_p\, p_n(x=-u)\, E_{1x} \right]$$

$$+ M(V_2)qH \int_o^L \left( D_n \frac{\partial n_p}{\partial x} \Big|_{x=o} + \mu_n\, n_p(x=o)\, E_{2x} \right) dy \qquad (69)$$

$$I_{J3} = qH \left[ \int_{\ell 1}^{\ell 2} \left( D_n \frac{\partial n_p}{\partial x} \Big|_{x=w} + \mu_n\, n_p(x=w)\, E_{2x} \right) dy \right.$$

$$\left. + 2 \int_w^{\overline{w}} \left( D_n \frac{\partial n_p}{\partial y} \Big|_{y=\ell_1} + \mu_n\, n_p(y=\ell_1)\, E_{2y} \right) dx \right]$$

$$+ I_{R3}\, e^{qV_3/\eta kT} \qquad (70)$$

$\vec{E}_1$, $\vec{E}_2$ are electric fields in $n_1$ or $P_2$ regions respectively, and,

$$\vec{E}_1 = \rho n_1\, \vec{I}_{J1} / HL \qquad (71)$$

and

$$M(V_2) = \left[ 1 - \left( \frac{V_2}{V_{BD2}} \right)^3 \right]^{-1} \qquad (72)$$

the multiplication factor,

$$u = \sqrt{2\, K_s\, \varepsilon_o\, V_{J2}/qN_A} \qquad (73)$$

the depletion length of $J_2$,

$$I_{R1}\, e^{qV_1/\eta kT} = \frac{n_i HL}{\tau} \sqrt{K_s\, \varepsilon_o q\, V_1/2N_D}\, e^{qV_1/2kT} \qquad (74)$$

the recombination current of $J_1$, and

$$I_{R3}\, e^{qV_3/\eta kT} = \frac{n_i HL}{\tau}\sqrt{k_s \varepsilon_o q\, V_3/2N_A}\; e^{qV_3/2kT} \qquad (75)$$

the recombination current of $J_3$.

Because the factor $\eta$ ($\approx 2$) is the exponent, the recombination current of $J_3$ is negligible in equations (68) and (70) when the depletion lengths of each junction are not much larger than the diffusion lengths. $V_{BD2}$ for typical $n_1$ ($10^{14}$ $cm^{-3}$) is 1150 volts, while the forward blocking voltage is no more than 500 volts, so equation (72) gives $M(V_2) \approx 1$. With these considerations along with boundary (A), (B) and assumption (g), we may simplify equations (68), (69) and (70) as:

$$I_{J1} = L\, H\, q \left[ \mu_p\, E_{1x}\, p_n(x=-U) - D_p \left.\frac{\partial p_n}{\partial x}\right|_{x=-U} \right] \qquad (76)$$

$$I_{J2} = L\, H\, q \left[ -D_p \left.\frac{\partial p_n}{\partial x}\right|_{x=-u} \right] + qHD_n \int_0^L \left.\frac{\partial n_p}{\partial x}\right|_{x=0} dy \qquad (77)$$

$$I_{J3} = q\, H\, D_n \left[ \int_{\ell_1}^{\ell_2} \left.\frac{\partial n_p}{\partial x}\right|_{x=w} dy + 2 \int_w^{\overline{w}} \left.\frac{\partial n_p}{\partial y}\right|_{y=\ell_1} dx \right] \qquad (78)$$

We may obtain the minority carrier concentrations $p_n(x,y,t)$ and $n_p(x,y,t)$ by solving equations (66) and (67) subject to the boundary conditions (A) through (E) and equations (76), (77) and (78).

Solutions for the Minority Carrier Concentration

Equations (66) and (67) are two independent partial differential equations, but boundary conditions (D) and (E) joined with equations (76), (77), and (78) make $p_n(x,y,t)$ and $n_p(x,y,t)$ mutually related. A.A. Lebedev et al. tried to solve them simultaneously[7,8,9], but it was too tedious to obtain the general solutions. We may, on the other hand, solve equations (66) and (67) independently, $I_{J1}$, $I_{J2}$, and $I_{J3}$ are considered as boundary values for $n_1$- or $P_2$-region, the conservation of them (i.e. boundary conditions (D) and (E) will be the modification of these boundary values after certain interval. With the efficient digital computers available these days, the interval lengths can be chosen arbitrarily small, then the analytical and numerical solutions can be obtained with all the boundary conditions satisfied.

(A) Solutions for $n_1$-region

By considering assumptions (a) through (h), equation (66) can be rewritten as:

$$D_p \frac{\partial^2}{\partial x^2} p_n + \mu_p E_1 \frac{\partial p_n}{\partial x} = \frac{Pn}{\tau_p} + \frac{\partial pn}{\partial t} \qquad (79)$$

In order to obtain the solution of this equation in closed form, it is found that to take the Laplace transform of equation (79) is a good approach. So, take the Laplace transform of both sides:

$$\frac{\partial^2}{\partial x^2} P + a_1 \frac{\partial}{\partial x} P = s_1 P - p_n(x,o) \qquad (80)$$

where

$$p(x,s) \equiv \mathcal{L}\{p_n(x,t)\} = \int_0^s p_n(x,t)\, e^{-st}\, dt$$

$$a \equiv \mu_p E_1 / D_p$$

$$s_1 \equiv (s + 1/\tau_p)/D_p$$

$p_n(x,o)$ is the initial condition of $P(x,s)$. It is the well-known static solution in the form of

$$p_n(x,o) = -p_n U \sinh \frac{x+u}{L_p} / \sinh \frac{U-u}{L_p}$$

$$= -b_1 \sinh \frac{x+u}{L_p} \qquad (81)$$

$$p_n U \equiv p_n(x=-U)$$

$$b_1 \equiv p_n U / \sinh \frac{U-u}{L_p}$$

The complete solution of equation (80) consists of a particular solution, $p_p(x,s)$ and complementary solution $p_c(x,s)$,

$$P(x,s) = p_p(x,s) + p_c(x,s) \qquad (82)$$

By substituting equation (81) into equation (80), the particular solution of this one-variable equation is

$$p_p(x,s) = \frac{bL_p^2}{2D_p}\left[\frac{e^{(x+u)/L_p}}{1+a_1L_p-s_1L_p^2} + \frac{e^{-(x+u)/L_p}}{s_1L_p^2+a_1L_p-1}\right] \qquad (83)$$

By substituting equations (82) and (83) into equation (80), we obtain the equation to solve for $P_c(x,s)$,

$$\frac{\partial^2}{\partial x^2} P_c + a_1 \frac{\partial}{\partial x} P_c = s_1 P_c \qquad (84)$$

$P_c(x,s)$ is obtainable by assuming it to be in the form of $e^{mx}$. Solving for m (two values), $P_c(x,s)$ is obtained as

$$P_c(x,s) = \left[ A_1 e^{\sqrt{a_1^2/4+s_1}\,(x+u)} + A_2 e^{-\sqrt{a_1^2/4+s_1}\,(x+u)} \right] e^{a_1 (x+u)/2} \qquad (85)$$

Now, using the technique of inverse Laplace transform one obtains the time function $p_n(x,t)$. Using the transform

$$\mathcal{L}\{e^{ht}\} = \int_0^\infty e^{ht}\, e^{-st}\, dt = \frac{1}{s-h} \qquad \text{Re}\{s\} > h$$

or, the inverse Laplace transform,

$$\mathcal{L}^{-1}\left\{\frac{1}{s-h}\right\} = e^{ht} \qquad \text{Re}\{s\} > h$$

One has:

$$P_p(x,t) = \mathcal{L}^{-1}\{P_p(x,s)\}$$

$$= \frac{b_1}{2}\left[ e^{-(x+u+a_1 D_p t)/L_p} - e^{(x+u+a_1 D_p t)/L_p} \right] \qquad (86)$$

$$= -\, b_1 \sinh\left(\frac{x+u}{L_p} + \frac{a_1 D_p t}{L_p}\right)$$

Before obtaining the inverse Laplace transform, we would check the equation (85) first. By the "initial value theorem",

$$\lim_{s \to \infty} s\, P(x,s) = p_n(x,o) \qquad (87)$$

Considering equations (82), (83), and (85), $\lim_{s \to \infty} s\, P_p(x,s) = p_n(x,o)$ and coefficient $A_2$ of $P_c(x,s)$ has to be zero, since otherwise

$$\lim_{s \to \infty} s\, e^{-\sqrt{a_1^2/4 + s_1}\,(x+u)} = \infty$$

Note, $x \leq -u<o$ in $n_1$-region. And also

$$\lim_{s \to \infty} s\, e^{\sqrt{a_1^2/4 + s_1}\,(x+u)} = 0$$

Therefore, the value of $A_1$ is unrestricted by equation (87). As stated, boundary conditions (D), (E) are now considered as boundary values. Condition (D) may then be restated as a description of gradient of $p_n(x,t)$,

$$(D') \quad \left.\frac{\partial p_n(x,t)}{\partial x}\right|_{x=-u} = c_1$$

which means $I_{pn}(x=-u)=-HLqD_p c_1$. By a Laplace transformation,

$$(D'') \quad \left.\frac{\partial P(x,s)}{\partial x}\right|_{x=-u} = \frac{c_1}{s}$$

Condition (D") is not a rigorous condition, since in any time interval, the actual value of $c_1$ varies as switching is started. Therefore, $c_1$ can be considered as a "final value" after a certain time interval, and

$$(D'') \quad \lim_{s \to 0} s \left. \frac{\partial \beta}{\partial x} \right|_{x=u} = c_1$$

Since

$$\left. \frac{\partial p}{\partial x} \right|_{x=u} = \frac{b_1 L_p}{2 D_p} \left( \frac{1}{1+a_1 L_p - s_1 L_p^2} - \frac{1}{a_1 L_p - 1 + s_1 L_p^2} \right)$$

$$+ A_1 \left( \frac{a_2}{2} + s_1 + a_1^2/4 \right) \tag{88}$$

$$\therefore A_1 = c_1 \Big/ s\left( \frac{a_1}{2} + \sqrt{\frac{1}{L_p^2} + \frac{a_1^2}{4}} \right)$$

$$p_c(x,s) = c_1 e^{-a_1 |x+u|/2} \frac{e^{-\sqrt{\frac{s}{D_p} + \frac{1}{L_p^2} + \frac{a_1^2}{4}} |x+u|}}{s\left( \frac{a_1}{4} + \sqrt{\frac{1}{L_p^2} + \frac{a_1^2}{4}} \right)} \tag{89}$$

Note, $x+u = -|x=u|$ for $x \leq -u$

$-x+u = |x+u|$ for $x \leq -u$

By equation (58) and (59), and equation (10) of Bateman's Table[38],

$$\mathcal{L}^{-1} \left\{ \frac{2e^{-\sqrt{\alpha s}}}{s+\beta} \right\} = e^{-\beta t} \left[ e^{-j\sqrt{\alpha\beta}} \operatorname{erfc}\left( \tfrac{1}{2}\sqrt{\frac{\alpha}{t}} - j\sqrt{\beta t} \right) \right.$$

$$\left. + e^{j\sqrt{\alpha\beta}} \operatorname{erfc}\left( \tfrac{1}{2}\sqrt{\frac{\alpha}{t}} + J\sqrt{\beta t} \right) \right] \tag{90}$$

$$P_c(x,t) = \mathcal{L}^{-1}\left\{P_c(x,s)\right\}$$

$$= c_1 e^{-a_1|x+u|/2}\left[e^{\left(|x+u|\sqrt{1/L_p{}^2+a_1{}^2/4}\right)}\operatorname{erfc}\left(\frac{|x+u|}{2\sqrt{D_p t}}\right.\right.$$

$$\left.+\sqrt{\frac{t}{\tau_p}+\frac{a_1{}^2 D_p t}{4}}\right) + e^{-|x+u|\sqrt{1/L_p{}^2+a_1{}^2/4}}$$

$$\left.\times \operatorname{erfc}\left(\frac{|x+u|}{2\sqrt{D_p t}} - \sqrt{\frac{t}{\tau_p}+\frac{a_1{}^2 D_p t}{4}}\right)\right] \Bigg/ \left(a_1+\sqrt{a_1{}^2+\frac{4}{L_p{}^2}}\right) \tag{91}$$

From equations (86) and (91), the minority carrier concentration in the $n_1$-region is:

$$P_n(x,t) = P_p(x,t) + P_c(x,t) \tag{92}$$

To find the current one takes the x-derivative of $p_n(x,t)$

$$\frac{\partial p_n(x,t)}{\partial x} = \frac{\partial p_p(x,t)}{\partial x} + \frac{\partial p_c(x,t)}{\partial x}$$

$$= -\frac{b_1}{L_p}\cosh\left(\frac{x+u}{L_p}+\frac{a_1 D_p t}{L_p}\right) + \frac{a_1}{2}\,p_c(x,t)$$

$$+\frac{c_1 e^{a_1(x+u)/2}}{a_1+\sqrt{a_1{}^2+4/L_p{}^2}}\left\{\left[e^{-(x+u)Z_1-Z_2{}^2} + e^{(x+u)Z_1-Z_3{}^2}\right]\right.$$

$$\Big/ \sqrt{\pi D_p t} + Z_1 \left[ \operatorname{erfc}(Z_3)\, e^{(x+u)Z_1} - \operatorname{erfc}(Z_2)\, e^{-(x+u)Z_1} \right] \Bigg\} \quad (93)$$

where $Z_1 \equiv \sqrt{1/L_p^2 + a_1^2/4}$, $Z_2 \equiv -(x+u) \Big/ 2\sqrt{D_p t} + \sqrt{t/\tau_p + a_1^2 D_p t/4}$

$$Z_3 \equiv -(x+u) \Big/ 2\sqrt{D_p t} - \sqrt{t/\tau_p + a_1^2 D_p t/4},$$

The solutions obtained for, $p_n(x,t) \dfrac{\partial p_n(x,t)}{\partial x}$, will be discussed later and numerically calculated for various locations and states of switching of the device.

(B) Solutions for $p_2$-region

By considering assumptions (a) through (h), equation (67) can be rewritten as:

$$D_n \left( \frac{\partial^2}{\partial x^2} + \frac{\partial 2}{\partial y^2} \right) n_p = \frac{\partial n_p}{\partial t} + \frac{n_p}{\tau_n} \quad (94)$$

Assuming that the variables are separable as discussed earlier, the function $n_p(x,y,t)$ can be separated as:

$$n_p(x,y,t) = \sum_{\substack{k=o \\ k \text{ even}}}^{\infty} \cos \frac{k\pi y}{L} f_k(x,t) \quad (95)$$

The choice of "$\cos \frac{k\pi y}{L}$" and "k" even is to satisfy boundary condition (B).

Putting equation (95) into equation (94), one obtains:

$$D_n \left( \frac{\partial^2}{\partial x^2} - \frac{k^2\pi^2}{L^2} \right) n_p = \frac{\partial n_p}{\partial t} + \frac{n_p}{\tau_n} \qquad (96)$$

or

$$\frac{\partial^2 f_k}{\partial x^2} = a f_k + b \frac{\partial f_k}{\partial t} \qquad (97)$$

where, $a \equiv \frac{1}{L_n^2} + \frac{k^2\pi^2}{L^2}$, $\qquad b \equiv \frac{1}{D_n}$.

Assuming:

$$f_k(x,t) = f_k(x,o) + g_k(x,t) \qquad (98)$$

$\Sigma \cos \frac{k\pi y}{L} f_k(x,0)$ is the initial function of $n_p(x,y,t)$, and is obtained as equation (34). $g_k(x,t)$ is the time-dependent part of $n_p(x,y,t)$.

Introducing equation (98) into equation (97), one may separate time-independent terms and time-dependent terms. The time-independent terms have already been solved, and the unsolved part of the equation (the time-dependent term) is:

$$\frac{\partial^2 g_k}{\partial x^2} = a\, g_k + b \frac{\partial g_k}{\partial t} \qquad (99)$$

We should solve equation (99) in the way that $n_p(x,y,t)$ meets conditions (A) through (E). For $g_k(x,t)$, condition (A) should be

modified as:

(A') $g_k(o,o) = 0$

One may modify condition (A') further as

(A") $g_k(x,o) = 0$

which means the time-dependent function $g_k(x,t)$ doesn't exist in any place initially.

Conditions (D) and (E) are now considered as boundary values, which are descriptions of gradients of $n_p(x,y,t)$:

$$(D') \quad \left.\frac{\partial n_p(x,y,t)}{\partial x}\right|_{x=o} = \frac{J_n(x=o)}{qD_n}$$

$$(E') \quad \left.\frac{\partial n_p(x,y,t)}{\partial x}\right|_{x=w} = \frac{J_{Gn}}{qD_n} \qquad 0<y<\ell_1, \quad \ell_2<y<L$$

where $J_n$ is the electron current density, $J_{Gn}$ is the electron current density at the gates. Gate current $I_G$ is the current necessary to turn on the device, which can be turned on only when $I_G$ is larger than a certain value.

Since conditions (D') and (E') involves time constants, we may rewrite conditions (D') and (E') for the boundary values of time-dependent function $g_k(x,t)$ in a time interval:

$$(D') \quad \left.\frac{\partial g_k(x,t)}{\partial x}\right|_{x=o} = c_o \qquad c_o > 0$$

$$(E'') \quad \left.\frac{\partial g_k(x,t)}{\partial x}\right|_{x=\bar{w}} = -c_{\bar{w}} \qquad c_{\bar{w}} > 0$$

Boundary values $c_o$, $c_{\bar{w}}$ together with $c_1$ in Section (A) for $n_1$-region are fixed for certain time intervals, but will be modified at the end of each interval as one is checking with the conservation of currents (condition (D) and (E) ).

Once again, the Laplace transform is found to be a good technique for solving equation (99) subject to conditions (A"), (C), (D"), and (E"). By taking the Laplace transform, equation (99) may be rewritten as:

$$\frac{\partial^2}{\partial x^2} G_k(x,s) = a_s \, G_k(x,s) \tag{100}$$

where

$$G_k(x,s) \equiv \mathcal{L}\left\{g_k(x,t)\right\}$$

$$a_s \equiv a + bs$$

The boundary conditions now becomes:

$$(A'') \quad \lim_{s \to \infty} s \, G_k(x,s) = 0$$

$$(D'') \quad \lim_{s \to 0} s \left.\frac{\partial G_k}{\partial x}\right|_{x=0} = c_o \, e^{-\sqrt{a}\omega} \qquad \omega > \bar{w}$$

$$(E'') \quad \lim_{s \to \infty} s \frac{\partial G_k}{\partial x}\bigg|_{x=\bar{w}} = -c_{\bar{w}} \; e^{-\sqrt{a}\omega} \quad \omega > \bar{w}$$

Condition (A") concerns the initial value of $G_k(x,s)$, while condition (E") concerns the initial value of $\partial G_k(x,s)/\partial x$ at x=w which is proportional to the initial value of gate current $I_G$. Condition (D") concerns the final value of $\partial G_k(x,s)/\partial x$ at x=o for certain interval which is based on the same argument as in Section (A) for condition (D"). Parameter "$\omega$" is chosen so that $G_k(x,s)$ will carry it, and the choice of its value will ensure that condition (C) is satisfied. Expression "$e^{-\sqrt{a}\omega}$" is chosen to ensure fast convergence when evaluating the $\sum_{\substack{k=o \\ k \text{ even}}}^{\infty}$ series numerically (note, $a = 1/L_n^2 + k^2\pi^2/L^2$).

The solution of equation (100) should be a combination of terms in the form of $e^{\pm\sqrt{a}s(\bar{w} - x)}$, $e^{\pm\sqrt{a}s(\omega-x)}$, or $e^{\pm\sqrt{a}s\,x}$.
A form found appropriate for $G_k(x,s)$ is

$$G_k(x,s) = A_1 \, e^{-\sqrt{a}s(\omega-x)} - A_2 \sinh \sqrt{a}s\, x \qquad (101)$$

which is mathematically easier than other forms for calculating the inverse Laplace transform of $G_k(x,s)$. $A_1$, $A_2$, are coefficients to be determined. By defferentiating equation (101), one has

$$\frac{\partial G_k}{\partial x} = \sqrt{a}s \left(A_1 \, e^{-\sqrt{a}s(\omega-x)} - A_2' \cosh \sqrt{a}s\, x \right) \Big/ \cosh \sqrt{a}s\, \bar{w} \qquad (102)$$

where $A_2' \equiv A_2 \cosh \sqrt{a_s}\,\bar{w}$

$$\left.\frac{\partial G_k}{\partial x}\right|_{x=o} = \sqrt{a_s}\,(A_1\, e^{-\sqrt{a_s}\omega} - A_2' \;/\; \cosh \sqrt{a_s}\,\bar{w}) \tag{103}$$

$$\left.\frac{\partial G_k}{\partial x}\right|_{x=w} = \sqrt{a_s}\,(A_1\, e^{-\sqrt{a_s}\,(\omega-\bar{w})} - A_2') \tag{104}$$

Condition (D") and equation (103), yields

$$A_1\, e^{-\sqrt{a}\omega} - A_2' \;/\; \cosh \sqrt{a}\,\bar{w} = c_o\, e^{-\sqrt{a}\omega} / s\sqrt{a} \tag{105}$$

while condition (E") and equation (104), yields

$$A_2' = c_{\bar{w}}\; e^{-\sqrt{a}\omega} / s\sqrt{a_s}$$

$$\text{Thus,} \quad A_2 = \frac{c_{\bar{w}}\, e^{-\sqrt{a}\omega}}{s\sqrt{a_s}\,\cosh \sqrt{a_s}\,\bar{w}} \tag{106}$$

$$\text{and,} \quad A_1 = \frac{c_o}{s\sqrt{a}} + \frac{c_{\bar{w}}}{s\sqrt{a_s}\,\cosh \sqrt{a}\,\bar{w}} \tag{107}$$

$A_1$ and $A_2$ obtained are both positive, which ensures that $G_k(x,s)$ of equation (101) will always be positive. This is a necessary condition to have the number of electrons $n_p(x,y,t)$ come out positive.

Now,

$$G_k(x,s) = \left( \frac{c_o}{s\sqrt{a}} + \frac{c_{\overline{w}}}{s\sqrt{a_s}\cosh \sqrt{a}\,\overline{w}} \right) e^{-\sqrt{a_s}\,(\omega-x)}$$

$$- \frac{}{s\sqrt{a_s}\cosh \sqrt{a_s}\,\overline{w}} \sinh \sqrt{a_s}\,x \qquad (108)$$

The inverse Laplace transform of this equation is based on the following inverse transforms:

$$I_1 = \mathcal{L}^{-1}\left\{ \frac{e^{-\sqrt{a_s}\,(\omega-x)}}{\sqrt{a_s}} \right\} = \mathcal{L}^{-1}\left\{ \frac{e^{-\sqrt{s}+a/b \;.\; \sqrt{b}\,(\omega-x)}}{\sqrt{b}\,\sqrt{s+a/b}} \right\}$$

Since $a_s \equiv a + bs$. From equation 5.6(6) of Bateman's Table[38],

$$\mathcal{L}^{-1}\left\{ \frac{e^{\sqrt{s}\alpha}}{\sqrt{s}} \right\} = \frac{1}{\sqrt{\pi t}} e^{-\alpha^2/4t}$$

and

$$\mathcal{L}^{-1}\left\{ G(s+\omega_o) \right\} = e^{-\omega_o t}\, \mathcal{L}^{-1}\left\{ G(s) \right\}$$

the inverse transform becomes

$$I_1 = \frac{e^{-at/b}}{\sqrt{b\pi t}}\, e^{-b(\omega-x)^2/4t} \qquad (109)$$

Also,

$$I_2 = \mathcal{L}^{-1}\left\{\frac{e^{-\sqrt{a}_s\ (\omega-x)}}{s}\right\}$$

$$= \mathcal{L}^{-1}\left\{e^{-\sqrt{s+a/b}\ \sqrt{b}\ (\omega-x)} \Big/ [(s+a/b)-a/b]\right\}$$

$$= \frac{1}{2}\left[ e^{(\omega-x)\ \sqrt{a}}\ \text{erfc}\ \left(\frac{\omega-x}{2}\sqrt{\frac{b}{t}} + \sqrt{\frac{at}{b}}\ \right)\right.$$

$$\left. + e^{-(\omega-x)\ \sqrt{a}}\ \text{erfc}\ \left(\frac{\omega-x}{2}\sqrt{\frac{b}{t}} - \sqrt{\frac{at}{b}}\ \right)\right] \qquad (110)$$

The last equality is shown in equation 5.6(6) of Bateman's Table.[38]

Also,

$$I_3 = \mathcal{L}^{-1}\left\{\frac{\sinh \sqrt{a}_s\ x}{\sqrt{a}_s \cosh \sqrt{a}_s\ \bar{w}}\right\}$$

$$= \mathcal{L}^{-1}\left\{(\sinh \sqrt{s+a/b}\ \sqrt{b}\ x) \Big/ (\sqrt{b}\ \sqrt{s+a/b}\ \cosh \sqrt{s+a/b}\ \sqrt{b}\ w)\right\}$$

$$= -e^{-at/b}\ \theta_1\left(\frac{x}{2\bar{w}}\ \middle|\ \frac{j\pi t}{w^2 b}\right) / b\bar{w}$$

$$= -\frac{e^{-at/b}}{b\bar{w}}\left(\frac{\pi t}{b\pi^2}\right)^{-\frac{1}{2}}\left[\sum_{r=-\infty}^{\infty} (-1)^r\ e^{-b\bar{w}^2\ (x/2\bar{w}+r-\frac{1}{2})^2/t}\right] \qquad (111)$$

The third equality is shown in equation 5.9(34) of Bateman's Table[38], $\theta_1(v|\tau)$ is Theta function of first kind. The fourth equality is shown as the last equation on page 387 of the same Table.

Note, equation (110) is the inverse Laplace transform good for the

first term of equation (108). Equations (109) and (111) are good for the second and the third terms of equation (108) respectively, if variable "s" is in the denominators of equations (109) and (111). By the property of:

$$\mathcal{L}^{-1}\left\{\frac{G(s)}{s}\right\} = \int_0^t g(x)\,dx$$

and observing that the time functions of equations (109) and (111) are of the same form, the inverse transforms $I_1$, $I_3$ can all become directly applicable to equation (108) by:

$$I_4 = \int_0^t \frac{e^{-\alpha x-\beta/x}}{\sqrt{x}}\,dx \qquad \alpha.\beta>0$$

$$= 2\int^{\sqrt{t}} e^{-\alpha T^2-\beta/T^2}\,dt \qquad \text{by } x=T^2$$

$$= \frac{1}{2}\sqrt{\frac{\pi}{\alpha}}\left[e^{2\sqrt{\alpha\beta}}\,\operatorname{erf}\left(\sqrt{\alpha t}+\sqrt{\beta/t}\right)\right.$$

$$\left. + e^{-2\sqrt{\alpha\beta}}\,\operatorname{erf}\left(\sqrt{\alpha t}-\sqrt{\beta/t}\right)-2\sinh 2\sqrt{\alpha\beta}\right] \qquad \sqrt{\alpha}.\sqrt{\beta}>0 \qquad (112)$$

The integration performed to give the last equality can be found as equation 7.4. 33 of HMF[39].

Therefore, the inverse Laplace transform of equation (108) can be obtained by $I_2$ and modified $I_1$, $I_3$ when considering $I_4$,

$$g_k(x,t) = \mathcal{L}^{-1}\left\{G_k(x,s)\right\}$$

$$= \frac{c_o}{2\sqrt{a}} \left[ e^{(\omega-x)\sqrt{a}} \operatorname{erfc}\left( \frac{\omega-x}{2}\sqrt{\frac{b}{t}} + \sqrt{\frac{at}{b}} \right) \right.$$

$$\left. + e^{-\sqrt{a}(\omega-x)} \operatorname{erfc}\left( \frac{\omega-x}{2}\sqrt{\frac{b}{t}} - \sqrt{\frac{at}{b}} \right) \right]$$

$$+ \frac{c_w}{2\sqrt{a}\cosh\sqrt{a}\,\bar{w}} \left[ e^{\sqrt{a}(\omega-x)} \operatorname{erf}\left( \sqrt{\frac{at}{b}} + \frac{\omega-x}{2}\sqrt{\frac{b}{t}} \right) \right.$$

$$\left. + e^{-\sqrt{a}(\omega-x)} \operatorname{erf}\left( \sqrt{\frac{at}{b}} - \frac{\omega-x}{2}\sqrt{\frac{b}{t}} \right) - 2\sinh\sqrt{a}(\omega-x) \right]$$

$$- \frac{c_{\bar{w}}\, e^{-\sqrt{a}\omega}}{2\sqrt{a}} \sum_{r=-\infty}^{\infty} (-1)^r \, e^{2\sqrt{a}w\left|x/2\bar{w}+r-\frac{1}{2}\right|} \operatorname{erf}\left( \sqrt{\frac{at}{b}} + \bar{w}\left|\frac{x}{2\bar{w}} + r - \tfrac{1}{2}\right|\sqrt{\frac{b}{t}} \right)$$

$$+ e^{-2w\sqrt{a}\left|x/2\bar{w}+r-\frac{1}{2}\right|} \operatorname{erf}\left( \sqrt{\frac{at}{b}} - w\left|\frac{x}{2w} + r-\tfrac{1}{2}\right|\sqrt{\frac{b}{t}} \right)$$

$$\left. - \sinh 2\sqrt{a}\left|\frac{x}{2w} + r-\tfrac{1}{2}\right|\bar{w} \right] \qquad (113)$$

or, to make numerical calculations more efficient, equation (113) may be rewritten as:

$$g_k(x,t) = \frac{1}{2\sqrt{a}} \left\{ e^{\sqrt{a}(\omega-x)} \left( c_o - \frac{c_{\bar{w}}}{\cosh\sqrt{a}\,\bar{w}} \right) \operatorname{erfc}(Z_{p1}) \right.$$

$$\left. + e^{-\sqrt{a}(\omega-x)} \left( c_o + \frac{c_{\bar{w}}}{\cosh\sqrt{a}\,\bar{w}} \right) (2 - \operatorname{erfc}(Z_{p2})) \right.$$

$$+ c_{\overline{w}}\, e^{-\sqrt{a}\omega} \sum_{r=-\infty}^{\infty} (-1)^r \left[ e^{2\sqrt{a}\, Z_{p3}}\, \mathrm{erfc}\left(\sqrt{\frac{at}{b}} + Z_{p3}\sqrt{\frac{b}{t}}\right) \right.$$

$$\left. -\left(e^{-2\sqrt{a}\, Z_{p3}}\right)\left(2 - \mathrm{erfc}\left(\sqrt{\frac{at}{b}} - Z_{p3}\sqrt{\frac{b}{t}}\right)\right)\right] \Bigg\} \qquad (114)$$

where $Z_{p1} \equiv \sqrt{at/b} + 0.5\,(\omega - x)\,\sqrt{b/t}$,

$Z_{p2} \equiv \sqrt{at/b} - 0.5\,(\omega - x)\,\sqrt{b/t}$, $Z_{p3} \equiv w\left|x/2w - r - \frac{1}{2}\right|$

Note, when checking equation (113) or (114), we may find:

$$\lim_{t \to o} g_k(x,t) = 0$$

$$\lim_{t \to \infty} g_k(x,t) = \text{constant of time}$$

which means $g_k(x,t)$ is non-existing before switching and saturated after switching.

Therefore, the minority carrier concentration in the $p_2$-region is:

$$n_p(x,y,t) = \sum_{\substack{k=o \\ k \text{ even}}}^{\infty} \cos\frac{k\pi y}{L}\, [f_k(x,0) + g_k(x,t)] \qquad (115)$$

In order to calculate the current density of minority carriers in the $p_2$-region, it is necessary to find the gradients of $n_p(x,y,t)$:

$$\frac{\partial n_p(x,y,t)}{\partial x} = \sum_{\substack{k=o \\ k \text{ even}}}^{\infty} \cos\frac{k\pi y}{L} \frac{\partial f_k(x,o)}{\partial x} + \sum_{\substack{k=o \\ k \text{ even}}}^{\infty} \cos\frac{k\pi y}{L} \frac{\partial g_k(x,t)}{\partial x} \tag{116}$$

The first term is calculated as equation (39), the second term can be calculated by:

$$\frac{\partial g_k(x,t)}{\partial x} = \frac{1}{2\sqrt{a}} \left\{ (c_o - \frac{c_{\bar{w}}}{\cosh \sqrt{a}\,\bar{w}}) e^{\sqrt{a}(\omega-x)} \left[-\sqrt{a}\,\text{erfc}\,(Z_{p1}) + \sqrt{\frac{b}{t\pi}}\, e^{-Z_{p1}^2}\right] \right.$$

$$+ (c_o + \frac{c_{\bar{w}}}{\cosh \sqrt{a}\,\bar{w}}) e^{-\sqrt{a}(\omega-x)} \left[\sqrt{a}(2-\text{erfc}(Z_{p2})) + \sqrt{\frac{b}{t\pi}}\, e^{-Z_{p2}^2}\right]$$

$$+ c_{\bar{w}}\, e^{-\sqrt{a}\omega} \sum_{r=-\infty}^{\infty} (-1)^r \left( e^{2\sqrt{a}Z_{p3}} \left[\sqrt{a}\,\text{erfc}(Z_{p4}) - \sqrt{\frac{b}{t\pi}}\, e^{-Z_{p4}^2}\right] \right.$$

$$\left. \left. + e^{-2\sqrt{a}Z_{p3}} \left[\sqrt{a}(2-\text{erfc}(Z_{p5})) - \sqrt{\frac{b}{t\pi}}\, e^{-Z_{p5}^2}\right] \right) \right\} \tag{117}$$

where $Z_{p4} \equiv \sqrt{at/b} + Z_{p3}\sqrt{b/t}$, $Z_{p5} \equiv \sqrt{at/b} - Z_{p3}\sqrt{b/t}$.

$$\frac{\partial n_p(x,y,t)}{\partial y} = -\sum_{\substack{k=o \\ k \text{ even}}}^{\infty} \frac{k\pi}{L} \sin\frac{k\pi y}{L} \left[f_k(x,o) + g_k(x,t)\right] \tag{118}$$

The solutions obtained, $n_p(x,y,t)$, $\partial n_p(x,y,t)/\partial x$, $\partial n_p(x,y,t)/\partial y$ will be discussed later with numerical calculations for various locations or states of switching of the device.

Numerical Calculation of the Dynamic Case

In the previous Section, equations (92) and (93) derived for the $n_1$-region and equations (115), (116), and (118) were derived for the $p_2$-region. Now, using these equations, one may calculate numerically the minority carrier distributions and current density with the aid of the following algorithm: (1) Establish the operating parameters of the device before triggering. (2) Determine the appropriate gate current $I_G$ to trigger the device. (3) Adjust the operating parameters to satisfy boundary conditions (D) and (E) for each time interval. Continue the above steps until the values obtained show a saturated condition, at that point the device stays "on". More specifically:

(1) Parameters before triggering

Set the device in the same operation conditions as in Example 1, for the static case, namely, $I_k = 4.4\times10^{-7}$ Amp in the forward blocking case without gate current, which means $I_{J1} = I_{J2} = I_{J3} = 4.4\times10^{-7}$ Amp. From the equality

$$I_{J1} = \frac{H\,L\,q\,D_p\,p_{no}}{L_p}\left(e^{qV_{J1}/kT} - 1\right)\coth\frac{U-u}{L_p} \qquad (119)$$

one obtains,

$$p_{nU} = p_{no}\,(e^{qV_{J1}/kT} - 1) = I_{J1}\,L_p \,/\, (HLqD_p \coth\frac{U-u}{L_p}) \qquad (120)$$

Using the values of H, L, W, w, $\ell_1$ and parameters of $L_n$, $D_n$, $\tau_n$ from Example 1 of Section IV in Chapter II, (in addition, knowing the parameters $D_p$=13 $cm^2$/sec.) $L_p$=1.14x$10^{-3}$ cm, q=1.6x$10^{-19}$ Coulomb). One finds from equation (120):

$$p_{nU} = 1.81 \times 10^{23} \times I_{J1} \qquad (120A)$$

and,

$$E_1 = I_{J1} / HLq\,\mu_p\,p_n = 8.8 \times 10^7\ I_{J1} \qquad (121)$$

From equation (119), $V_{J1}$ = 0.69 V.

In order to evaluate the switching characteristics of the device, one has to connect this device in series with a load $R_c$, and apply DC power supply of voltage $E_v$. The governing equation is:

$$E_v = IR_c + V_{J1} + V_{J2} + V_{J3} \qquad (122)$$

where I is the current that passes through the device. Assuming $E_v$ = 20 V, $R_c$ = 50 Ω, and $V_{J1}$ = 0.69 V, $V_{J3}$ = 0.6 V, (as calculated earlier), one obtains:

$$V_{J2} = E_v - IR_c - V_{J1} - V_{J3} = 18.71 \text{ V}$$

One may now evaluate the depletion length of u of $n_1$-region in

junction $J_2$:

$$u = -\sqrt{2k_s\varepsilon_o V_{J2}/qN_n} = -\sqrt{12.9636\, V_{J2}} \times 10^{-4} \text{ cm} \tag{123}$$

$u = 1.56\times10^{-3}$ cm for this $V_{J2}$ specified.

Parameter $c_1$ may be evaluated from $p_n(x,o)$ of equation (81):

$$c_1 = \left.\frac{\partial p_n}{\partial x}\right|_{x=-u} = -\frac{p_{nU}}{L_p \sinh(\frac{U-u}{L_p})} = -1.17\times10^{23} \times I_{J1} \Big/ \sinh\frac{U-u}{L_p} \tag{124}$$

Choosing $U=3\times10^{-3}$ cm as a typical thickness of $n_1$-region, the only unknown parameters are then $I_{J1}$ and $V_{J2}$.

The parameters for the $p_2$-region before switching are specified in Example I of the static analysis.

(2) Establishing a sufficient gate current $I_G$

A gate current $I_G$ is considered as sufficient to turn on the device if the time-dependent part of $n_p(x,y,t)$ is much larger than the time-independent part, this occurs when $t = 1o^{-7}$ to $10^{-6}$ sec. With $I_G$ specified, $c_w$ becomes,

$$c_w = -\left.\frac{\partial g_k(x,t)}{\partial x}\right|_{x=\bar{w}} = \frac{I_{Gn}}{2qD_n H\ell_1} = 1.152\times10^{22}\, I_{Gn} \tag{125}$$

As calculated by A.Y.C. Yu[40], the minority carrier current $I_{Gn}$ at

the gate contacts with semiconductor of

$p=10^{16}$ $cm^{-3}$ is

$$I_{Gn} = 10^{-6} \times I_G$$

Therefore,

$$c_w = 1.15\times10^{16} I_G \qquad (125A)$$

Numerically, a gate current is sufficient to turn on the device if $c_w$ (assigned by equation (125A) ensures the calculations of $n_p \gtrsim 4\times10^{11}$ $cm^{-3}$ and $\partial n_p/\partial x \simeq 5\times10^{13}$ at $y=2.52\times10^{-2}$ cm and $t = 10^{-7} \sim 10^{-6}$ sec. These numbers for $n_p$ and $\partial n_p/\partial x$ are obtained from Figures 8 and 9 respectively.

(3) Parameter Modifications after Time Intervals

When $I_G$ is sufficiently large, $I_{J2}$ and $I_{J3}$ will be greater than $I_{J1}$. After each time interval, one must then modify parameters to satisfy boundary conditions (D) and (E). From equations (76), (77) and (78), one may evaluate $I_{J1}$, $I_{J2}$, $I_{J3}$.

$$I_{J1} = 4.08\times10^{-18} \left[ 280 E_1 \, p_n(x=-U) - 7 \times \frac{\partial p_n}{\partial x}\bigg|_{x=-U} \right] \qquad (126)$$

$$I_{J2} = -2.856\times10^{-17} \frac{\partial p_n}{\partial x}\bigg|_{x=-u} + 2.48\times10^{-19} \int_o^{L/2} \frac{\partial p_n}{\partial x}\bigg|_{x=o} dy$$

$$= -2.856\times10^{-17} \frac{\partial p_n}{\partial x}\bigg|_{x=-u} + 6.32\times10^{-21} \left[ \frac{\partial f_o(o,o)}{\partial x} + \frac{\partial g_o(o,t)}{\partial x} \right] \qquad (127)$$

$$I_{J3} = 2.48\times10^{-19}\left\{(L/2-\ell_1)\left[\frac{\partial f_o(w,o)}{\partial x}+\frac{\partial g_o(w,t)}{\partial x}\right]\right.$$

$$+\sum_{\substack{k=2\\ k\ \text{even}}}^{\infty}\frac{L}{k\pi}\left(\sin\frac{k\pi}{2}-\sin\frac{k\pi\ell_1}{L}\right)\left[\frac{\partial f_k(w,o)}{\partial x}+\frac{\partial g_k(w,t)}{\partial x}\right]$$

$$\left.-\sum_{\substack{k=2\\ k\ \text{even}}}^{\infty}\frac{k\pi}{L}\sin\frac{k\pi\ell_1}{L}\int_w^W\left[f_k(x,o)+g_k(x,t)\right]dx\right\} \qquad (128)$$

When applying a sufficient $I_G$ for a given interval, there are always three possible cases to adjust the parameters:

(a) If $I_{J1}$ is the largest among $I_{J2}$ and $I_{J3}$, adjust $c_o$ so that $I_{J2} \geq I_{J1}$ and $I_{J3} \geq I_{J1}$.

(b) If $I_{J2}$ is the largest among $I_{J1}$ and $I_{J3}$, adjust $I_{J1}$ so that $I_{J1} \geq I_{J2}$, and adjust $c_o$ so that $I_{J3} \geq I_{J2}$.

(c) If $I_{J3}$ is the largest among $I_{J1}$ and $I_{J2}$, adjust $I_{J1}$ so that $I_{J1} \geq I_{J3}$, and adjust $c_o$ so that $I_{J2} \geq I_{J3}$.

The "interval" lengths are chosen so that the differences between $I_{J1}$, $I_{J2}$ and $I_{J3}$ are below a certain fixed percentage.

The numerical values of operating parameters can be found by using the algorithm mentioned above. (1) As $I_{J1} = I_k = 4.4\text{X}10^{-7}$ Amp. initially, then $p_{nU}$, $E_1$, $V_{J1}$, $V_{J2}$, u, $c_1$, are all known quantities. (2) With the computer program of Appendix C, one may find the sufficient gate current for switching to be, $I_G = 1\text{x}10^{-6}$ Amp. and $c_{\overline{w}} = 1.152\text{x}10^{-10}$ $cm^{-4}$. (3) With the computer program of Appendix D, one may calculate

the junction current at junction $J_2$ in $p_2$-region as $I_{J2}(n_p)$ = $2x10^{-4}$ Amp, and $C_o$ = $1x10^{19}$ $cm^{-4}$, when the gate current triggers the device for an interval of $1o^{-7}$ sec. With the computer program of Appendix D, one may obtain $I_{J3}$ = $1.1x10^{-1}$ Amp after $10^{-7}$ sec. Also with the computer program one finds $I_{J1}$ = $5.54x10^{-2}$ Amp, and the current at junction $J_2$ in $p_1$-region $I_{J2}(p_n)$ = $7.18x10^{-2}$ Amp after $1o^{-7}$ sec. Thus $I_{J2}$ = $I_{J2}(p_n)$ + $I_{J2}(p_n)$ = $7.2x10^{-2}$ Amp. Now adjust $I_{J1}$ = $1x10^{-1}$ Amp, $c_o$ = $1x10^{22}$ for these programs and set interval to be $2x10^{-7}$ sec. and one calculates these values successively until the solutions for the condition of saturation are obtained. These solutions were plotted in Figure 14 for the $n_1$-region, and Figure 15 for the $p_2$-region.

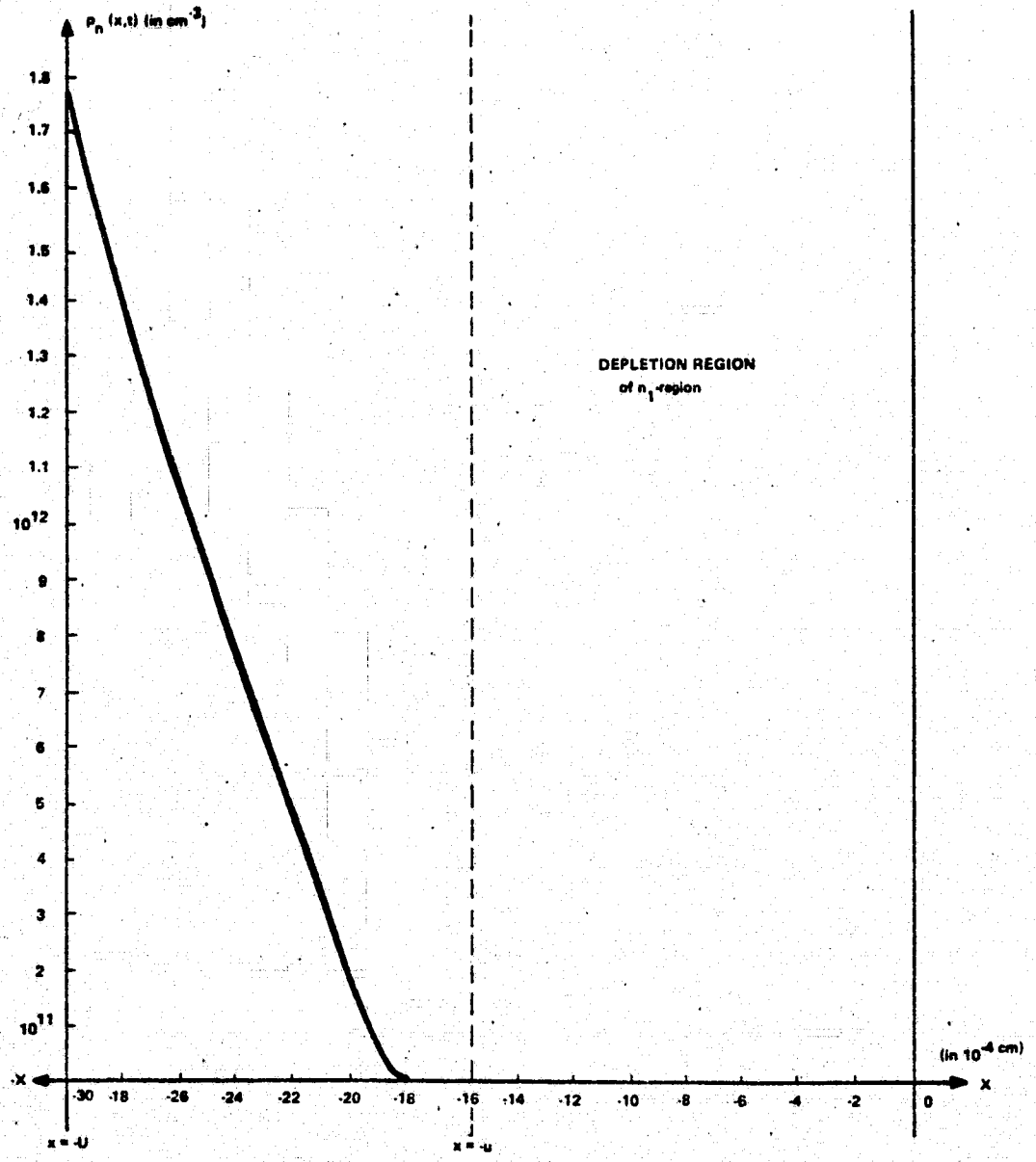


Figure 14 Minority Carrier Distribution when Triggering started ($t = 10^{-7}$ sec)

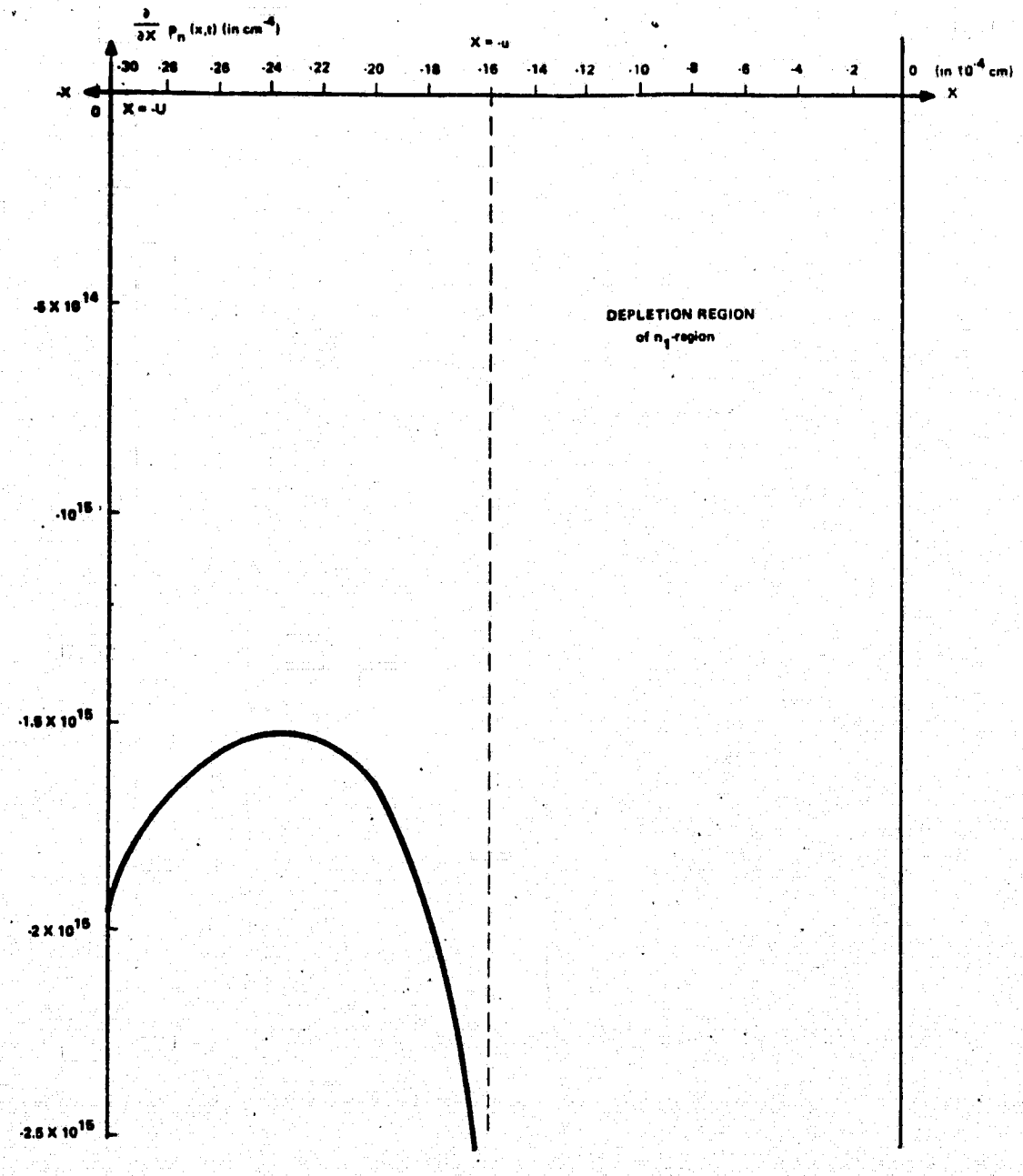


Figure 14B x-derivative of $p_n(x,t)$ in the $n_1$-region when Triggering started ($t = 10^{-7}$ sec.)

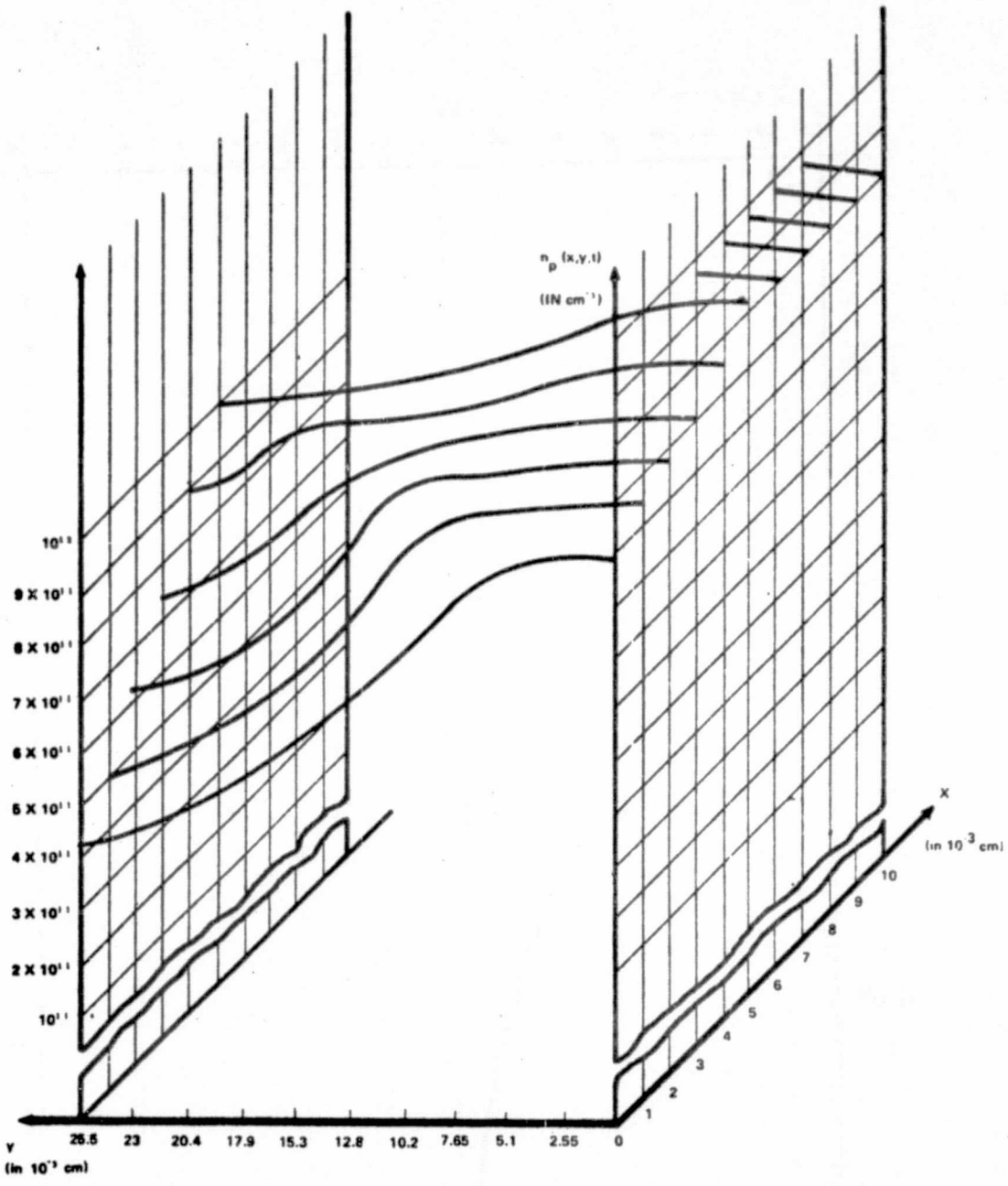


Figure 15A Minority Carrier Distribution $n_p(x,y,t)$ when Triggering starts ($t = 10^{-7}$ sec) (The way to read the curves is the same as that described for Figure 5.)

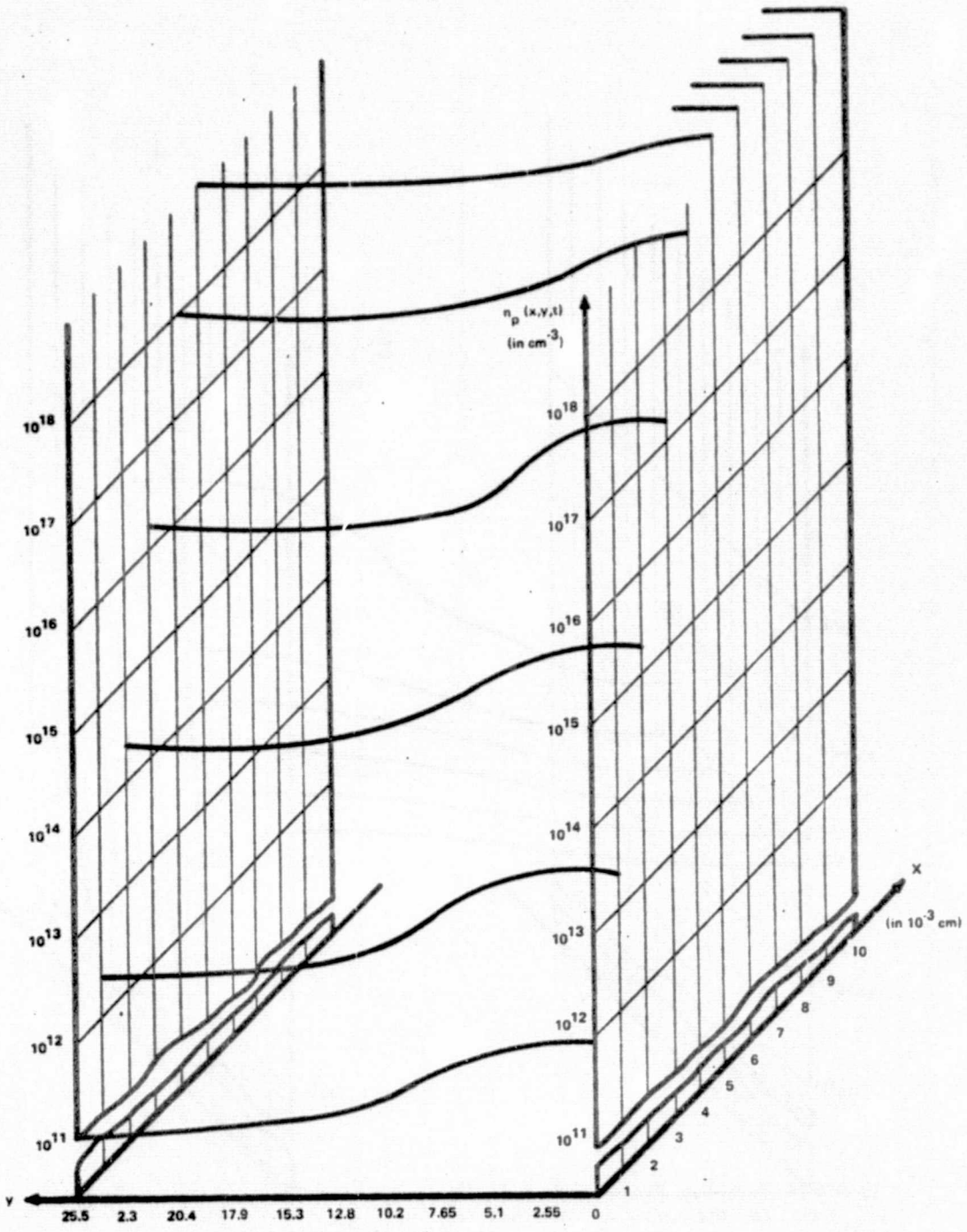


Figure 15B Minority Carrier Distribution $n_p(x,y,t)$ when the Device is Saturated in "ON" State. ($t=0^{-6}$ sec.)

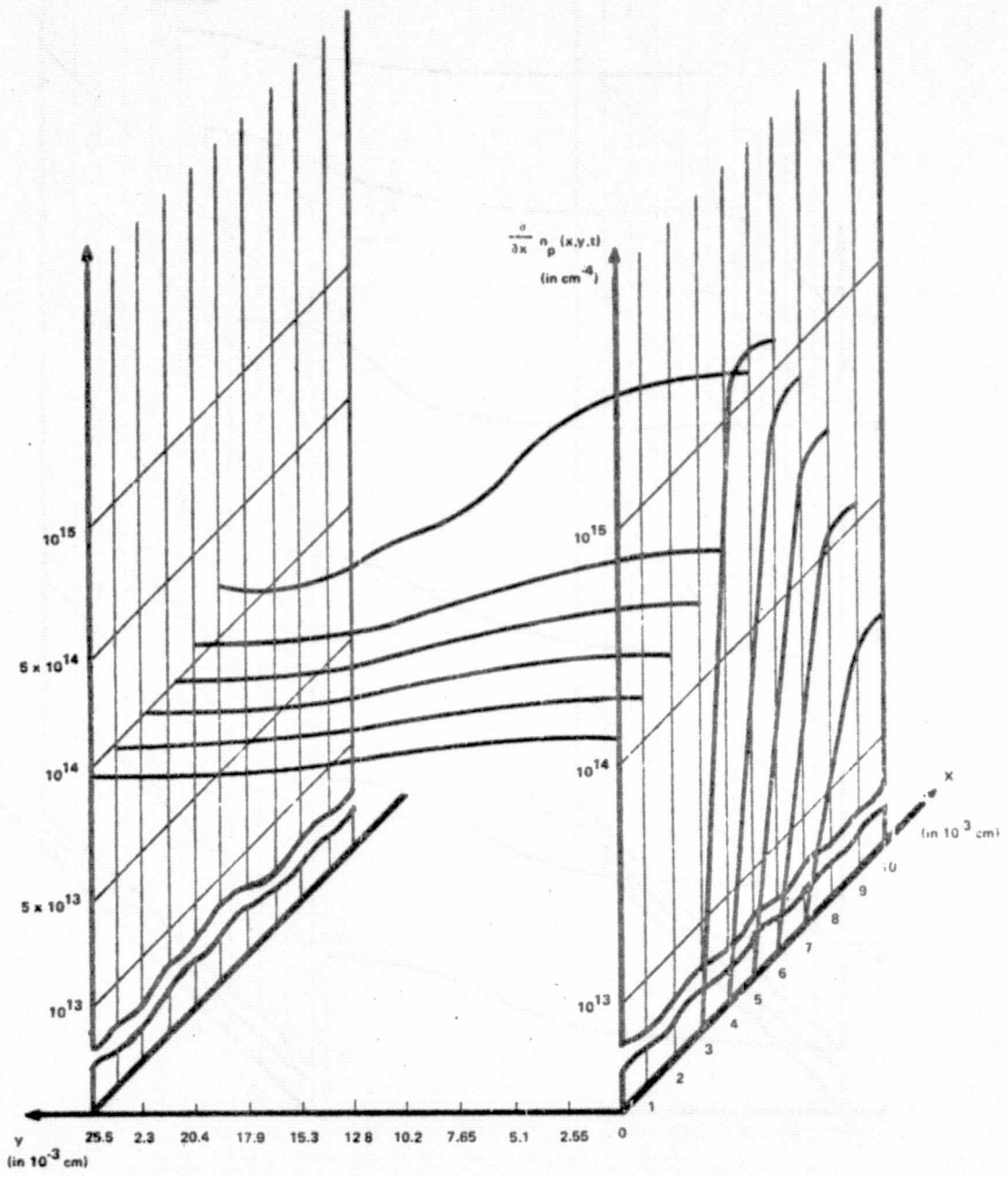


Figure 15C Minority Carrier Gradient Distribution $\frac{\partial n_\partial(x,y,t)}{\partial x}$ (i.e. $J_{nx}/qD_n$) when Triggering Starts. ($t=10^{-7}$ sec.)

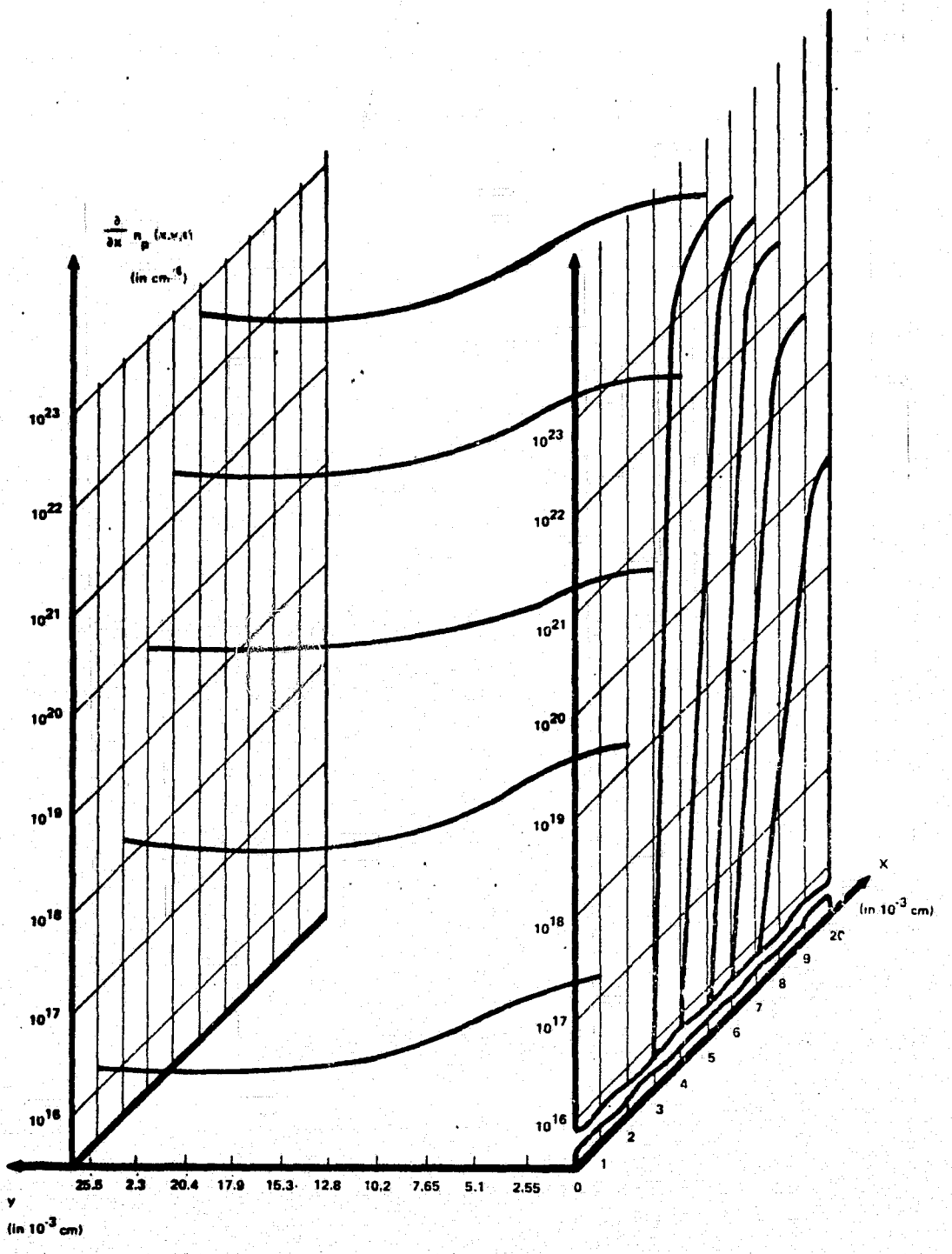


Figure 15D Minority Carrier Gradient Distribution $\frac{\partial}{\partial x} n_p(x,y,t)$ (i.e. $J_{nx}$) When the Device is Saturated in "ON" State. ($t=10^{-6}$ sec.)

# CHAPTER IV

## EXPERIMENTAL VERIFICATION

The lateral spreading of the turned-on area for a thyristor (Figure 16), was reported by N. Mapham in 1962,[41] who observed a time delay between the two gates when the device is turned-on at one gate and measured at the other. W.H. Dodson and R.L. Longini[16] subsequently measured the lateral time delay between probed islands using the configuration shown in Figure 17. The lateral voltage drop of forward conducting thyristors was measured by E.S. Yang[23] using a lumped simulating circuit as shown in Figure 18. In addition, as will be demonstrated further, since current density can be related to temperature generated in the device, an infrared microradiometer can also be used to map the thermal profile and give the current density distribution.[42]

These approaches outlined above however give an integrated value only, since the electrical measurements[41,16,23] can not describe differential values, and the microradiometer measurements[42] read only the "smeared" temperature on the surface. Because the switching of such a device can be accurately described by the activities of minority carriers driven in and out of the $p_2$-region, and because of the clear relationship of current density to temperature generated, it is possible to use the infrared technique to map the optical absorption and yield

Figure 16. A typical thyristor geometry. Areas shaded are ohmic contacts, the nonshaded surfaces are covered by oxide. Typical doping concentrations are:
$p_1 = 10^{19}$ cm$^{-3}$, $n_1 = 10^{14}$ cm$^{-3}$,
$p_2 = 10^{16}$ cm$^{-3}$, $n_2 = 10^{19}$ cm$^{-3}$

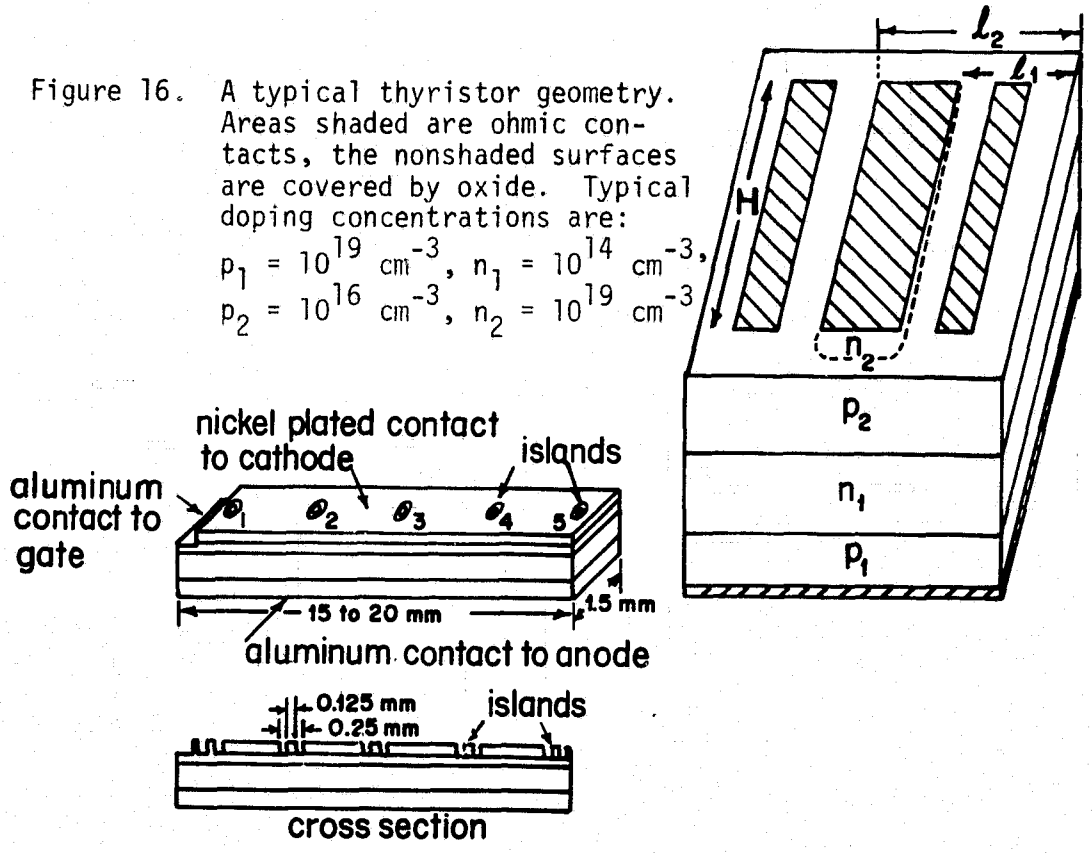


Figure 17. Device configuration. The island permitted the observation of the spread of the on-state.

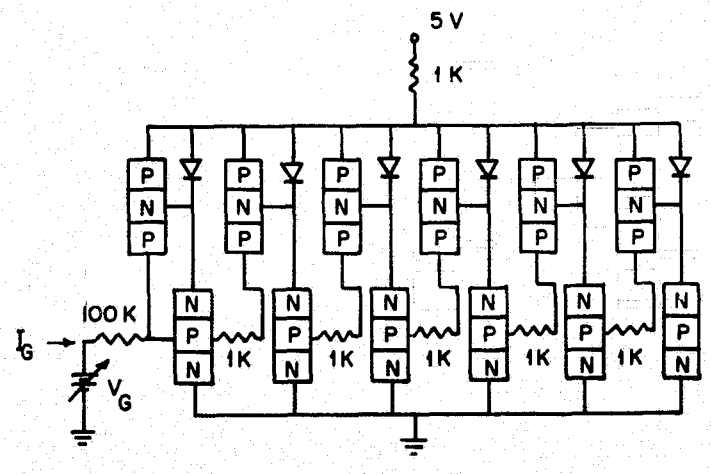


Figure 18. A two dimensional lumped model for a p-n-p-n device.

the thermal profile of the $p_2$-region so that one may obtain the current density distribution at each point of the device junction. This in turn will be sufficient to describe the spreading of the turned-on area and the hot-spots generated due to successive switching.[15] In this chapter the approach used in this project will be described, namely to employ a fine infra-red beam to map the thermal profile of semiconductor active devices. This is quite a novel technique. Infra-red micro radiometers were used in prior work, but only for surface measurements. This is the first time that an infra-red beam is used to scan and determine the differential temperature of an active device. From a knowledge of the temperature map, as will be shown, one can determine the current density distribution as well as other important parameters of the device. The development of the mapping technique itself used in this project is also novel and could be very important in determining hot spots, and device defects. The thermal profile of the $p_2$ region is based on the following two factors: (a) Infrared absorption rate of silicon depends on the temperature of silicon, (b) The major non-uniformity of current density is in the $p_2$-region. These factors will be discussed in the following paragraphs.

## Theoretical Background of the Temperature Measurement Technique

Near the absorption edge the optical absorption coefficient $\alpha$ can be expressed as[43,44]

$$\alpha \sim (h\nu - E_g)^{\frac{1}{2}} \tag{129}$$

for allowed direct transition, where h is Planck's constant and $\nu$ is the frequency of incident light. The energy band gap of silicon $E_g$ is temperature dependent[45], between $300^o$ to $600^o$k, with $dE_g/oT$ being about $-2.4 \times 10^{-4}$ eV/$^o$k. At $300^o$k, $E_g$ = 1.12 eV for silicon, therefore for an incident light of wavelenght $\lambda$ of 1.14 $\mu$m ( $\lambda = c/\nu = ch/E_g$), we will observe a temperature-sensitive absorption coefficient.

When the incident wavelength is less than 1.14 $\mu$m, absorption due to carriers being raised from the valence band to the conduction band becomes dominant; while when the incident wavelength is larger than 1.14 $\mu$m, free carriers associated with impurities and defects contribute the major absorption[46]. In addition, the absorption coefficient of free carriers $\alpha_{fc}$[19,47,48] is

$$\alpha_{fc} = \frac{2q^3}{4\pi^2 c^3 \underline{n}\, \varepsilon_o} \left( \frac{n}{\mu_n m_n^{*2}} + \frac{p}{\mu_p m_p^{*2}} \right) \tag{130}$$

Therefore carrier concentration dependence becomes explicit. In order to find the incident light to give the most temperature-sensitive absorption coefficient, it is necessary to find the spectral absorption coefficient of silicon wafers with various doping concentrations as a function of temperature.

For a small rectangular volume of silicon of area A, length L and resistivity $\rho_R$, electric power dissipation of current I in this volume is

$$P = I^2R = J^2\rho_R AL \tag{131}$$

Energy dissipated in time interval t is

$$\Delta E = P(\Delta t) = \rho_R AL\ J^2(\Delta t) \tag{132}$$

The equivalent heat is

$$\Delta Q = (\Delta E)/4.1840 \qquad \text{(in Joules)} \tag{133}$$

and the corresponding temperature change is

$$\Delta T = \frac{\Delta Q}{c_v\ n_m} \tag{134}$$

where $c_v = 3\ R_G\ C_{DP}$

$n_m = \frac{m}{28}$ (in moles)

and $R_G = 1.99$ Cal/mole-deg (gas constant)

$C_{DP}$ = Dulong - Petit constant. The value varies with temperatute T in $^oK$[49], between $300^o$ to $500^oK$, with a temperature proportion constant of approximately $4.17 \times 10^{-3}$.

m = mass = 2.42 for silicon

Therefore, in a time interval $\Delta t$, the temperature change in a

small volume of silicon of resistivity $\rho_R$ by the power dissipation of current density J is

$$\Delta T = 1.66 \times 10^{-7} \left( \frac{\rho_R}{C_{DP}} \right) J^2 \Delta t \qquad (135)$$

Note, the factor $(\rho_R/C_{DP})$ is temperature-dependent, but its variation in the temperature range of $300^0$ to $500^0$K is negligible.

Thermal conduction is a complicated problem because it is three-dimensional, involved with Fermi energy, mean free time, and differential thermoelectric power. The thermal conductivity is contributed by lattice, electronic or both lattice and electronic mechanism. It is related to doping concentrations[50] according to the relationship $np\mu_n\mu_p/(n\mu_n + p\mu_p)^2$. In the temperature range of concern, namely from $300^0$K to $600^0$K, the thermal conductivity for silicon with a doping level of $n = 10^{14}$ $cm^{-3}$ varies from 1.6 watt/cm-$^0$K to 0.52 Watt/cm-$^0$K approximately linearly[51]. Therefore, the thermal conductivities can be characterized for this problem as: (1) Thermal conductivities for the $p_1$ - or the $n_2$-regions are one thousandth or less than that of $n_1$ or $p_2$ regions (2) The thermal conductivity dropped to 30% when the temperature raised from $300^0$K to $600^0$K for the $n_1$-region. For a block of silicon of thermal conductivity $K_{th}$ with temperature gradient [grad (T)] the heat flow through the boundary is

$$Q_{th} = K_{th} \text{ grad } (T) \qquad (136)$$

Therefore the thermal conduction expressed by this factor $Q_{th}$ is negligible in the $p_1$- or $n_2$-regions with respect to that of $n_1$- or $p_2$-regions. The thermal conduction is negligible in the $n_1$-region with respect to the $p_2$-region as the temperature is raised from $300^{o}K$ to $600^{o}K$. One may conclude, from the effect of thermal conduction in the $p_1$-, $n_1$-, or $n_2$-regions, the thermal profiles formed in these regions are negligible compared to that in the $p_2$-regions.

Infrared Absorption Coefficients of Silicon as A Function of Temperature and Doping Concentrations

A literature search for data on absorption coefficients as a function of temperature and doping concentrations for silicon revealed that the available information for this work is incomplete, especially for the doping concentrations of major concern for thyristors, i.e., $p \simeq 10^{18}$ cm$^{-3}$, $n \simeq 10^{14}$ cm$^{-3}$. Therefore, it was necessary to conduct a series of experiments in order to determine the temperature and doping concentration dependence of absorption coefficients for various wavelengths.

A. Experiments in the wavelength range of 2.5 to 14 μm.

A Double Beam Infrared Spectrophotometer can scan through the near infrared by modifying the reflecting grating, ranging from 2.5 μm to 14 μm. Basically this instrument (Figure 19) splits the beam emanating from a glowbar light source into two beams. They are then a.c. chopped, and one of them (which is 90$^{o}$ out of phase with the other) passes through the silicon wafer, the other bypasses it and then they are detected by the same detector, the ratio of transmission intensity to the incident intensity is available. A reflection grating rotating in the optical path in front of the detector allows the detection of a particular wavelength. A few things need to be noticed when operating with this system: (1) The water vapor band around 6 μm disturbs the readout. This can be corrected by flushing nitrogen into this system to clear the water vapor, (2) The beams are around the size of 5 mm,

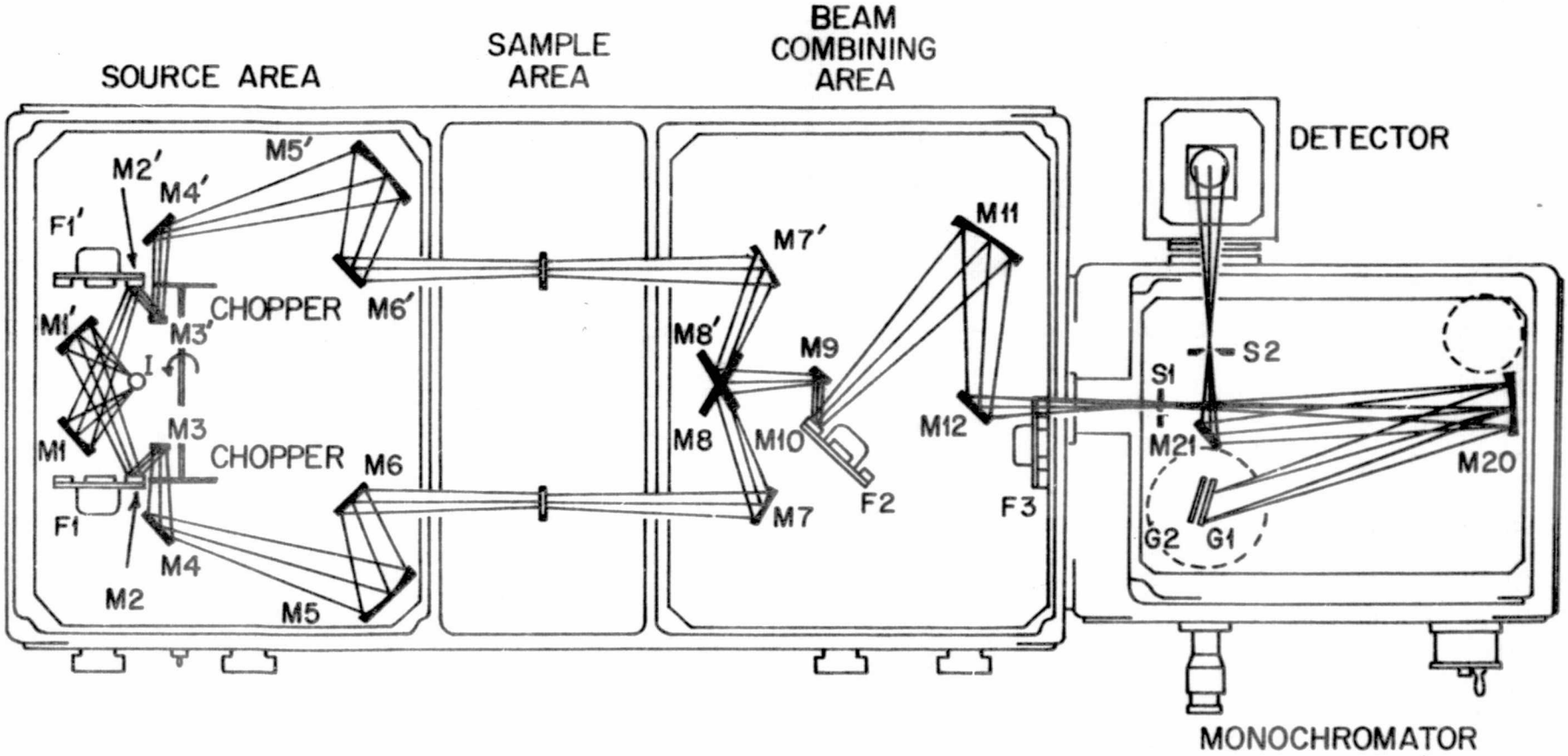


DOUBLE BEAM FAR INFRARED SPECTROPHOTOMETER

Figure 19. Optical Diagram

and can not be focused without disturbing the whole alignment. So, it is not suitable for use in mapping the thermal profile.

A sample holder was made to hold one-inch silicon wafers (Figure 20). A thermocouple was placed in contact with the wafer so as to have good control of the temperature of the wafer. Quartz was used for the windows because it has negligible optical absorption for the temperature and wavelength range of concern. The wafers used were cleaned and polished 0.02 cm thick silicon single crystal wafers with doping concentrations of $p = 10^{16}$ $cm^{-3}$, $p = 6x10^{18}$ $cm^{-3}$, $n = 5x10^{14}$ $cm^{-3}$, $n = 8x10^{18}$ $cm^{-3}$. Temperature variations were sampled as $25^{o}C$, $90^{o}C$, $145^{o}C$, and $220^{o}C$. The transmitted intensity changes relative to the intensity at room temperature were measured. This set of data shows that the intensity change varies with wavelength and with doping concentrations. For p-type silicon, major changes are around 3 μm and 12.5 μm, while for n-type silicon, major changes are around 4 μm only. None of these intensity changes give more than 10% range for all four types of silicon, which implies that this data can not be used to resolve temperature profiles satisfactorily when the wafer temperature changes from $25^{o}C$ to $250^{o}C$.

B. Experiments with wavelengths 1.15 μm and 2.0 μm.

An optical system as in Figure 21 was set up to measure optical absorption coefficients for monochromatic light.

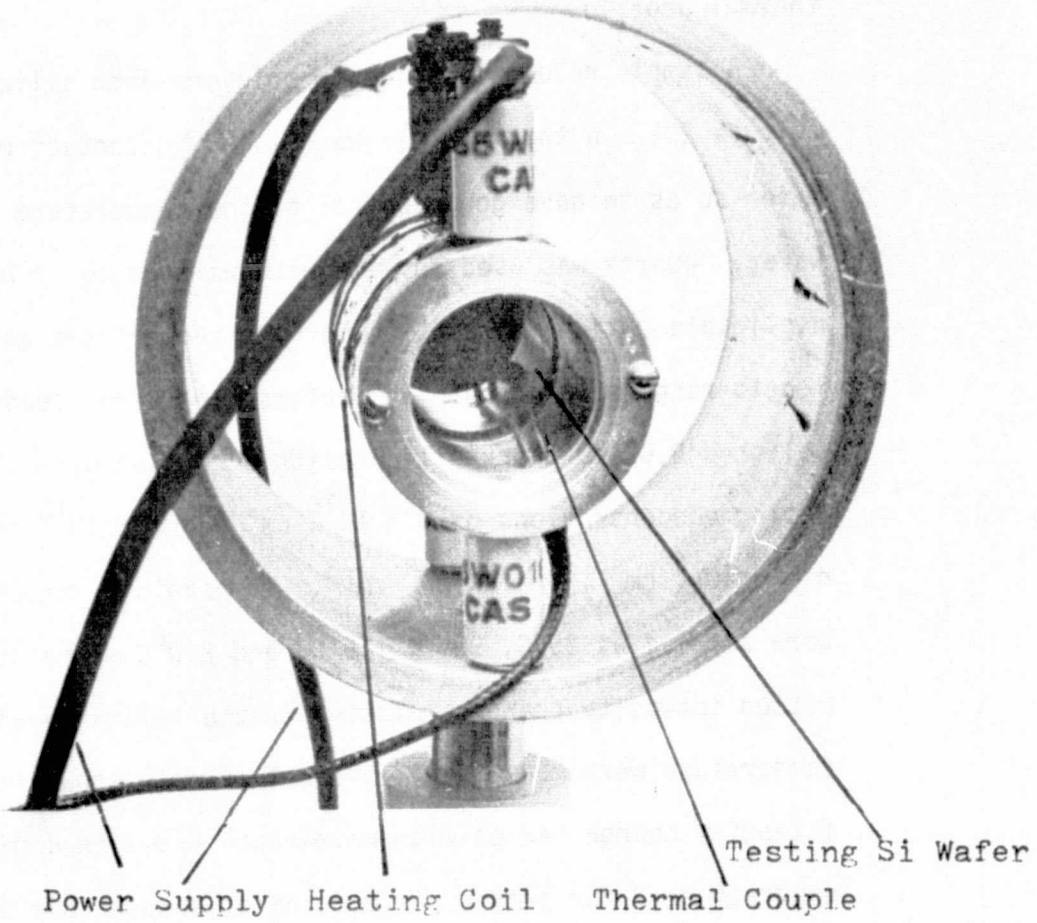


Figure 20 Sample Holder with Temperature Control and Probing Thermal Couple

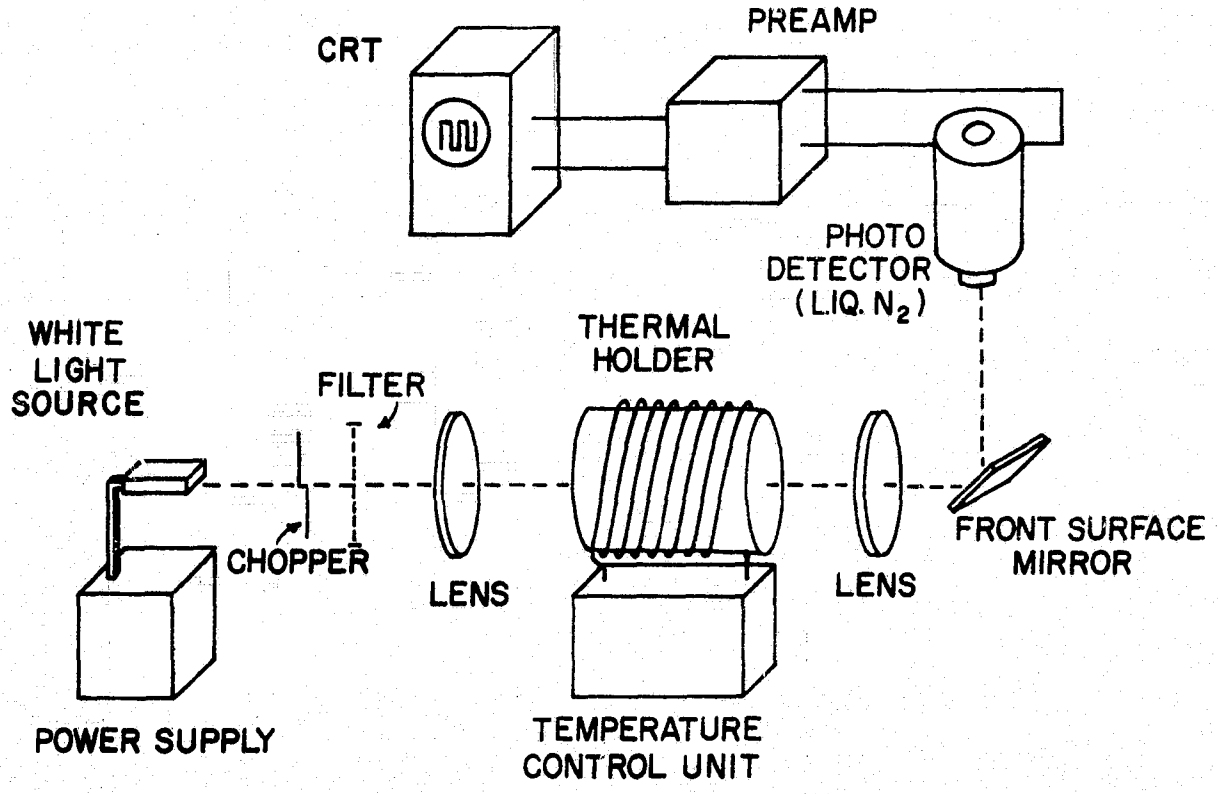


Figure 21. Optical system to calibrate silicon optical absorption coefficients versus silicon doping concentration and temperature.

Tungsten light was used as a source, the beam was chopped at a frequency of 80 cps and samples were held in the temperature controlled holder. The 2.0 μm filter used was manufactured by Optics Technology Inc., Flushing, N.Y., the wavelength tolerance of this filter, set 20 Infrared Narrow Band Filter, was ± 0.05 μm. The photovoltaic indium arsenide infrared detector, when cooled by liquid nitrogen to 196°K, had a peak detectivity D* of $3.7 \times 10^{10}$ cm-Hz$^{\frac{1}{2}}$/watt at 3.3 μm, the output impedance was 3000 Ω and a response time of 1 μsec. This system was checked by varying the intensity of the source from maximum to 5% of maximum and the oscilloscope does show a corresponding amplitude variation of the signal with errors below 6%.

Data were taken on sampling wafers of various doping concentrations and on temperature settings of 25°C to 250°C. Decrease of transmitted intensities versus temperature were measured and plotted on Figure 22, for the incident light of 1.15 μm.

From the relationship

$$I = I_0 \exp(-\alpha d) \qquad (137)$$

one may find α. $I_0$ and I are the intensity of light before and after passing through the sample of thickness d, and absorption coefficient α. The α's calculated are plotted on Figure 23.

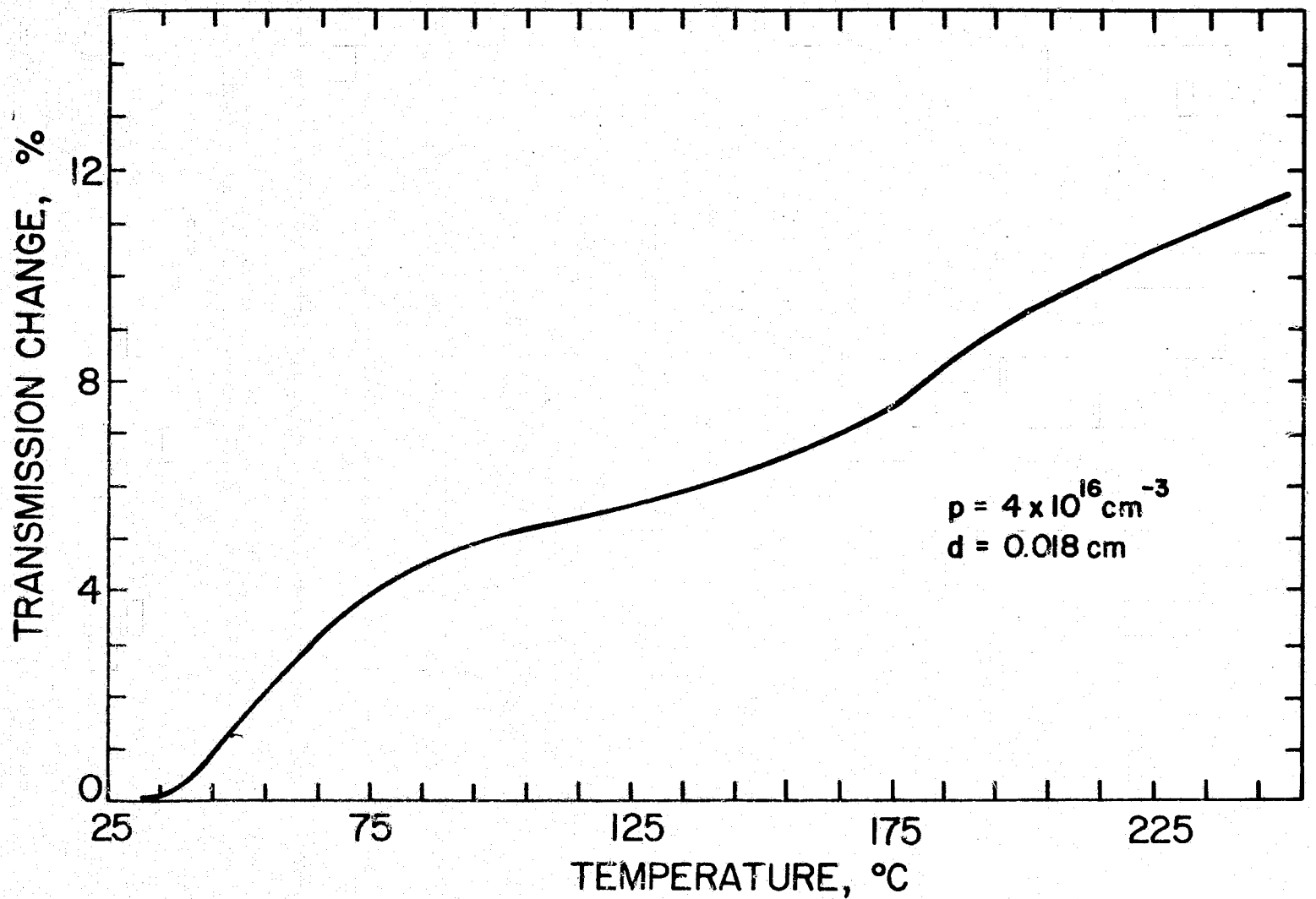


Figure 22A. Transmission change of infrared light ($\lambda$=1.15μm) as a function of temperature for silicon wafers.

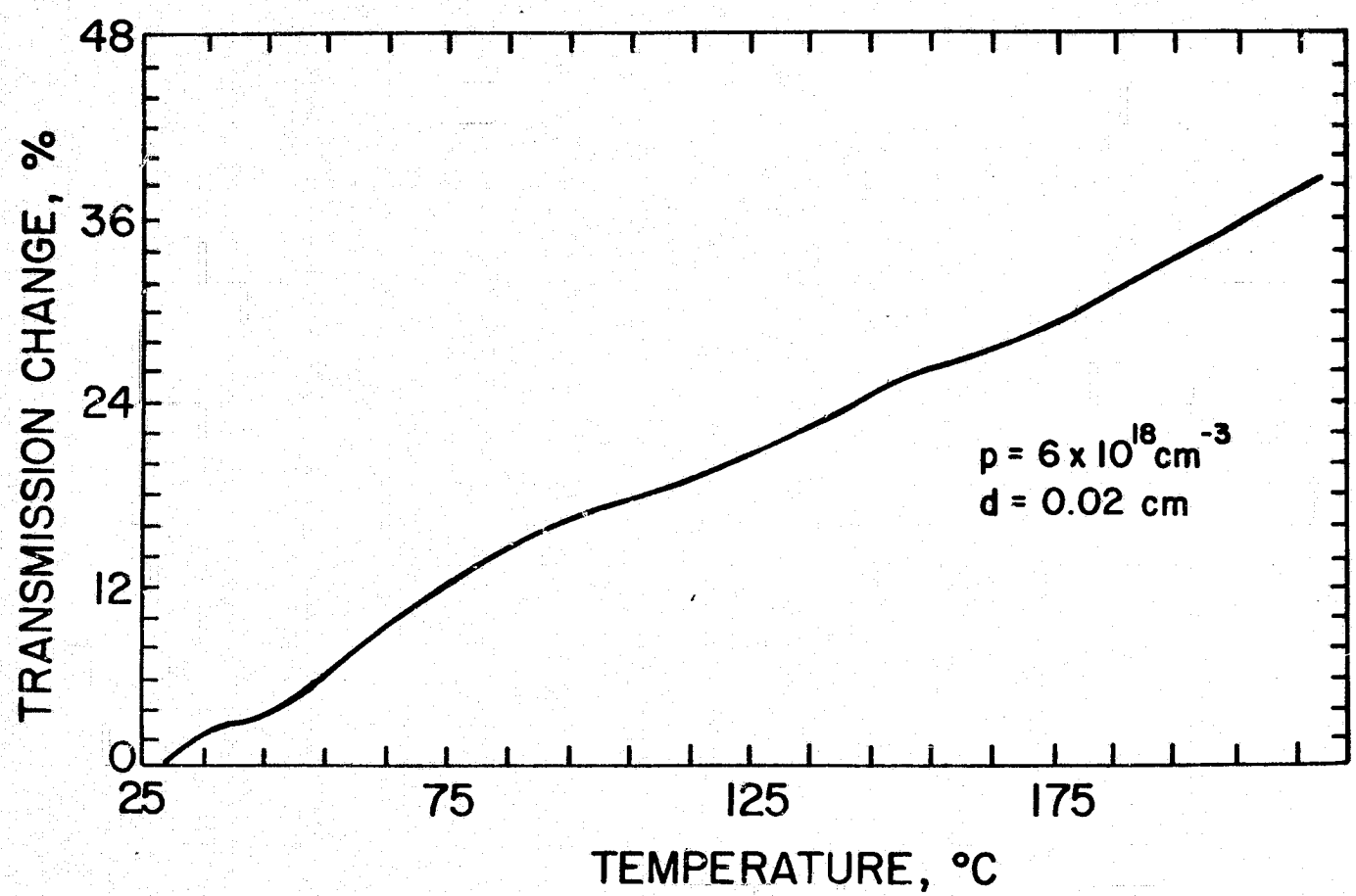


Figure 22B. Transmission change of infrared light ($\lambda$=1.15$\mu$m) as a function of temperature for silicon wafers.

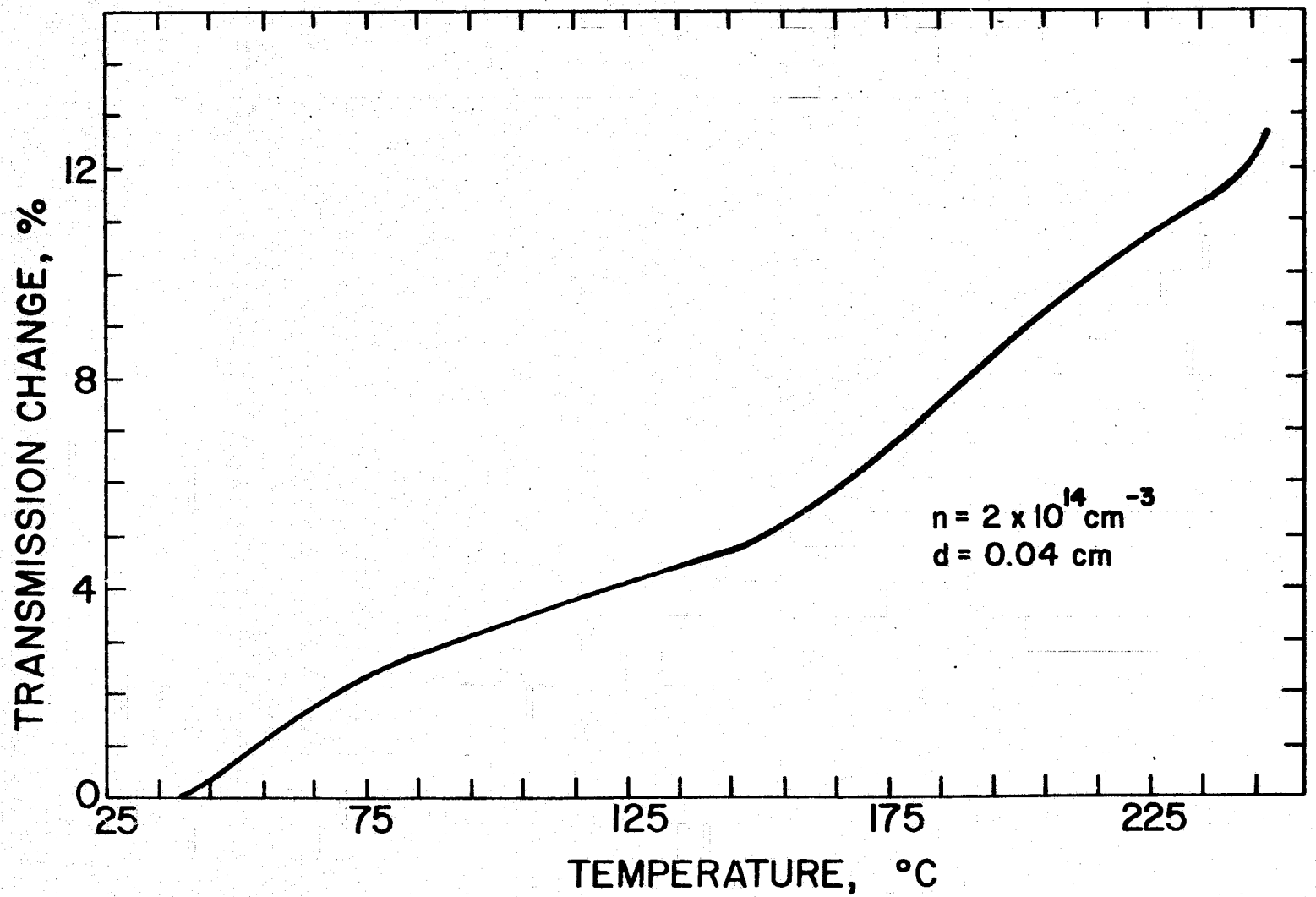


Figure 22C. Transmission change of infrared light ($\lambda$=1.15μm) as a function of temperature for silicon wafers.

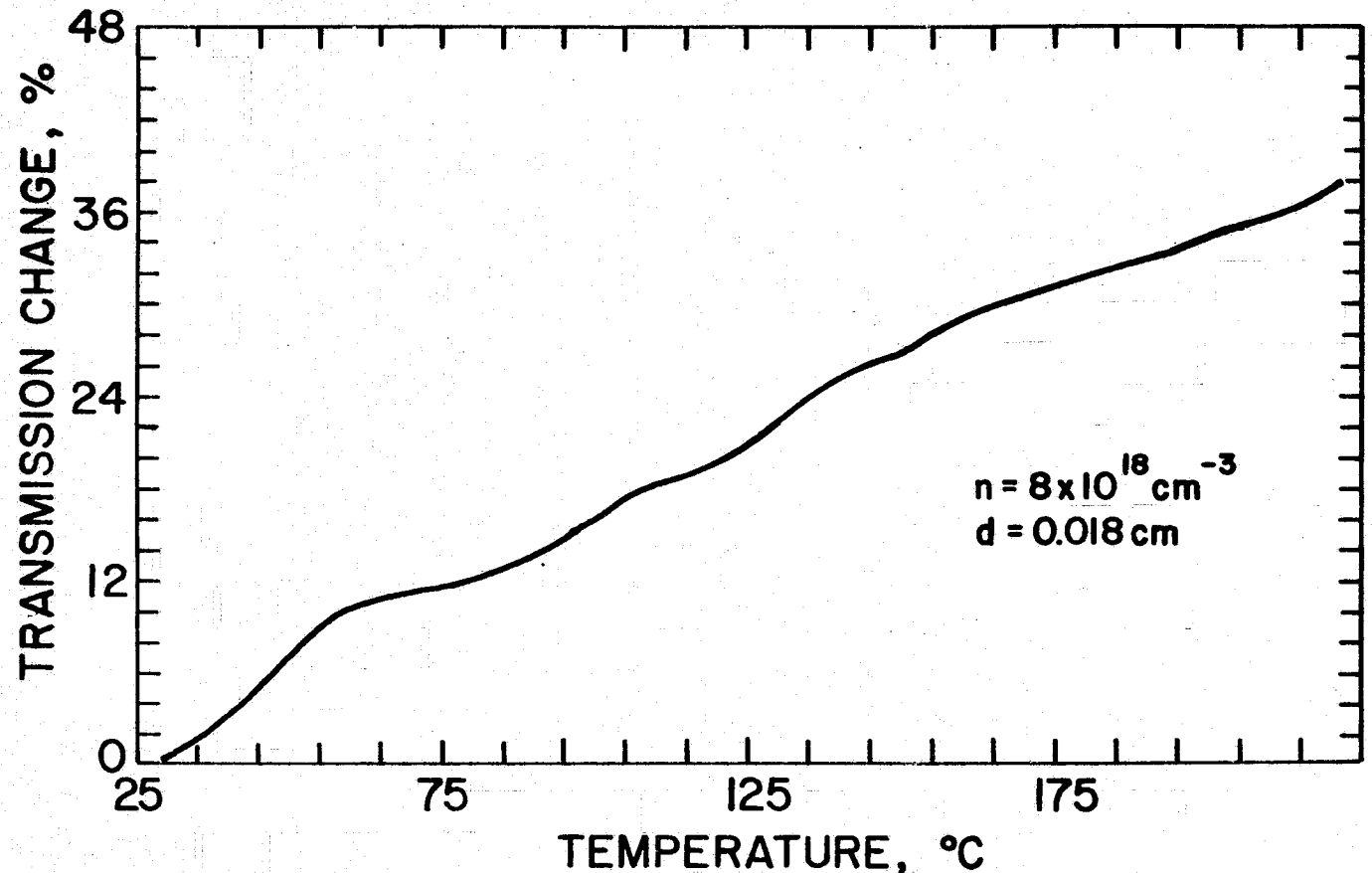


Figure 22D. Transmission change of infrared light ($\lambda$=1.15$\mu$m) as a function of temperature for silicon wafers.

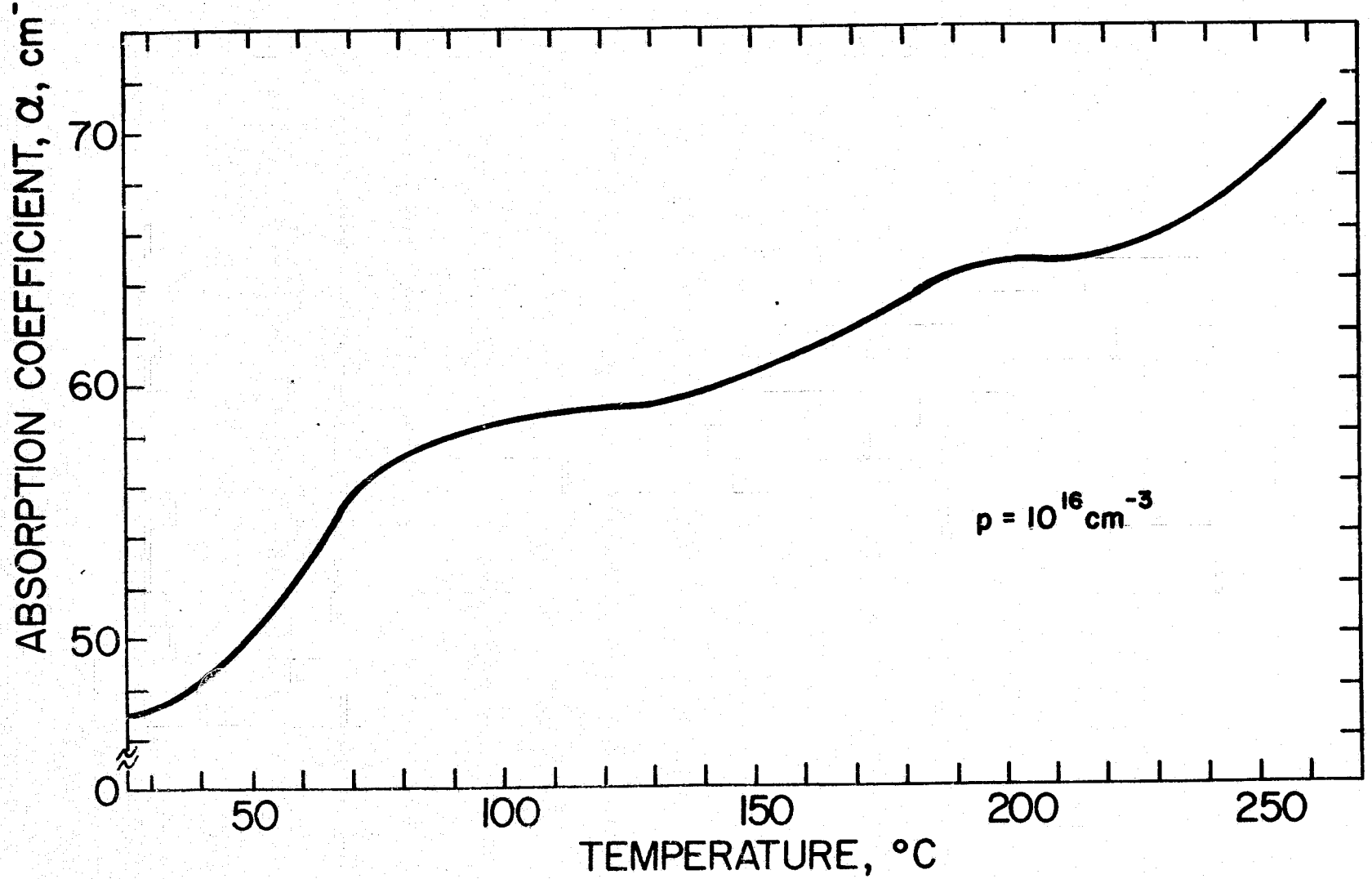


Figure 23A. Absorption coefficient change of infrared light (λ=1.15μm) as a function of temperature for silicon wafers.

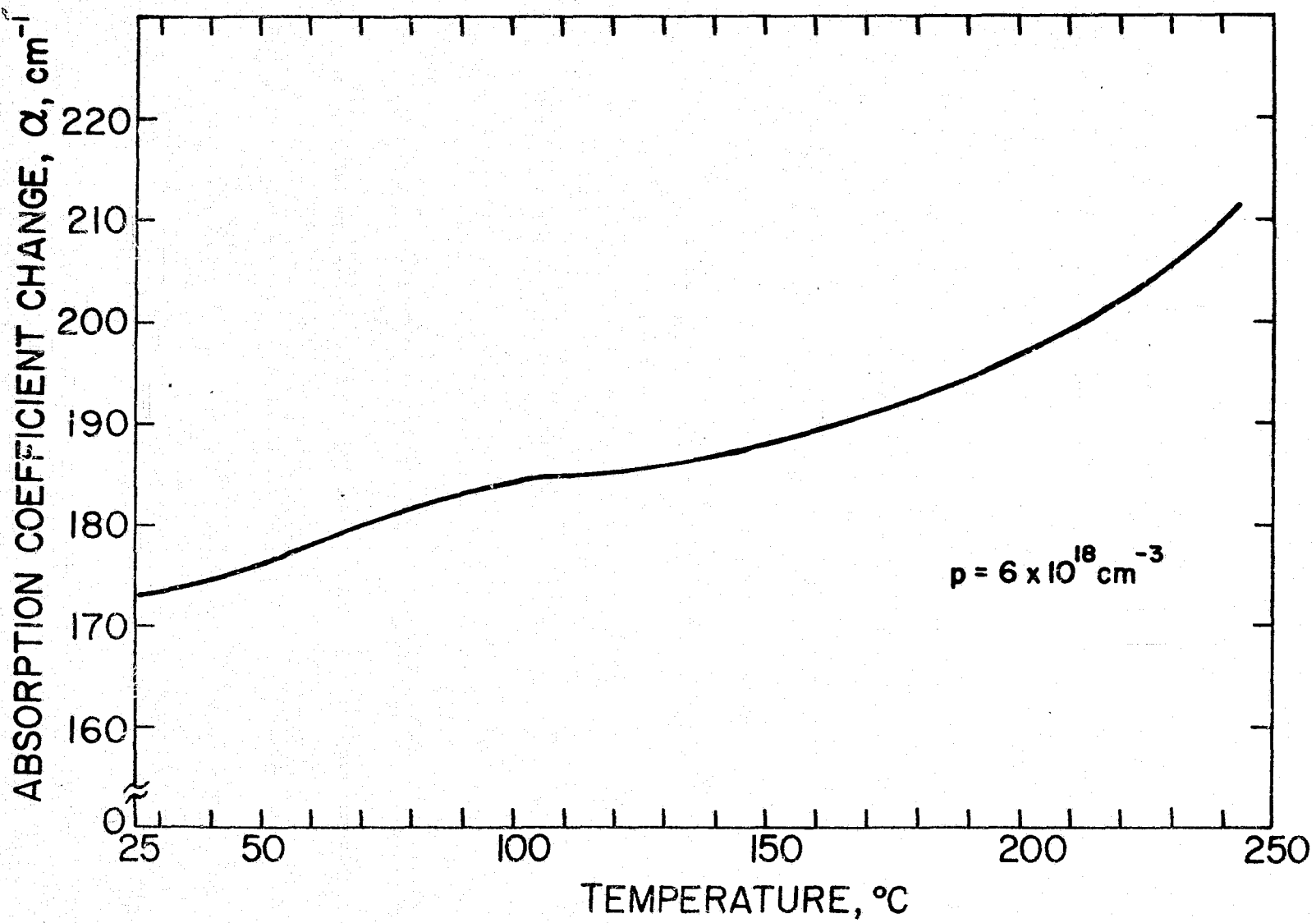


Figure 23B. Absorption coefficient change of infrared light ($\lambda$=1.15$\mu$m) as a function of temperature for silicon wafers.

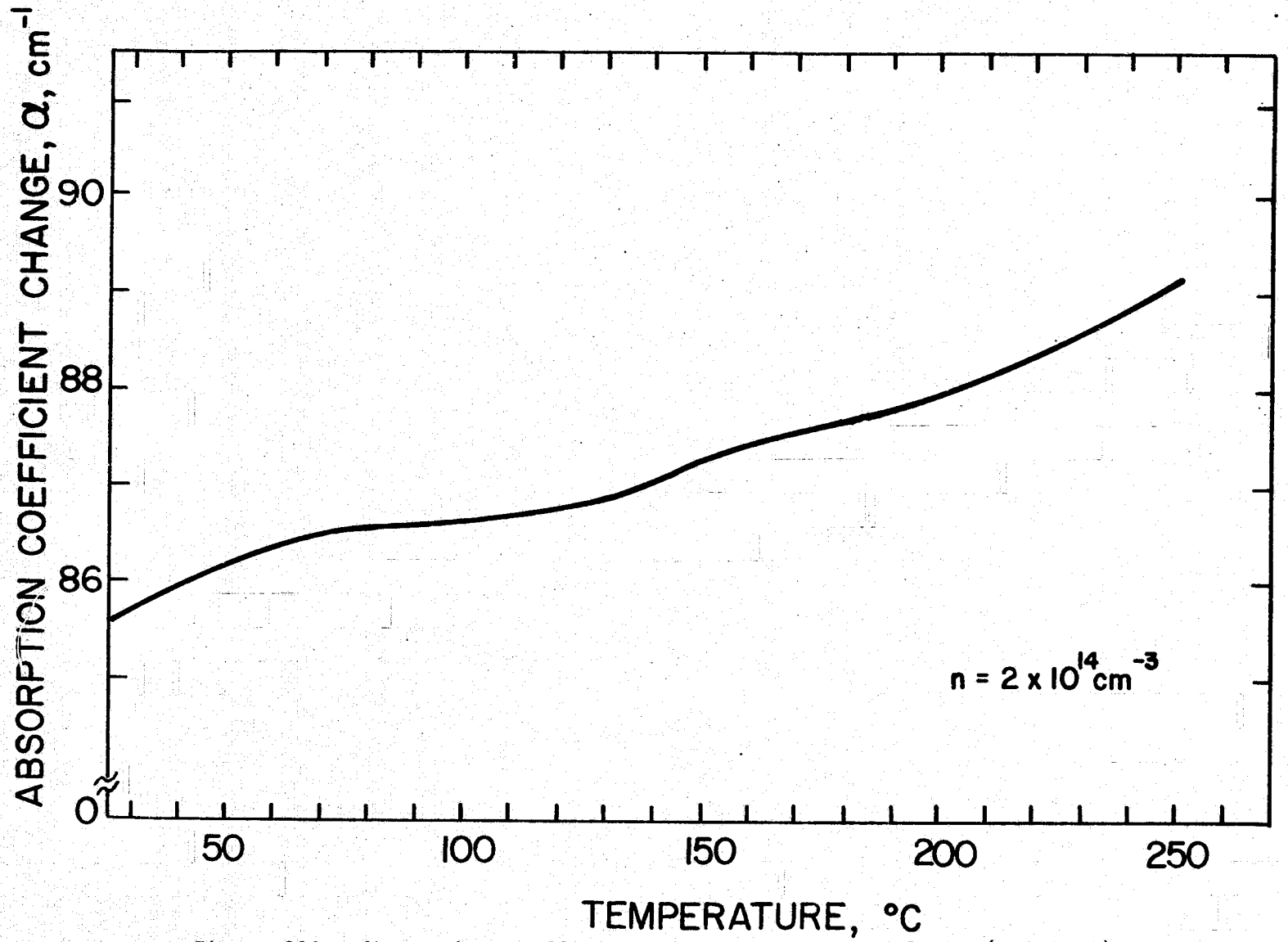


Figure 23C. Absorption coefficient change of infrared light ($\lambda$=1.15$\mu$m) as a function of temperature for silicon wafers.

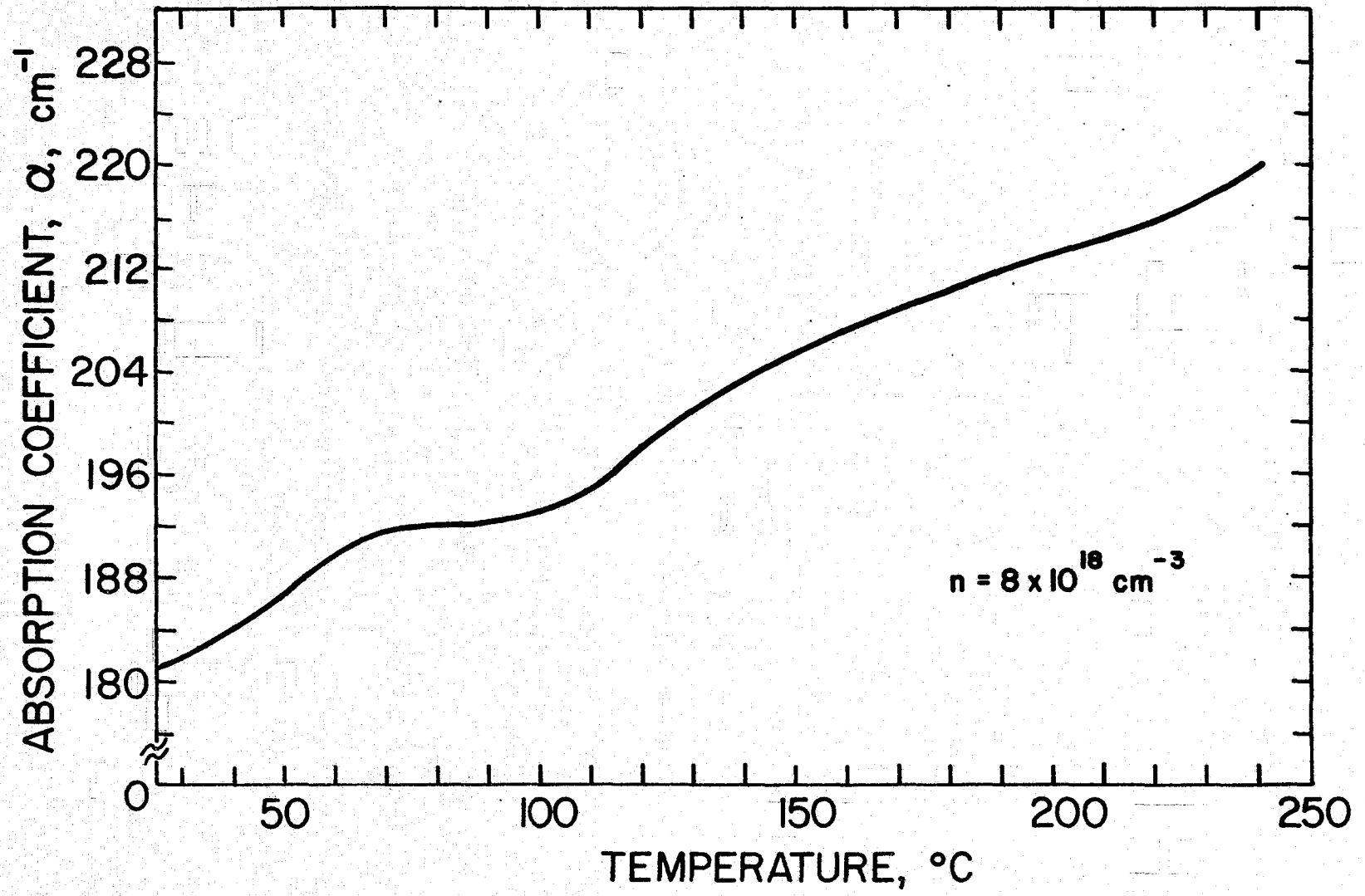


Figure 23D. Absorption coefficient change of infrared light ($\lambda$=1.15$\mu$m) as a function of temperature for silicon wafers.

In the same way, incident light of 2.0 μm, the intensity changes were measured and α's were calculated.

The characteristics of Figure 23 plotted for α's are: (1) The higher the doping concentrations, the larger the α's. (2) The higher the temperature, the higher the α's. These findings are consistent with the theories given earlier. In fact, these data are also consistent with the experimental data of references 45, 46, 19. By comparing the set of data of α's for λ=1.15 μm to the set of α's for λ=2.0 μm, it appears that α's measured by the light with a wavelength of 1.15 μm can resolve temperature better than α's measured at other infrared wavelengths. The optical absorption coefficient has the highest temperature sensitivity when the incident light has an energy value around the band gap energy of silicon.

The Mapping of Thermal Profiles

Using the data obtained in an earlier section, one may find the temperature of the wafer of known doping concentration and thickness from the $\alpha$ - T curves obtained. Therefore, by scanning light through a device and measuring absorption coefficients continually, one may draw the thermal profile of it. The problem involved with this experiment are: (1) The cross section area of thyristors are usually around $10^{-2}$ $cm^2$ or less, the incident beam spot diameter should be around 2.54 $\mu m$, so as to have enough number of discriminating measurements of absorption coefficients. (2) The device should not be covered with metal or thick oxide over these regions where light is transmitted. (3) The scanning of the device should be well arranged so as to enable each measured point to be identified. These problems are the major objectives in setting up the optical system as described below:

A. The Components of Optical Scanning System

Everything in the system should be solid, well-aligned and tightly leveled on an optical bench (see Figure 24): Each component is specified as follows:

(1) Light source: A He-Ne laser was used as light source, its cavity length is 43 cm and designed to emit light of 6328 $\mathring{A}$ in TEMoo mode with power of 2.0 mW. With confocal mirrors it emits light of wavelength 1.15 $\mu m$ with 0.3 mW power. Amplitude was found stable with

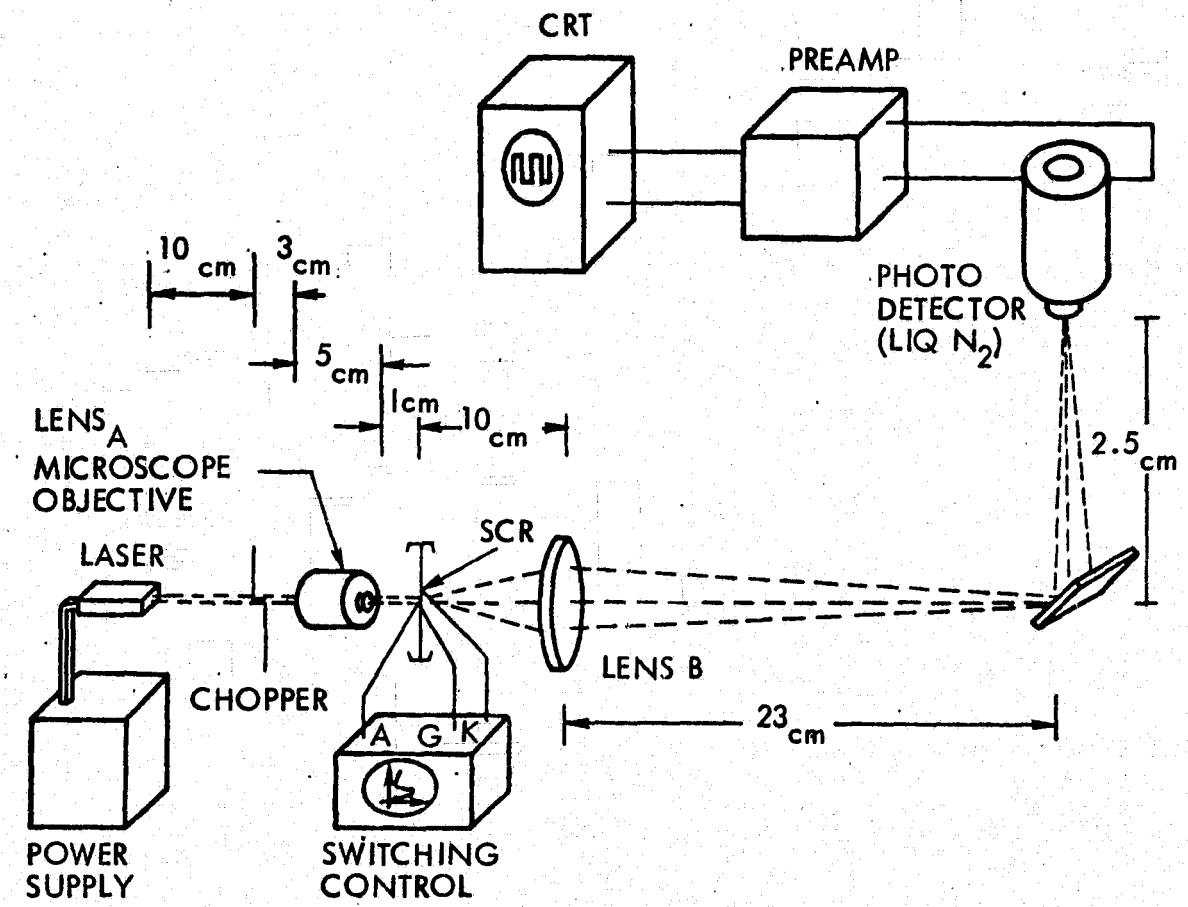


Figure 24 Optical System to Map the Thermal Profile Of a Switching Device

ripple within 1%, beam diameter is ($1/e^2$ point) 1.5 mm. and beam divergence is 1.5 mr, and linearly polarized.

(2) Chopper: It chops laser beam to square waves of frequency of 80 cps.

(3) Lens A: An epiplan 40/0.85 lens was used.

(4) Device holder: An optical bench holder with micrometers for adjusting the device location horizontally and vertically with a precision of $10^{-3}$ cm, was found adequate to localize the focused spot.

(5) Lens B: The focal length is 9 cm which refocuses the diverging beam on the photodetector after the beam is reflected by the front surface mirror.

(6) Photo detector: The same InAs photovotaic detector was used as was used previously.

B. Devices:

In order to verify experimentally the actual temperature profile within the junction, it is necessary to test typical commercially available thyristors. It is however very difficult to know the doping concentrations, junction depths, metalization layers, etc. of a commercial product. The set of measured figures one can obtain is that shown in Figure 25 (GE Series C30 which is corner-gated). When measuring along a-b line or c-d line of Figure 25-B, the activities along a-b line are too far away to influence the c-d line, and vice

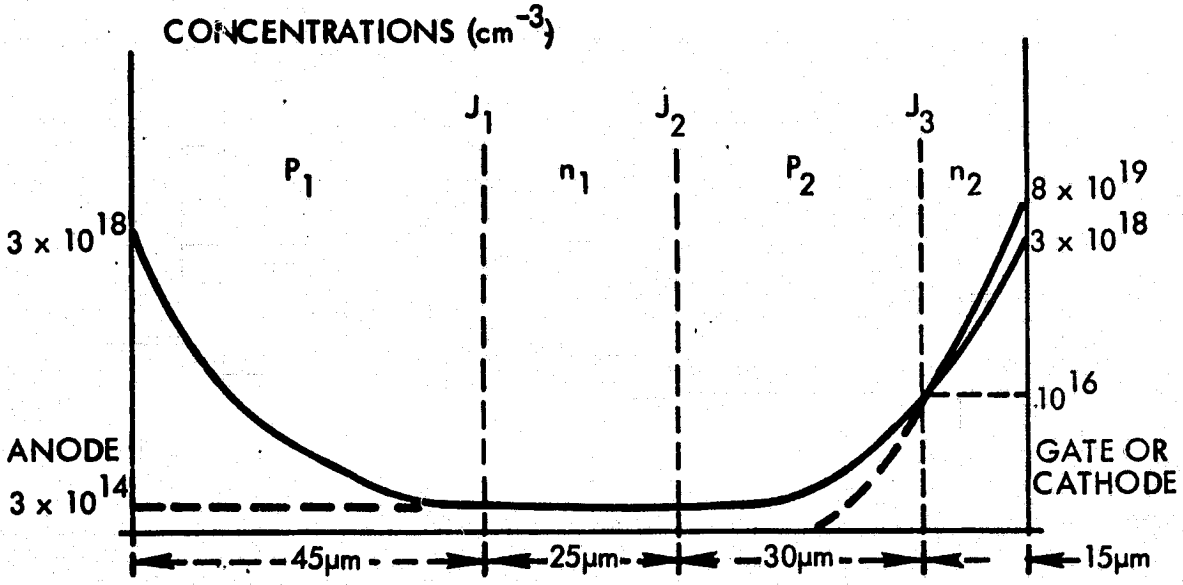


Figure 25-A Doping Profiles of Thyristor Sample

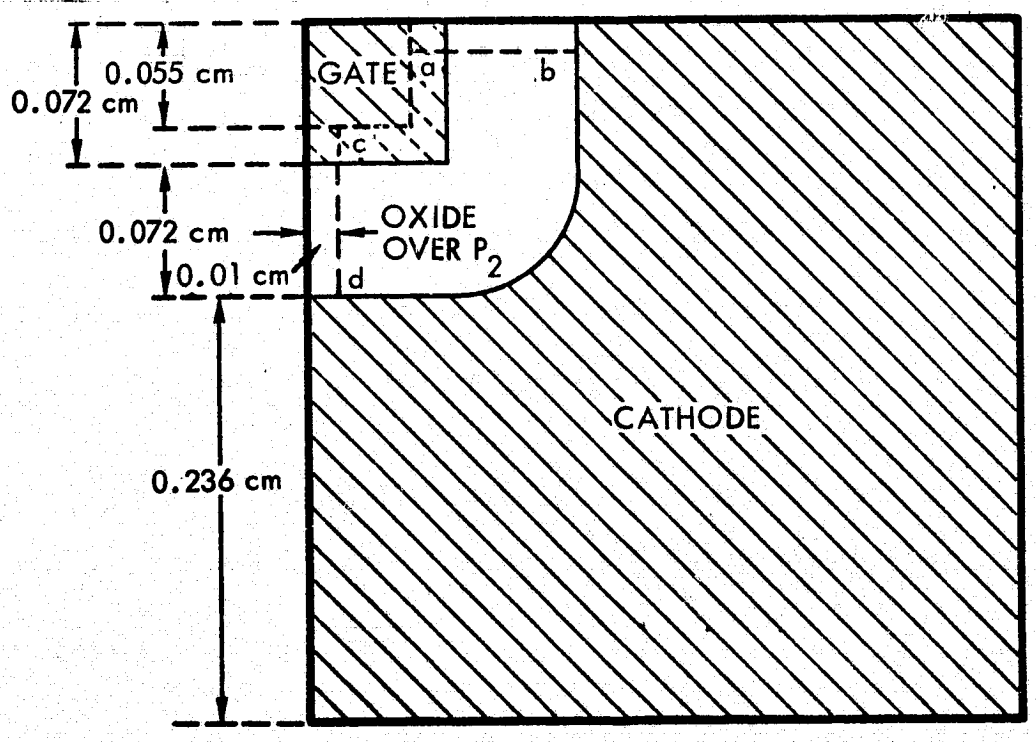


Figure 25-B Geometry of Gate-Cathode Metal Contacts of Thyristor under test. Solid-lined regions are the new contacts after modification. The anode on the other side is modified to the same solid-lined geometry also.

versa, so that the measurements of a corner-gated thyristor should have the same characteristic as an interdigitated thyristor. This Series C30 thyristor has a power switching capability of $10^4$ Watts, maximum forward blocking voltage of 400 volts, RMS forward current (on-state) 25 Amperes, gates power dissipation of 0.5 Watts (average), or 5.0 Watts (maximum). The metal contacts are made of three layers: chrome ($10^3$ Å), nickel (3 ~ $4x10^3$ Å), silver ($1.5x10^4$ Å). Since the metal contact on the anode is a complete 0.38 cm x 0.38 cm square, it blocks the infrared beam. This was solved by modifing the metal contacts of this device on a solid holder and attach leads to it is a very difficult task, because the device has no direct support and numerous attempts to bond wires with ultrasonic wire bonding were fruitless. An alternative approach was to take a piece of printed circuit board (2 inches in diameter) cut a hole in the middle and glue a chip of devices onto it. The copper surface of PC board was cut into three areas and spring contacts were attached to the anode, cathode and gate of the device from each area individually as shown in Figure 26. The modified devices were tested with a Tektronix Type 575 Curve Tracer and the I-V characteristics obtained are shown in Figure 27.

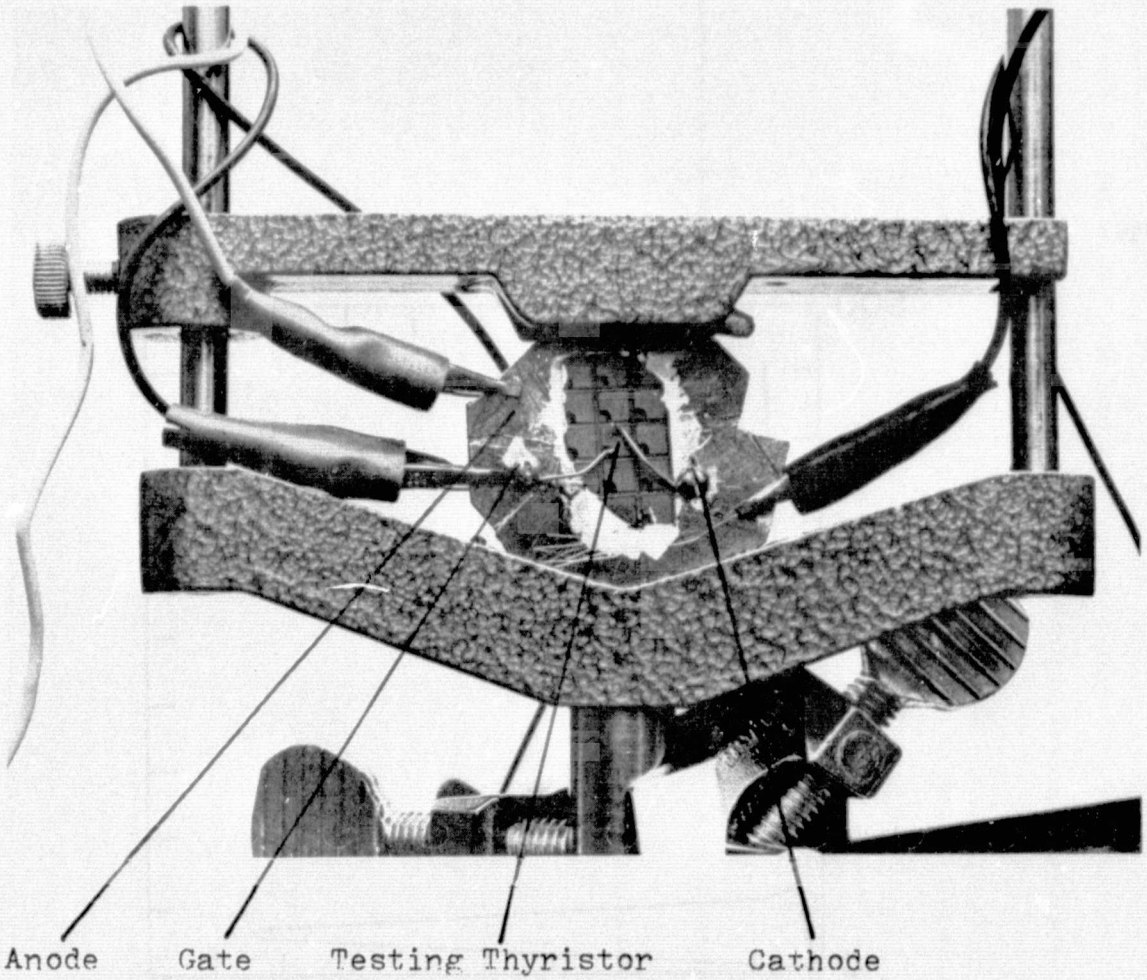


Figure 26 Testing Thyristor mounted on Printed Circuit Board

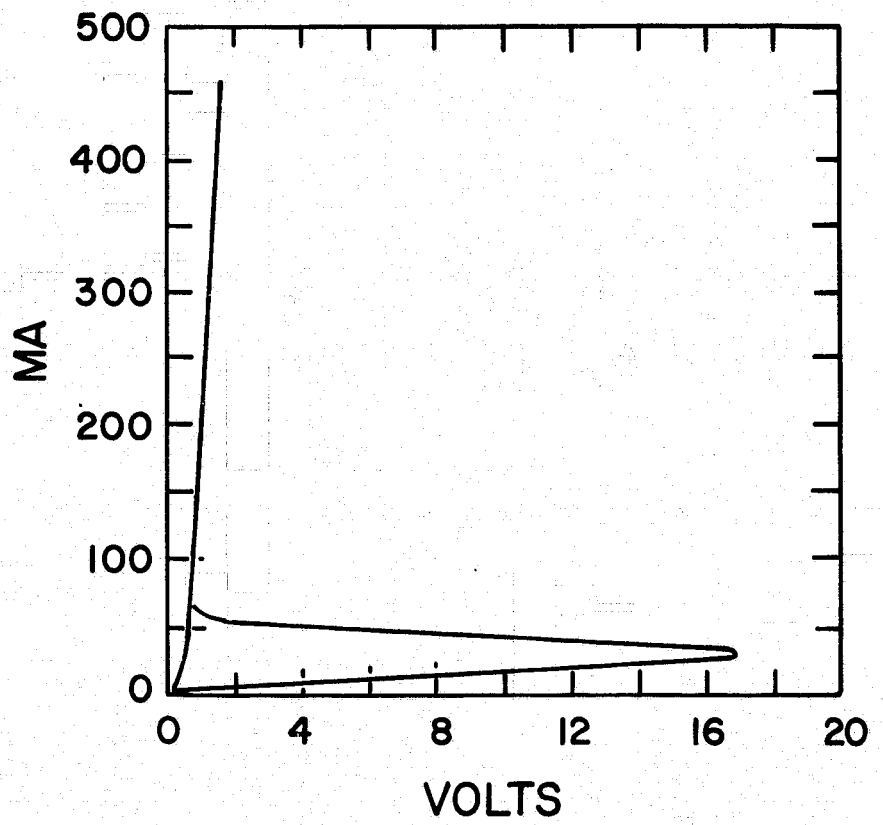


Figure 27. I-V characteristics of modified sample C30.

C. The Set-up and The Measurements

To set up a system as shown in Figure 24 with components specified in A. is fairly straight forward, but to make sure that the beam size is small enough, a pinhole was used in the optical path of this system. The pinhole chosen was 25 μm in diameter. The position of the pinhole is set to obtain a maximum intensity detected (the CRT reads 0.07 volts for peak to peak magnitude of the square waves, and when measured without the pinhole, the CRT reads 0.14 volts). The spot size focused by the microscope objective as described in IV A (3), was about 0.00375 cm in diameter.

A photograph of the actual experimental system is shown in Figure 28. The Curve Tracer monitored the device characteristics during measuring, and it provides switching drive at a frequency of 120 cps.

When measuring along the ab line or the cd line of each device, the thermal activities may be mapped between cathodes and gates. There are two kinds of thermal profiles to generate: (A) Thermal profile of the device in on-state, (static case). (B) Thermal profile of the device due to successive switching. Since the temperature change due to each switching is accumulated, this thermal profile may reveal the change due to each switching (dynamic case). Dynamic measurements were conducted first.

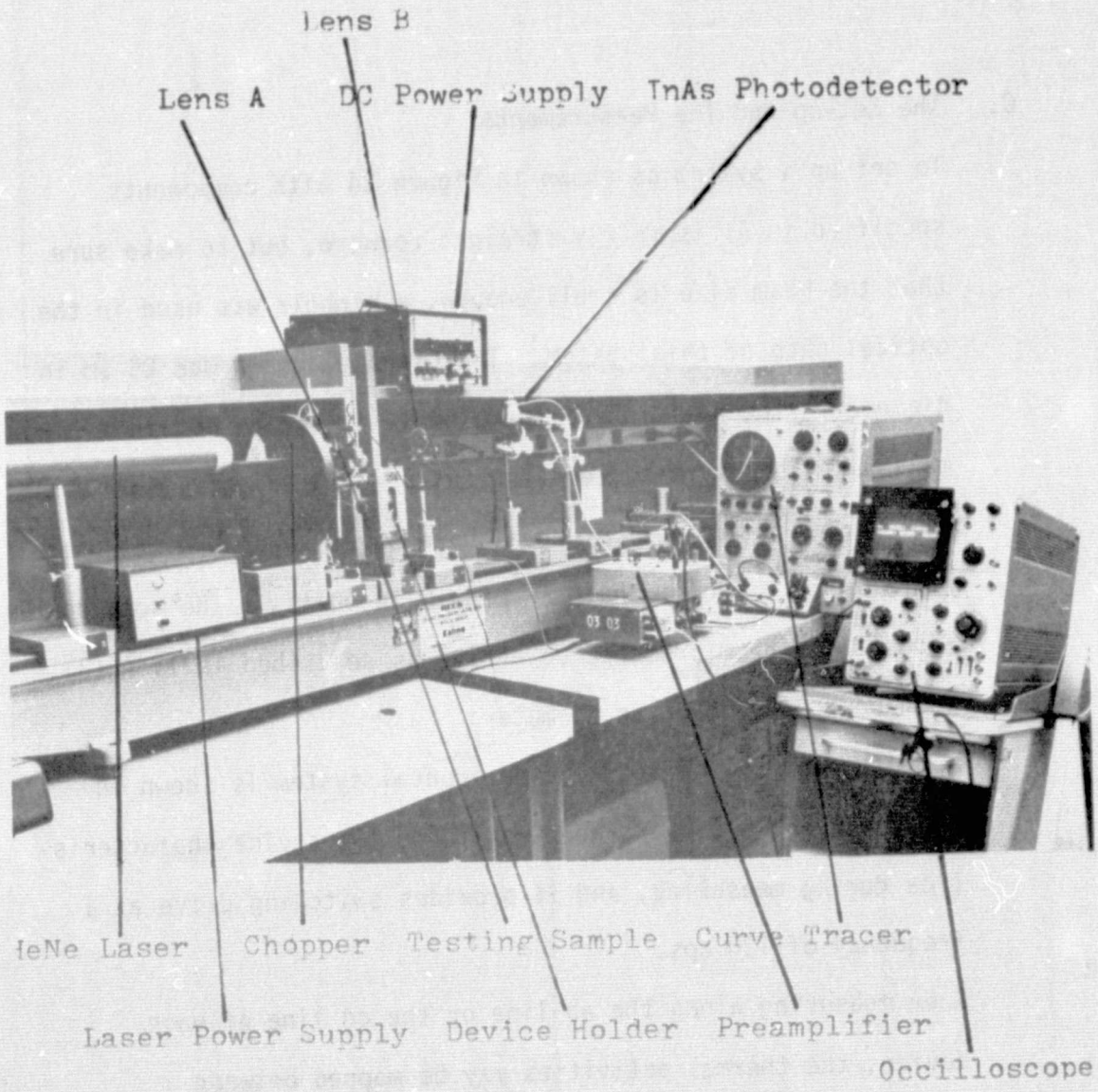


Figure 28 The Actual Experimental System

(A) Dynamic Measurement There are two ways of measuring:

(1) Scan the beam through the device (in fact, one moves the device, so that the fixed light may "scan" through the device) before the device is energized, and take several measurements of transmission during that time, then switch the device on and off a large number of times, scan the beam through again, and measure the transmission at the same spots as the first time. This should reveal the difference of transmission due to switching. But this approach needs to synchronize the system and be fast enough to avoid thermal runaway in the second measuring.

(2) Fix the beam at a spot on the device, measure before or after the switchings, then cool the device to room temperature and move to the next spot. Since it is difficult to take care of the thermal runaway in the first approach, the second approach was tried in this research. When doing the measurements, the scanning lines (i.e., ab or cd lines) were 0.01 cm away from the edges. The spots for measurements were not chosen equidistant. Between two measurements at each spot, the devices were switched on and off for five minutes (about $3.6 \times 10^4$ switchings). After the second measurement, the device was cooled down by an air blower until the intensity went back to that of the first measurement, this serving as a consistency check. The results of these measurements are tabulated in Table 1 through 5. Column "y" identifies

distances between measuring spots and the metal contact of the cathode. Column "$V_1$" is the intensity before switching and "$V_o$" is the intensity measured without the device. "$\alpha$" is the temporal absorption coefficient immediately after switchings, and "T" is the corresponding temperature.

(B) Static Measurement The set-up is the same as that shown in Figure 24, only the curve tracer is replaced by a DC power supply. The positive output of the power supply is connected to the anode of the device. It is also connected to the gate through a load register $R_G$. The negative output is connected to the cathode through another load resistor $R_C$. When the device is turned on for a moment, a non-uniform thermal distribution is generated. Here again the same two methods of measuring the thermal profile which were described for the dynamic measurements are available, and the second way was chosen. For these measurements, $R_G$ was chosen as 200 Ω, and $R_C$ was chosen as 10 Ω. The power supply was set to 8 volts, when in forward blocking state and the cathode current $I_k$ was around $5 \times 10^{-4}$ Amp. When triggered by gate pulse, the device was turned on, $I_k$ jumped to 0.125 Amp, and the device voltage drop $V_{AK}$ was 0.2 volts. Optical measurements were taken before switching and thirty (30) seconds after they have been switched on. Then the device was turned off by turning the power supply off.

| $y$(in $10^{-3}$ cm) | $V_1$(in Volts) | $V_1/V_o$(in %) | $V_2$(in Volts) | $V_2/V_o$(in %) | $\alpha$(in $cm^{-1}$) | T(in $^oC$) |
|---|---|---|---|---|---|---|
| 10 | 0.036 | 25.7 | 0.034 | 24.3 | 53 | 62 |
| 12.5 | 0.033 | 23.8 | 0.030 | 21.4 | 56.7 | 73 |
| 33.7 | 0.036 | 25.7 | 0.030 | 21.4 | 66.6 | 230 |
| 42.5 | 0.045 | 32.2 | 0.042 | 30.0 | 63 | 178 |
| 47.5 | 0.027 | 19.3 | 0.022 | 15.7 | 60.5 | 140 |
| 53.7 | 0.043 | 30.7 | 0.040 | 28.6 | 60.5 | 140 |
| 65 | 0.046 | 32.8 | 0.044 | 31.5 | 57 | 76 |
| 76.3 | 0.048 | 34.3 | 0.040 | 28.6 | 97.5 | * |
| 82.5 | 0.032 | 23.8 | 0.030 | 21.4 | 56.6 | 74 |

Table 1. Absorption Coefficients and Temperature Values after Thyristor was switched for $3.6 \times 10^4$ times. $V_o$ = 0.14 volts. Thyristor 1

| $y$(in $10^{-3}$ cm) | $V_1$(in Volts) | $V_1/V_o$(in %) | $V_2$(in Volts) | $V_2/V_o$(in %) | $\alpha$(in $cm^{-1}$) | T(in $^oC$) |
|---|---|---|---|---|---|---|
| 0 | 0.032 | 23.6 | 0.032 | 22.8 | 50 | 50 |
| 25 | 0.040 | 28.6 | 0.036 | 25.7 | 62.3 | 172 |
| 33.7 | 0.036 | 25.7 | 0.032 | 22.8 | 59.5 | 130 |
| 60 | 0.030 | 21.4 | 0.024 | 17.2 | 63.6 | 183 |
| 77.5 | 0.027 | 19.3 | 0.022 | 15.7 | 60.5 | 140 |
| 87.5 | 0.033 | 23.8 | 0.030 | 21.4 | 56.6 | 74 |

Table 2. Absorption Coefficients and Temperature Values after Thyristor was switched for $3.6 \times 10^4$ times. Vo = 0.14 volts. Thyristor 2

* $\alpha$ readings are off the range of $\alpha$-T relation calibrated.

| x(in $10^{-3}$ cm) | $V_1$(in Volts) | $V_1/V_o$(in %) | $V_2$(in Volts) | $V_2/V_o$(in %) | $\alpha$(in $cm^{-1}$) | T(in $^oC$) |
|---|---|---|---|---|---|---|
| 0 | 0.050 | 41.6 | 0.042 | 35 | 56.5 | 72 |
| 6.25 | 0.084 | 70 | 0.068 | 56.6 | 77 | 230 |
| 8.75 | 0.082 | 68.3 | 0.072 | 60 | 68 | 230 |
| 28.7 | 0.089 | 74.1 | 0.056 | 53.3 | 100 | 230 |
| 38.7 | 0.093 | 77.5 | 0.084 | 70 | 67 | 230 |
| 56 | 0.085 | 70.9 | 0.064 | 53.3 | 88 | * |
| 72.5 | 0.090 | 75 | 0.064 | 53.3 | 107 | * |
| 83.7 | 0.060 | 50 | 0.048 | 40 | 62.5 | 170 |
| 90 | 0.056 | 46.7 | 0.048 | 40 | 56.8 | 75 |

Table 3. Absorption Coefficients and Temperature Values after Thyristor was switched for $3.6 \times 10^4$ times. $V_o$ = 0.14 volts. Thyristor 3

| x(in $10^{-3}$ cm) | $V_1$(in Volts) | $V_1/V_o$(in %) | $V_2$(in Volts) | $V_2/V_o$(in %) | $\alpha$(in $cm^{-1}$) | T(in $^oC$) |
|---|---|---|---|---|---|---|
| 21.2 | 0.094 | 58.8 | 0.086 | 53.8 | 55.6 | 70 |
| 42.5 | 0.092 | 57.5 | 0.088 | 55 | 51 | 55 |
| 55 | 0.082 | 51.2 | 0.056 | 35 | 75 | * |
| 62.5 | 0.097 | 60.6 | 0.076 | 47.6 | 71.5 | * |
| 80 | 0.095 | 59.4 | 0.092 | 76.6 | 50.3 | 52 |
| 88.8 | 0.081 | 50.6 | 0.068 | 42.4 | 60 | 140 |

Table 4. Absorption Coefficients and Temperature Values after Thyristor was switched for $3.6 \times 10^4$ times. $V_o$ = 0.14 volts. Thyristor 4

| $y$ (in $10^{-3}$ cm) | $V_1$ (in Volts) | $V_1/V_o$ (in %) | $V_2$ (in Volts) | $V_2/V_o$ (in %) | $\alpha$ (in $cm^{-1}$) | T (in $^oC$) |
|---|---|---|---|---|---|---|
| 0 | 0.040 | 25 | 0.037 | 23.1 | 50.8 | 54 |
| 5 | 0.068 | 42.5 | 0.063 | 39.4 | 54 | 65 |
| 17.5 | 0.090 | 56.2 | 0.080 | 50 | 70.8 | 260 |
| 32.5 | 0.090 | 56.2 | 0.086 | 53.8 | 59 | 121 |
| 56.25 | 0.092 | 57.5 | 0.085 | 53.1 | 64.7 | 195 |
| 67.5 | 0.062 | 38.8 | 0.056 | 35 | 55 | 67 |
| 90 | 0.062 | 38.8 | 0.056 | 35 | 55 | 67 |

Table 5. Absorption Coefficients and Temperature Values after Thyristor was switched for $3.6 \times 10^4$ times. $V_o$ = 0.14 volts. Thyristor 5

The device was cooled and the beam shifted to another point thus preparing it for another measurement. The results of these measurements are tabulated in Table 6 through 10. The caluclated absorption coefficient and corresponding temperature T are also shown in these tables.

D. Data Analysis

(A) Dynamic Measurements From the data for each of the points on the device, the absorption coefficients at a given temperature can be calculated and interpreted. Following is a typical calculation: From Table 1, when $y = 42.5$, $V_o = 0.14$, $V_1 = 0.045$, $V_2 = 0.042$. From Figure 23A, $\alpha_o = 47\ cm^{-1}$ for $p = 10^{16} cm^{-3}$ at room temperature. Since the measurements were done on the gate contact region, the thickness of $p_2$ is 45 μm (instead of 30 μm for the typical $p_2$ region).

The transmission ratio is:

$$\frac{I}{I_o} = e^{-\alpha_o d} = e^{-47 \times 0.0045} = 0.81$$

But $V_1/V_o = 0.322$

Therefore the transmission ratio due to $p_1$ and $n_1$ is

$$\frac{0.322}{0.81} = 0.395$$

After switching on and off for five minutes, $V_2$ is obtained, and $V_2/V_o = 0.300$. the actual transmission ratio

| y(in $10^{-3}$ cm) | $V_1$(in Volts) | $V_1/V_o$(in %) | $V_2$(in Volts) | $V_2/V_o$(in %) | $\alpha$(in $cm^{-1}$) | T(in $^oC$) |
|---|---|---|---|---|---|---|
| 24 | 0.036 | 0.0124 | 0.031 | 0.0117 | 48 | 36 |
| 34.5 | 0.080 | 0.276 | 0.075 | 0.0258 | 53.2 | 62 |
| 39 | 0.140 | 0.0482 | 0.130 | 0.0448 | 49.2 | 45 |
| 43.5 | 0.100 | 0.0345 | 0.075 | 0.0258 | 54.5 | 65 |
| 51 | 0.100 | 0.0345 | 0.900 | 0.0311 | 49 | 43 |
| 63 | 0.170 | 0.0585 | 0.130 | 0.0448 | 55.4 | 69 |
| 75 | 0.180 | 0.0620 | 0.160 | 0.0550 | 52.5 | 59 |
| 78 | 0.410 | 0.1410 | 0.380 | 0.1310 | 63 | 178 |
| 84 | 0.140 | 0.0482 | 0.120 | 0.0413 | 52.5 | 59 |
| 90 | 0.030 | 0.0103 | 0.026 | 0.00896 | 49.5 | 46 |

Table 6 Absorption Coefficients and Temperature Values obtained after Thyristor was turned on at Current 0.125 Amp. for 30 sec. $V_o$=3.0 volts. Thyristor 1

| y(in $10^{-3}$ cm) | $V_1$(in Volts) | $V_1/V_o$(in %) | $V_2$(in Volts) | $V_2/V_o$(in %) | $\alpha$(in $cm^{-1}$) | T(in $^oC$) |
|---|---|---|---|---|---|---|
| 1[illegible] | 0.050 | 0.3250 | 0.046 | 0.0288 | 50.5 | 51 |
| 33 | 0.060 | 0.0375 | 0.055 | 0.0344 | 49.2 | 49 |
| 39 | 0.080 | 0.0500 | 0.060 | 0.0375 | 76 | * |
| 45 | 0.150 | 0.0935 | 0.110 | 0.0688 | 70.5 | 260 |
| 48 | 0.140 | 0.0875 | 0.100 | 0.0625 | 70 | 260 |
| 60 | 0.106 | 0.0663 | 0.090 | 0.0563 | 55 | 68 |
| 66 | 0.210 | 0.1210 | 0.170 | 0.1062 | 81.5 | * |
| 78 | 0.120 | 0.0750 | 0.110 | 0.0688 | 54 | 64 |
| 84 | 0.120 | 0.0750 | 0.110 | 0.0688 | 54 | 64 |
| 87 | 0.165 | 0.1030 | 0.115 | 0.0719 | 79 | * |
| 90 | 0.052 | 0.0325 | 0.046 | 0.0288 | 50.5 | 51.5 |

Table 7 Absorption Coefficients and Temperature Values obtained after Thyristor was turned on at Current 0.125 Amp. for 30 sec. $V_o$=3.0 volts. Thyristor 2

* $\alpha$ readings are off the range of $\alpha$-T relation calibrated.

| y (in $10^{-3}$ cm) | $V_1$ (in Volts) | $V_1/V_o$ (in %) | $V_2$ (in Volts) | $V_2/V_o$ (in %) | $\alpha$ (in $cm^{-1}$) | T (in $^oC$) |
|---|---|---|---|---|---|---|
| 0 | 0.110 | 0.0380 | 0.095 | 0.0347 | 49.7 | 46 |
| 6 | 0.140 | 0.0480 | 0.125 | 0.0430 | 51.5 | 56 |
| 30 | 0.190 | 0.0655 | 0.165 | 0.0568 | 54 | 64 |
| 36 | 0.230 | 0.0792 | 0.210 | 0.0724 | 52.2 | 59 |
| 42 | 0.190 | 0.0655 | 0.165 | 0.0569 | 54 | 64 |
| 51 | 0.150 | 0.0517 | 0.080 | 0.0276 | 70.8 | 263 |
| 66 | 0.340 | 0.1170 | 0.280 | 0.0965 | 69.8 | 259 |
| 72 | 0.230 | 0.0792 | 0.160 | 0.0551 | 68.5 | 252 |
| 84 | 0.205 | 0.0705 | 0.120 | 0.0413 | 74.5 | * |
| 90 | 0.115 | 0.0396 | 0.050 | 0.0173 | 71.8 | 265 |

Table 8 Absorption Coefficients and Temperature Values obtained after Thyristor was turned on at Current 0.125 Amp. for 30 sec. $V_o$=3.0 volts. Thyristor 3

| y (in $10^{-3}$ cm) | $V_1$ (in Volts) | $V_1/V_o$ (in %) | $V_2$ (in Volts) | $V_2/V_o$ (in %) | $\alpha$ (in $cm^{-1}$) | T (in $^oC$) |
|---|---|---|---|---|---|---|
| 9 | 0.120 | 0.0413 | 0.110 | 0.0380 | 50 | 49 |
| 24 | 0.170 | 0.0585 | 0.165 | 0.0569 | 48 | 36 |
| 30 | 0.260 | 0.0896 | 0.250 | 0.0862 | 50 | 49 |
| 39 | 0.220 | 0.0758 | 0.190 | 0.0655 | 55.2 | 68 |
| 51 | 0.180 | 0.0620 | 0.170 | 0.0585 | 50 | 49 |
| 63 | 0.107 | 0.0585 | 0.160 | 0.0550 | 49.5 | 46 |
| 75 | 0.420 | 0.1450 | 0.410 | 0.1410 | 54.5 | 66 |
| 78 | 0.125 | 0.0430 | 0.095 | 0.0328 | 56.5 | 75 |
| 90 | 0.044 | 0.0152 | 0.042 | 0.0145 | 48 | 36 |

Table 9 Absorption Coefficients and Temperature Values obtained after Thyristor was turned on at Current 0.125 Amp. for 30 sec. $V_o$=3.0 volts. Thyristor 4

| y(in $10^{-3}$ cm) | $V_1$(in Volts) | $V_1/V_o$(in %) | $V_2$(in Volts) | $V_2/V_o$(in %) | $\alpha$ (in $cm^{-1}$) | T(in $^oC$) |
|---|---|---|---|---|---|---|
| 10 | 0.110 | 0.0380 | 0.095 | 0.0347 | 49.7 | 46 |
| 17 | 0.010 | 0.0033 | 0.008 | 0.0026 | 50 | 49 |
| 22 | 0.022 | 0.0073 | 0.016 | 0.0053 | 51.7 | 50 |
| 28 | 0.029 | 0.0096 | 0.021 | 0.0070 | 52.2 | 51 |
| 38 | 0.115 | 0.0296 | 0.050 | 0.0173 | 71.8 | 265 |
| 45 | 0.170 | 0.0585 | 0.125 | 0.043 | 60 | 144 |
| 58 | 0.340 | 0.1170 | 0.280 | 0.0965 | 69.8 | 259 |
| 70 | 0.017 | 0.0585 | 0.165 | 0.0569 | 48 | 36 |
| 82 | 0.340 | 0.1170 | 0.275 | 0.0965 | 69.5 | 258.5 |
| 88 | 0.041 | 0.1410 | 0.380 | 0.1310 | 62 | 179 |

Table 10 Absorption Coefficients and Temperature Values obtained after Thyristor was turned on at Current 0.125 Amp. for 30 sec. $V_o$=3.0 volts. Thyristor 5

due to $p_2$, when considering 39.5% of transmission is due to $p_1$-$n_1$ regions, is

$$\frac{0.300}{0.395} = 0.76$$

This 76% is due to the new $\alpha$ and the same d(45 $\mu$m) of $p_2$-region, i.e.

$$e^{-\alpha d} = e^{-0.0045\alpha} = 0.76$$

$$\therefore \alpha = 60.5 \text{ cm}^{-1}$$

From Figure 23A, one finds that the corresponding temperature is 178°C.

The same calculations go on to complete columns of $V_1/V_o$, $V_2/V_o$, $\alpha$, T of Tables 1 to 5. The average values of $\alpha$ and T were plotted in Figures 29 and 30.

Note, (1) The transmission factor 0.395 due to $p_1$ and $n_1$ is consistent with the data measured. From Figures 23B, for $p_1$-region, $\alpha$ = 172 $\text{cm}^{-1}$ at room temperature and $\alpha$ = 85.6 $\text{cm}^{-1}$ for $n_1$-region at room temperature (Figure 23C). From the thickness of $p_1$-$n_1$ given in Figure 25-A, the transmission is

$$e^{-172 \times 0.045} \times e^{-85.6 \times 0.0025} = 0.389$$

which is only -1.5% off 0.395. (2) From Figures 23B and 23C, it is apparent that the $p_1$ and $n_1$ regions are much less temperature sensitive than the $p_2$-regions. Suppose, after

many switchings, there is a hot spot of 240°C in $p_2$, the neighboring point in $n_1$ is at 160°C, and $p_1$ is at 80°C, the transmission is:

$$e^{-182x0.045} \times e^{-87.2x0.0025} = 0.386$$

which is only -0.8% off 0.389. However, the transmission ratio in $p_2$ goes from

$$e^{-47x0.0045} = 0.81$$

to

$$e^{-67x0.0045} = 0.74$$

which is -8.65% off 0.81. Noting the difference of thermal conductivity of each region as is mentioned earlier, it follows that the thermal profiles obtained in Figures 29 and 30 are mainly generated by the $p_2$ region.

(B) Static Measurements The analysis is essentially the same as that shown for Dynamic Measurements, the values of $\alpha$ and T are calculated and tabulated in Table 6 through 10. The average values of $\alpha$ and T of these five measurements are plotted in Figures 31 and 32.

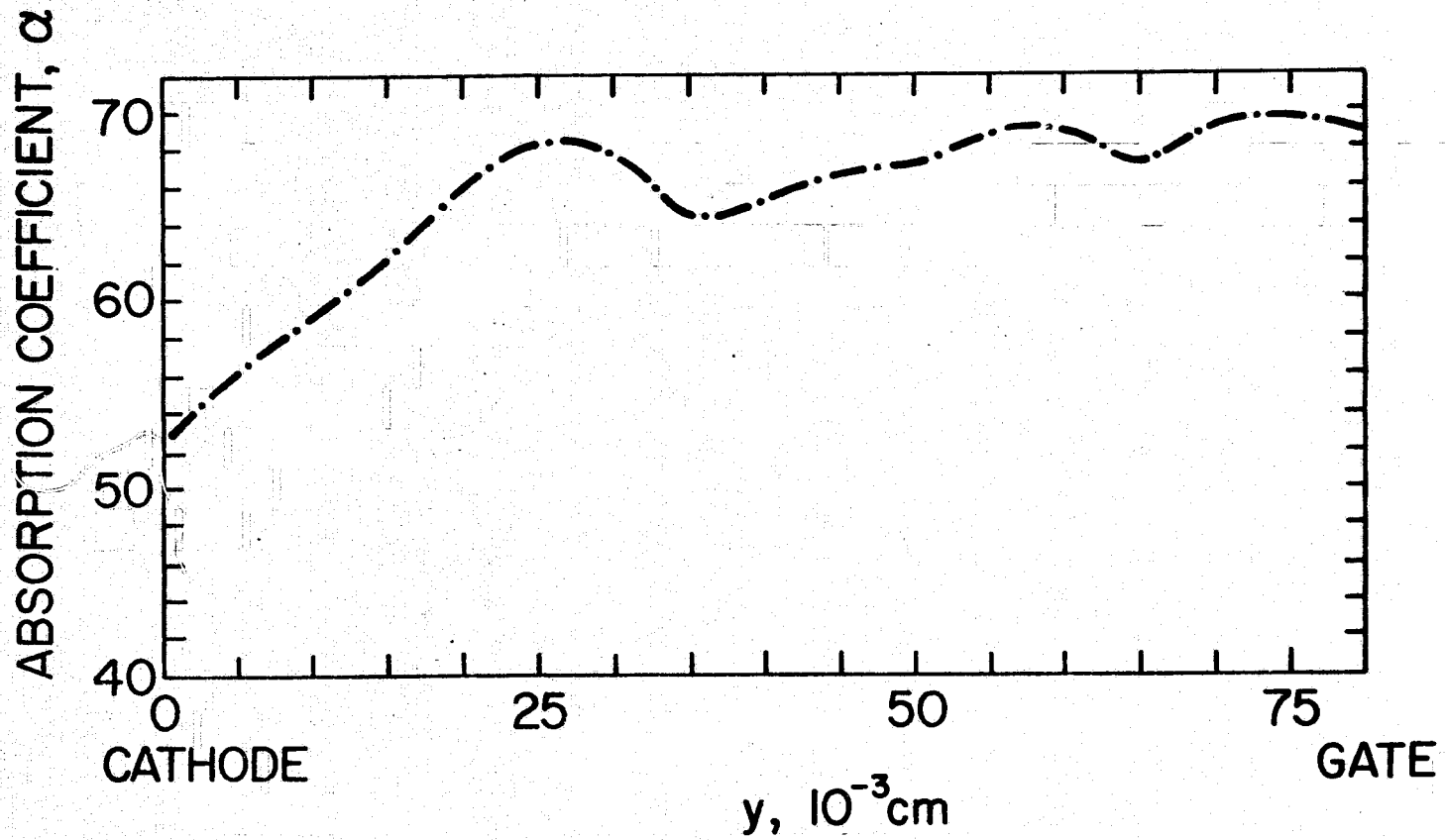


Figure 29. Variation of the absorption coefficient value between cathodes and gates (Dynamic Case).

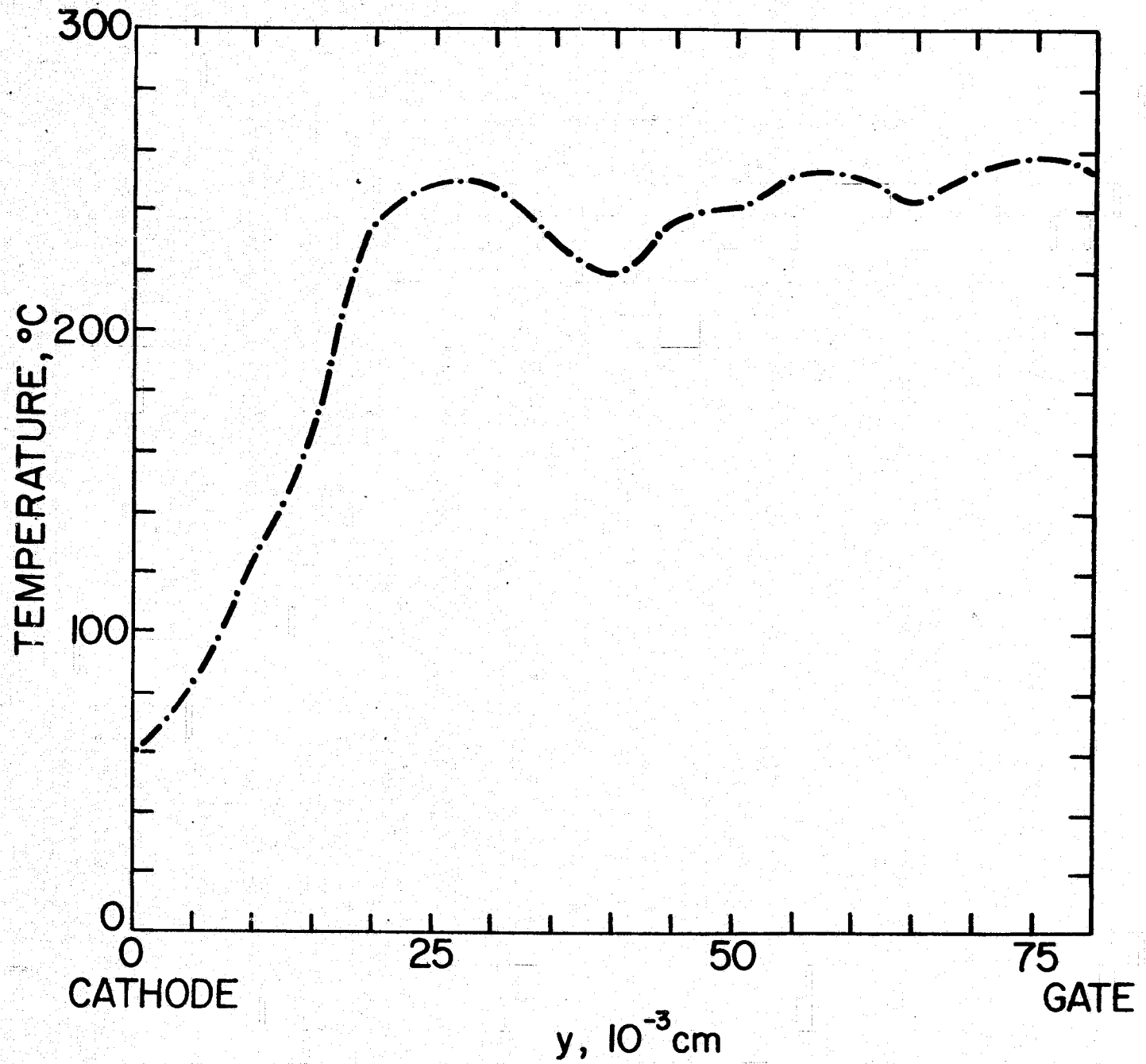


Figure 30. Variation of the temperature value between cathodes and gates. (Dynamic Case).

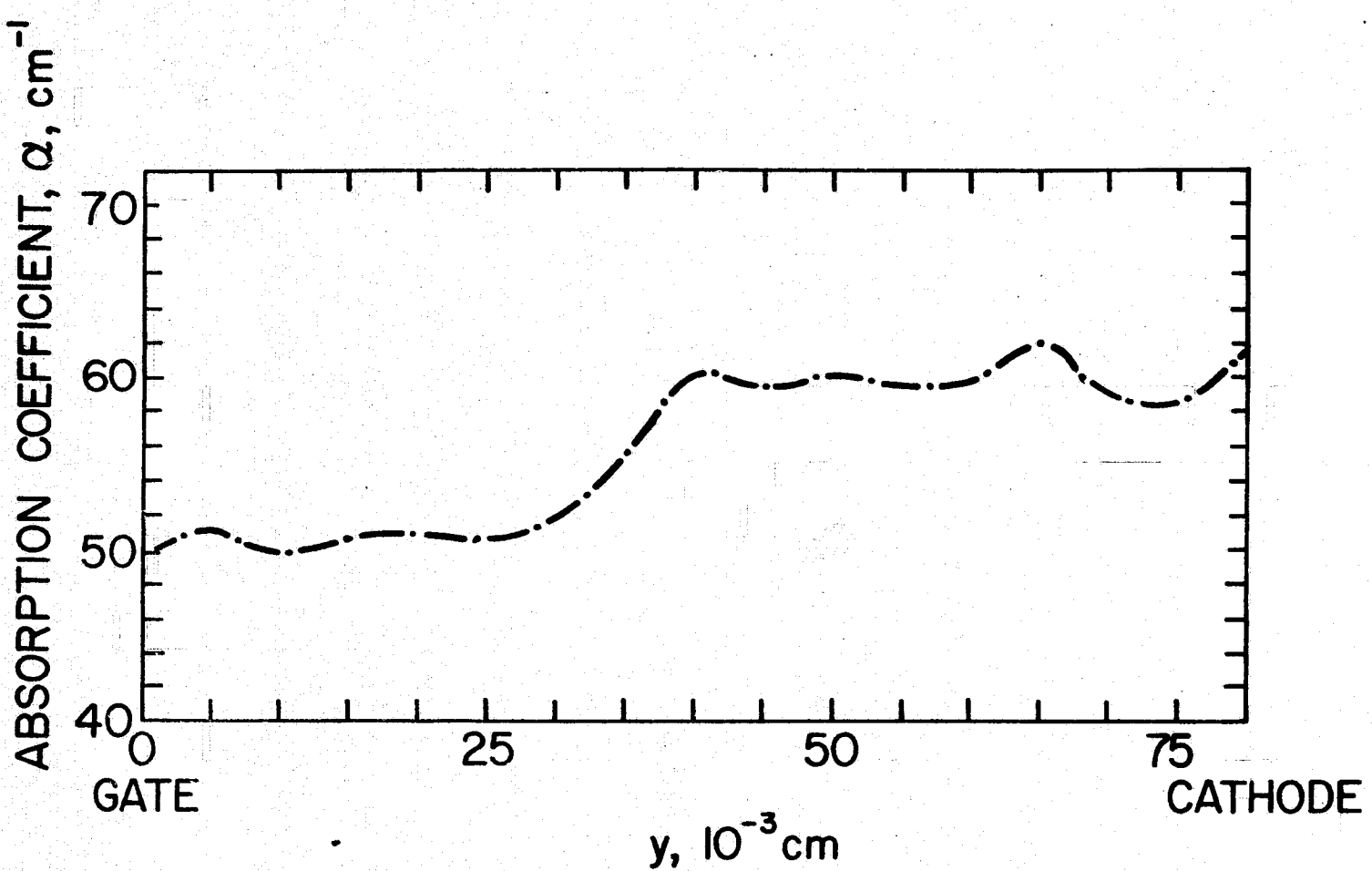


Figure 31. Variation of the absorption coefficient value between gates and cathodes. (Static Case).

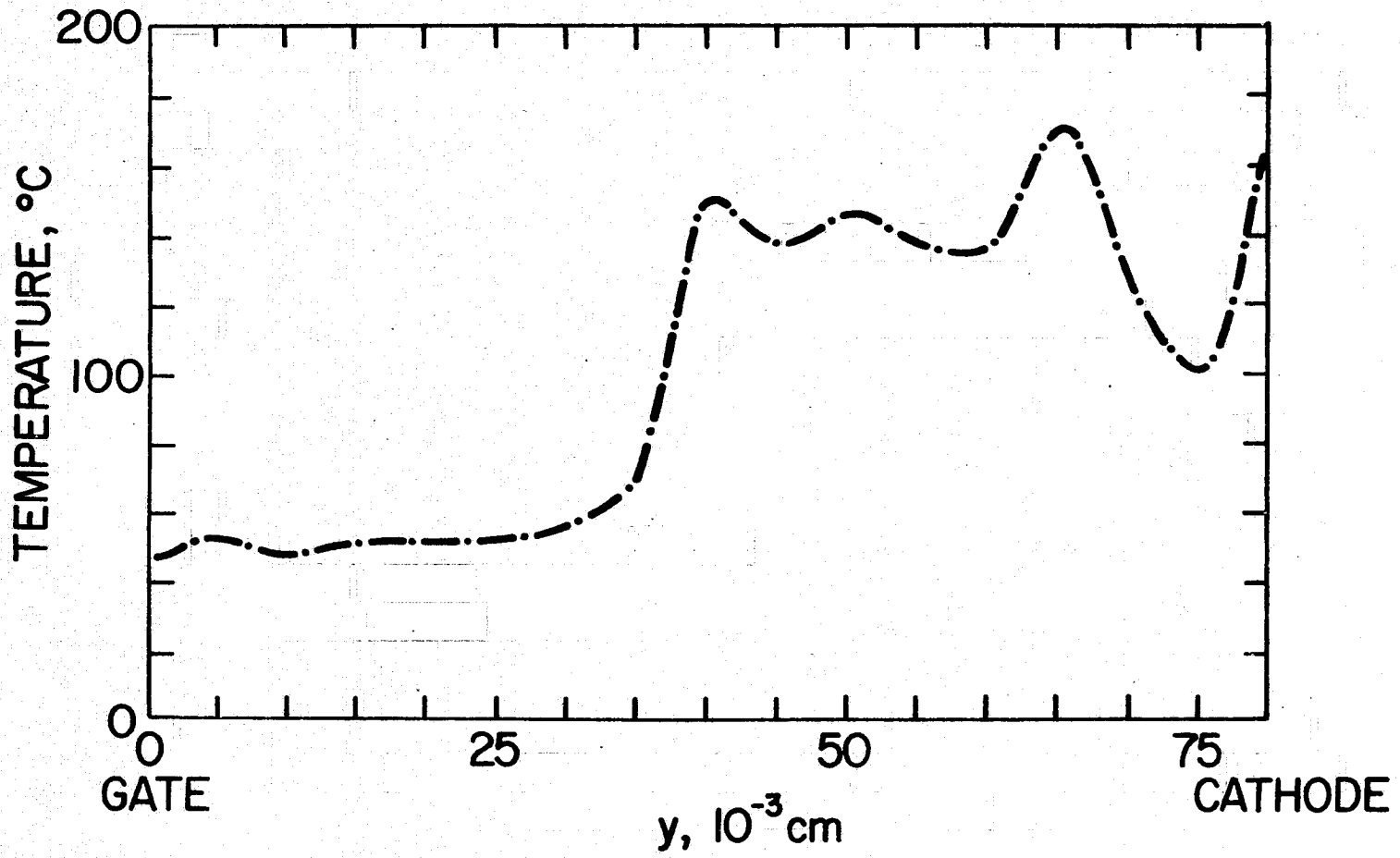


Figure 32. Variation of the temperature value between cathodes. (Static Case).

# CHAPTER V

## RESULTS AND CONCLUSIONS

The static measurements shown in Chapter IV Tables 6 through 10 and Figures 31 and 32 may be compared with the theoretical calculations of Chapter II. From the current density-temperature correspondence given earlier in equation (135) namely,

$$\Delta T = 1.66 \times 10^{-7} \left( \frac{\rho_R}{C_{DP}} \right) J^2 \Delta t$$

one sees that current density J is proportional to $\sqrt{\Delta T}$. The current density of minority carriers in the $p_2$-region as calculated in equation (35) is of the form

$$J_{np}2 = qD_n \frac{\partial N_s}{\partial x} = qD_n \begin{cases} n_o' + (n_w' - n_o') \sin^4 \frac{\pi y}{2\ell} & 0<y<\ell \\ n_w' & \ell<y<L-\ell \\ n_o' + (n_w' - n_o') \sin^4 \frac{\pi (L-y)}{2\ell} & L-\ell<y<L \end{cases}$$

and is plotted in Figure 7.

One could compare these two results by fitting the expressions of "$\sin^4 \frac{\pi y}{2\ell}$ to the plot of $\sqrt{\Delta T}$. This is done in Figure 33, by choosing the value of "$\ell$" in the expression of $\sin^4 \frac{\pi y}{2\ell}$ to be $2 \times 10^{-2}$ cm.

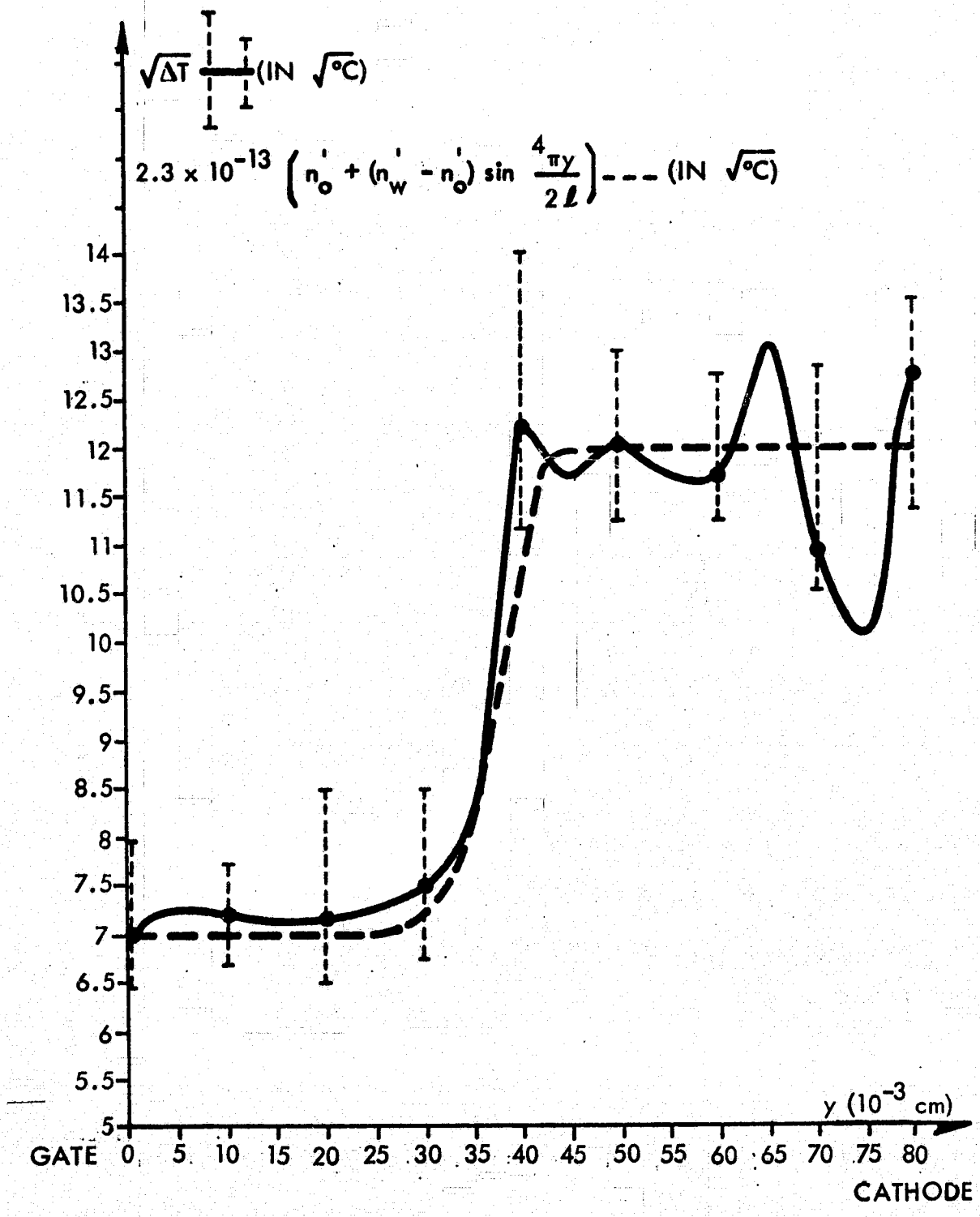


Figure 33 Comparison of the Analytical Calculation $2.3 \times 10^{-13} \left( n_o' + (n_w' - n_o') \sin^4 \frac{\pi y}{2\ell} \right)$ and Experimental Results ($\sqrt{\Delta T}$)

(Static Case)

The experimental result of $\sqrt{\Delta T}$ gives an overall thermal profile of the device, while the analytical calculation show a localized current density distribution J, e.g. equation (35) of Chapter II is giving $\frac{\partial N_s}{\partial x}$ at x=w. The assumption of $\text{Sin}^4 \frac{\pi y}{2\ell}$ in Chapter II fits the experimental results satisfactorily when "$\ell$" is well-chosen. At the same time one can obtain $n_w'$ and $n_o'$ to specify the "central" and "outer" current density. The thermal profile measured and shown in Figure 32 of Chapter IV, or $\sqrt{\Delta T}$ shown in Figure 33, is matching with the boundary condition

$$\left.\frac{\partial N_s}{\partial y}\right|_{y=o} = 0$$

In the range of $y=(50\sim80)\times10^{-3}$ cm the curve does not quite stay level as suggested for the central region of Figure 7. This may be due to the crystal defect and non-uniform doping depth that cause a non-uniform resistivity for the device in the "on" state[52]. Also, when modifying the contacts, the photoresist processing is not smooth enough to give well-defined metal contacts, and this could account for the level variations.

The dynamic measurements shown in Table 1 through 5 and Figures 29 and 30 may be compared with the theoretical calculations. By the linear correspondence between $\sqrt{\Delta T}$ and J in equation (135), the measured $\Delta T$ of Figure 30 should be plotted as $\sqrt{\Delta T}$ in Figure 34, and typical

current density calculation in Figure 15D plotted on this same graph and the two compared. When this is done one can conclude that:

1. The correspondence between analytical and experimental results is quite satisfactory.
2. In the current density plot in Figure 15D, the curve that fits the experimental result best is the curve that represents the dominant current density distribution in the interval of triggering.
3. The mathematical methods developed are useful in obtaining solutions sought in this work.
4. The current density distribution assumed for the static analysis was valid.
5. The infrared thermal mapping technique developed and used in this work produced thermal profiles, which verify the static and dynamic analysis.

This technique could also be very well used to identify "hot spots" of thyristors or other multijunction devices. The analytical results verified serve as descriptive functions for minority carrier distribution at all points at each instant of time. The method used to calculate these functions numerically is a valid method of describing the switching and will help understand the operation of these devices. The analysis presented in this report can be further extended to some special case, like high level injection. It can also serve the device designers whenever numerical calculations are done with various device parameters and

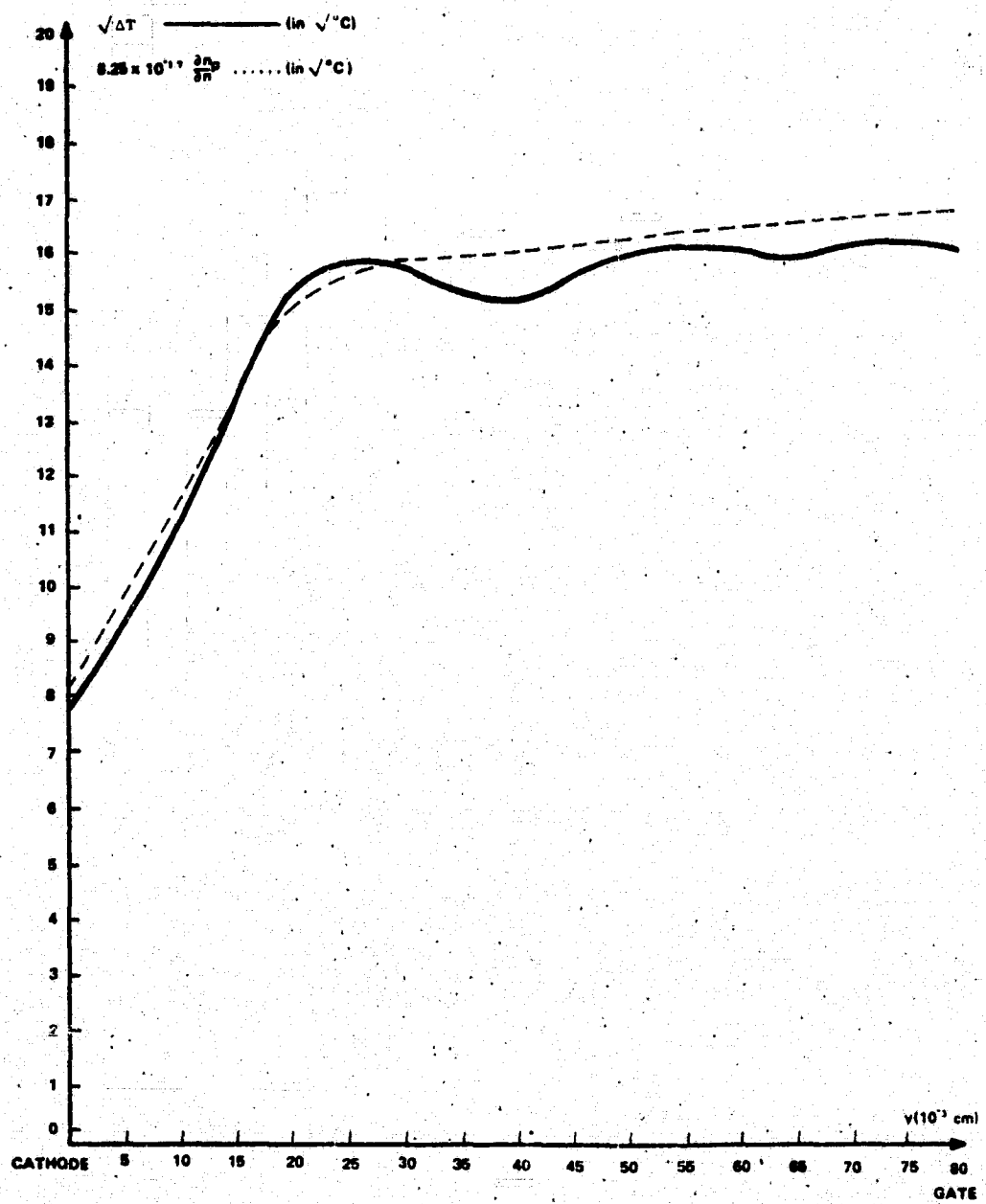


Figure 34 Comparison between Experimental Results ( $\overline{\Delta T}$) and Analytical Results ($8.25 \times 10^{-17} \frac{\partial n_p}{\partial x}$ at $x=5 \times 10^{-4}$ cm, $t=10^{-6}$ sec) (Dynamic Case)

operation conditions. The mathematical techniques used in the analysis is not limited to thyristors, but are also applicable to other three-terminal devices like bipolar transistors.

The results derived from this work have made a significant contribution to the methods of analysis of thyristor (and other multijunction type devices) and have given good verification of these methods by experimental means. An equally significant result of this work is the development of the experimental method of testing these devices for design optimization hot spots, fabrication defects and improper device operating setup by examining the temperature map within the device. The experimental setup can be further modified so as to build a compact system to map thermal profiles of semiconductor devices. These new extensions of this work are well worth pursuing.

## APPENDIX A

## STATIC CALCULATIONS OF $A_k$ AND $B_k$ WHEN $I_g = 0$

By condition (A) and equation (34), we have

$$n_{po} = \sum_{k=o}^{\infty} \cos \frac{k\pi y}{L} \; B_k \sinh \sqrt{\alpha}\, w$$

where $\alpha$ means

$$\sqrt{\frac{1}{L_n^2} + \frac{k^2\pi^2}{L^2}}$$

Integrating both sides with respect to y from 0 to L, we obtain

$$B_k = \begin{cases} \dfrac{n_{po}}{\sinh \dfrac{w}{L_n}} & \text{for } k = 0 \\ 0 & \text{for } k \neq 0 \end{cases} \qquad \text{(A-1)}$$

Taking the drivative of equation (34) one obtains:

$$\left.\frac{\partial N_s}{\partial x}\right|_{x=w} = \sum_{k=o}^{\infty} \cos \frac{k\pi y}{L} \; \sqrt{\alpha} \; [A_k \cosh \sqrt{\alpha}\, w + B_k] \qquad \text{(A-2)}$$

Equating this to equation (35), one can find the values of $A_k$. For k = 0

$$\frac{1}{L_n} \int_o^L (A_o \cosh \frac{w}{L_n} + B_o)\, dy = \int_o^L Q\, dy$$

$$A_o = \left\{ \left[ n_w'\left(L - \frac{5}{4}\ell\right) + \frac{5}{4} n_o'\ell \frac{L}{L_n} - B_o \right\} \right/ \cosh \frac{w}{L_n} \qquad \text{(A-3)}$$

For $k \neq 0$,

$$A_k \cosh \sqrt{\alpha}\, w \int_o^L \cos \frac{k'\pi y}{L} \left( \sum_{k \neq o} \cos \frac{k\pi y}{L} \right) dy$$

$$= n_w' \int_\ell^{L-\ell} \cos \frac{k'\pi y}{L}\, dy + \int_o^\ell + \int_{L-\ell}^L n_o' \cos \frac{k'\pi y}{L}\, dy$$

$$+ \int_o^L (n_w' - n_o') \sin \frac{4\pi y}{2\ell} \cos \frac{k'\pi y}{L}\, dy$$

$$+ \int_{L-\ell}^L (n_w' - n_o') \sin \frac{4\pi(L - y)}{2\ell} \cos \frac{k'\pi y}{L}\, dy \qquad \text{(A-4)}$$

and

$$A_k = \frac{4(n_w' - n_o') \sin \frac{k\pi\ell}{L}}{n\pi \sqrt{\alpha} \cosh \sqrt{\alpha}\, w} \left\{ -1 + \frac{k\ell}{L(2 + \frac{n\ell}{L})} \left[ 1 + \frac{2}{1 + \frac{k\ell}{L}} \left(1 + \right.\right.\right.$$

$$\left.\left.\left. \frac{3}{2\frac{k\ell}{L}} \left[ 1 + \frac{1}{2\frac{k\ell}{L} - 4} + \frac{1}{2\frac{k\ell}{L} - 2} \right] \right) \right] \right]$$

k's are even and non-zero integers.

## APPENDIX B

## STATIC CALCULATION OF $A_K$, $B_K$ AND $C_K$ WHEN $I_g \neq 0$

When $I_G \neq 0$, the gate is closed, no charge can accumulate on the metal contact which will block electrons from sweeping out, thus condition B, is now valid and

$$N_s(\overline{W},y) = \sum_{k=o}^{\infty} \cos \frac{k\pi y}{L} \left[A_k \sinh (\sqrt{\alpha}\, \overline{W}) + B_k \sinh (\sqrt{\alpha}\, (\overline{W} - w)) - C_k \sinh \sqrt{\alpha}\, (\overline{W} - w))\right] = 0 \qquad \text{(B-1)}$$

In order to obtain $A_k$, and $C_k$ independent of y, we may set the contents of the square bracket to zero, namely,

$$C_k = B_k + A_k \frac{\sinh\sqrt{\alpha}\, \overline{W}}{\sinh[\sqrt{\alpha}(\overline{W} - w)]} . \qquad \text{(B-2)}$$

By condition (E) and (B-2),

$$\frac{I_{nG}}{qD_n} = 2 \frac{H\ell_1 A_o \sinh(W/L_n)}{l_n \sinh[(\overline{W} - w)/L_n]}$$

$$+ 2H \sum_{\substack{k \neq 0 \\ k,\text{even}}}^{\infty} \frac{\sqrt{\alpha}L \sin(k\pi\ell_1/L) A_k \sinh(\sqrt{\alpha}w)}{k\pi \sinh[\sqrt{\alpha}\, (W - w)]} \qquad \text{(B-3)}$$

By condition (F) and (B-1),

$$I_{np}(J_3) = HqD_n \left[ \frac{L - 2\ell_1}{L_n} \left( A_o \cosh \frac{W}{L_n} + B_o \right) \right.$$

$$+ 2 \sum_{\substack{k \neq o \\ k,\text{even}}}^{\infty} A_k \sin \frac{k\pi\ell_1}{L} \left( - \frac{L\sqrt{\alpha}}{k\pi} \cosh(\sqrt{\alpha}\, w) \right.$$

$$\left. \left. + \frac{k\pi \sinh(\sqrt{\alpha}\, w)}{L\sqrt{\alpha} \sinh[\sqrt{\alpha}\, (\overline{W} - w]} \{1 - \cosh[\sqrt{\alpha}\, (\overline{W} - w)]\} \right) \right] \qquad \text{(B-4)}$$

## APPENDIX C

## PROCESS TO MODIFY METAL CONTACTS OF METALIZED THYRISTOR

The process to modify the metal contacts is as follows:

(1) Strip metal contacts: Put a wafer of finished but uncut thyristors into ferric nitrate for 5 minutes, the top silver will be etched away, then the nickelchrome can be etched away by concentrated hydrochloric acid. Rinse with de-ionized water, dry by dipping isopropyl alcohol, put into vacuum oven of 90°C overnight.

(2) Evaporate aluminum on both sides of the wafer.

(3) Put on photoresist: Apply photoresist on both sides by Waycoat 60 cps, then spin dry by 3000 RPM for 15 seconds, soft bake at 65°C for 20 minutes. This makes photoresist of 1.4 μm.

(4) Mask making: By photographic reduction, make a mask of the geometry as shown in Figure 24-B. Note, that only solid-lined regions are for the gate-cathode mask. Some geometry is for the anode mask, but two stripes of 0.01 cm wide should be made on the edge to join these two solid-lined areas.

(5) Expose to ultra-violet light for 10 seconds with anode mask and gate-cathode mask on each side of the wafers, develop in Kodak Thin Film Resist Developer for 30 seconds and rinse in Kodak Thin Film Resist Rinse for 20 seconds.

(6) Put into aluminum etch (one part of concentrated HCl and four part of deionized water) for five minutes.

(7) Strip photoresist: Put into J-100 (at 100$^{o}$C) for 10 minutes then xylene, TCE (at 70$^{o}$C), acetone for 2 minutes each, dry by dipping in isopropyl alcohol for 30 seconds, and air dry. The process is now finished.

## APPENDIX D

## COMPUTER PROGRAMS

Computer programs for calculating $n_p(x,y,t)$, $I_{J2}(n_p)$, $I_{J3}$, $P_n(x,t)$ and $I_J$, are available on request from the authors.

## APPENDIX E

## LIST OF SYMBOLS

| | |
|---|---|
| $A_k$ | |
| $B_k$ | |
| $C_k$ | |
| c | speed of light |
| $D_n$ | diffusion constant of electrons |
| D* | detectivity of photo-cell |
| $\vec{E}$ | electric field |
| $E_g$ | energy band gap of silicon |
| $\epsilon$ | dielectric constant |
| G | generation rate |
| H | length of gate or cathode contacts |
| $I_A$ | anode current |
| $I_{co}$ | transistor reverse saturation current of the collector junction with emitter open-circuited |
| $I_K$ | cathode current |
| $I_G$ | gate current |
| $I_{Gn}$ | gate current of electrons |
| $I_{np}(J_3)$ | minority carrier current in $p_2$ of junction $J_3$ |
| J | current density |
| $J_{Gn}$ | gate current density of electrons |
| K | Boltzmann constant |
| $K_{th}$ | thermal conductivity |
| L | device width |

| | |
|---|---|
| $\mathcal{L}$ | Laplace transform of |
| $\mathcal{L}^{-1}$ | inverse Laplace transform of |
| $L_n$ | diffusion length of electrons/holes |
| $L_p$ | diffusion length of holes |
| $m_n$ | effective mass of electrons |
| $m_p$ | effective mass of holes |
| $\underline{n}$ | real part of refraction index |
| $N_A$ | acceptor concentrations in $p_2$-region |
| $N_c$ | effective density of states of conduction band |
| $N_v$ | effective density of states of valence band |
| $n_p$ | electron concentration in p region |
| $n_{po}$ | equilibrium electron concentration in p region |
| $n_{pf}$ | $\equiv n_p$ (at junction $J_2$, when $J_2$ is forward biased) |
| $n_{pw}$ | $\equiv n_{po} \exp(qV_{J3}/kT)$ |
| $n_s$ | steady state concentration of $n_p$ |
| $N_s$ | $\equiv n_s - n_{po}$ |
| $P_n$ | hole concentration in n region |
| P | Laplace transform of $p_n$ |
| $P_p$ | Particular solution of P |
| $P_c$ | complementary solution of P |
| q | electron charge |
| Q | $\equiv \left.\frac{\partial N_s}{\partial x}\right\|_{x=w}$ |
| s | the variable in Laplace domain corresponds to time t |

| | |
|---|---|
| $s_1$ | $\equiv (s + \frac{1}{\tau_p})/Dp$ |
| $t$ | time |
| $T$ | absolute temperature in $^oK$ |
| $U$ | recombination rate |
| $\vec{V}_{Ji}$ | voltage drop in junction $J_i$, i = 1, 2, 3 |
| $\alpha$ | optical absorption coefficient |
| $\alpha_1$ | current gain for the pnp transistor |
| $\alpha_2$ | current gain for the npn transistor |
| $\lambda$ | wavelength of light |
| $\mu_n$ | mobility of electrons |
| $\mu_p$ | mobility of holes |
| $\tau_n$ | lifetime of electrons |
| $\tau_p$ | lifetime of holes |
| $\Theta$ | Theta function |
| $\rho$ | charge density |
| $\rho_p$ | resistivity in p region |
| $\rho_R$ | resistivity |
| $\vec{\nabla}$ | $= \frac{\partial}{\partial x}\ \hat{x} + \frac{\partial}{\partial y}\ \hat{y}$ |

## REFERENCES


1. W. Shockley, "Electrons & Holes in Semiconductors", D. Van Nostrand Company, Inc., (1950).

2. J.L. Moll, M. Tanenbaum, J.M. Goldey, and N. Holonyake, "P-N-P-N Transistor Switches", Proc. IRE, 44 1174 (1956).

3. F.E. Gentry, F.W. Gutzwiller, N. Holonyake, E.E. Von Zastrow, "Semiconductor Controlled Rectifiers", Prentice-Hall, Inc., (1964).

4. J. Millman, H. Taub, "Pulse, Digital, and Switching Waveforms", Chapters 12, 13, McGraw-Hill Book Co., (1965).

5. J.J. Ebers, "Four-Terminal p-n-p-n Transistors", Proc. IRE 40, 1361 (1952).

6. J.F. Gibbons, "A Critique of the Theory of p-n-p-n Devices", IEEE Trans. ED-11, 406 (1964).

7. J.F. Gibbons, "Graphical Analysis of the I-V Characteristics of Generalized p-n-p-n Devices", Proc. IEEE, 55, #8, 1366 (1967).

8. E.S. Yang, I.G. Shalnik, "Generalized Turn-On Criterion of p-n-p-n Devices", IEEE, Trans. ED-14, #8, 450 (1967).

9. N. Mapham, "Overcoming Turn-On Effects in SCR", Electronics, p. 50, August 17 (1962).

10. B.M. Rabinovici, "Proposal for Study of the Switching Characteristics of Semiconductor Power Devices", submitted to NASA, Sept. 1968.

11. W.H. Dodson, R.L. Longini, "Probed Determination of Turn-On Spread of Large Area Thyristor", IEEE Trans. ED-13, #5, 478, (1966).

12. G.D. Bergman, "The Gate-Triggered Turn-On Process in Thyristors", Solid-State Elec. 8, 757, (1965).

13. IEEE Trans. on Elect. Dev. ED-17, #9, A special issue on "High-Power Semiconductor Devices", (1970).

14. Proc. of the IEEE, 55, #8, (1967). A special issue on "High-Power Semiconductor Devices".

15. B.M. Rabinovici, Progress Report, NASA Contract NAS12-2053, July 1970.

16. W.H. Dodson, R.L. Longini, "Probed Determination of Turn-On Spread of Large Area Thyristors", IEEE Trans. ED-13, #5, 478 (1969).

17. H.J. Ruhl Jr., "Spreading Velocity of the Active Area Boundary in a Thyristor", IEEE Trans. ED-17, #9, 672 (1970).

18. B.R. Page, L.R. Reid, "An Infrared Microradiometer", IEEE Trans. IM-15, #3, 89 (1966).

19. Yu. I. Ukhanov, "Optical Absorption of Ge and Si at Temperatures 77°K to 1000°K", Soviet Physics - Solid State, 3, #7, 1529 (1962).

20. Special Issue on High-power Semiconductor Devices, Proc. IEEE, August 1970.

21. Special Issue on High-power Semiconductor Devices, Trans., IEEE, September 1970.

22. J.L. Blue, "Two-dimensional Distributed Base-resistance Effects in Bipolar Transistor", Bell Telephone Lab., Murry Hill, N.J. Private Communication, September 1971.

23. E.S. Yang, "Two-dimensional Current Flow in Semiconductor Devices", Int. J. Electronics, 23, No. 3, 221, (1967).

24. D. Vandorpe, N.S. Xuong, "Mathematical Two-dimensional Model of Semiconductor Device", Electronics Letter, 7, No. 2, 47, (1971).

25. S.M. Sze, "Physics of Semiconductor Devices", Wiley-Interscience 1969. Chapter II. Sect. 7.

26. C.D. Hachtel, R.C. Joy, and J.W. Conley, "A New-Dimensional Analysis Program for Junction Device Modeling", Proc. of IEEE, 60, No. 1, January 1972, p. 87, equation 5.

27. Reference 25. Table 2.4.

28. Section 2.5 of Reference 3, a and c are related to the current gains of $p_1$-$n_1$-$p_2$ or $n_1$-$p_2$-$n_2$ transistors, b depends on the current level, the density of the trapping sites and their energy levels which is between 1 and 2.

29. H.S. Carslaw, J.C. Jaeger, "Conduction of Heat in Solids", Oxford Press, 1959.

30. E.S. Yang, N.C. Voulgaris, "On the Variation of Small-signal Alphas of p-n-p-n Device with Current", Solid-State Electronics, 10, 641, (1967).

31. J.F. Gibbons, "Graphical Analysis of the I-V Characteristics of Generalized p-n-p-n Devices", Proc. IEEE, 55, 1366, (1967).

32. R.L. Davies, J. Petruzella, "p-n-p-n Charge Dynamics", Proc. IEEE, 55, 1318, (1967).

33. A.A. Lebedev, A.I. Uvarov, V.E. Chelnokov, "The Transient Characteristic of the p-n-p-n Structure", Rad. Eng. El. Phys. 11, #8, 1264, (1966).

34. A.A. Lebedev, A.I. Uvarov, V.E. Chelnokov, "Establishment of the Stationary State for Turning on a p-n-p-n Structure", Rad. Eng. El. Phys. 12, #10, 626, (1967).

35. A.A. Lebedev, A.I. Uvarov, V.E. Chelnokov, "The Effect of An Electric Field on the Switching Process in p-n-p-n Structure", Rad. Eng. Elect. Phys. 12, 1358, (1967).

36. A.A. Lebedev, A.I. Uvarov, "Switching a Symmetical p-n-p-n Structure when the Dependence of the Amplification Factors on Current is taken into Account", Rad. Eng. Elect. Phys. 12, 830, (1967).

37. R.L. Longini, J. Melngailis, "Gated Turn-on of Four Layer Switch", IEEE ED-10, 178, (1963).

38. Harry Bateman, "Tables of Integral Transform", Vol. I, McGraw-Hill Book Co., 1954.

39. M. Abramowitz and I.A. Stegun, "Handbook of Mathematical Functions", National Bureau of Standards, 1964.

40. A.Y.C. Yu, "The Metal-Semiconductor Contact", IEEE Spectrum, p. 83, March, 1970.

41. N. Mapham, "Overcoming Turn-on Effects in Silicon Controlled Rectifiers, "Electronics, August 17, (1962), p. 50.

42. B.R. Pagel and L.R. Reid, "An Infrared Microradiometer", IEEE Trans., IM-15, 89, (1966).

43. S.M. Sze, "Physics of Semiconductor Devices", Wiley-Interscience 1969. Chapter 2, Section 6.

44. G.G. MacFarlane, T.P. McLean, J.E. Quarrington and V. Roberts, "Fine Structure in the Absorption Edge Spectrum of Si", Physics Review 111, 1245, (1958).

45. Reference 25, Chapter 2, Figure 27.

46. W.R. Runyan, "Silicon Semiconductor Technology", McGraw-Hill, (1965).

47. A.R. Hilton and C.E. Jones, J. El. Chem. Soc. 113, 472, (1966).

48. H.F. Wolf, "Silicon Semiconductor Handbook", Pergamon Press, (1968).

49. American Institute of Physics Handbook, (1968).

50. Reference 25. Chapter 2, equation (75).

51. P.D. Maycock, Solid State Electronics, 10, 161, (1967).

52. Julian Been, "I-V Characteristics of Forward Conducting Thyristor", NASA Lewis Research Center, Cleveland, Ohio, Private Communication, April 1972.